

**A NOVEL MULTIPLE-PHASE,
MULTIPLE-COMPONENT, THERMAL LATTICE
BOLTZMANN MODEL**

by

Michael Ikeda

B.S. in Mechanical Engineering, California Institute of Technology,

2007

M.S. in Mechanical Engineering, University of Pittsburgh, 2010

Submitted to the Graduate Faculty of
the Swanson School of Engineering in partial fulfillment
of the requirements for the degree of
Ph.D. in Mechanical Engineering

University of Pittsburgh

2012

UNIVERSITY OF PITTSBURGH
SWANSON SCHOOL OF ENGINEERING

This dissertation was presented

by

Michael Ikeda

It was defended on

November 8th, 2012

and approved by

Laura A. Schaefer, Ph.D., Professor, Department of Mechanical Engineering and Materials
Science, University of Pittsburgh

Sung Kwon Cho, Ph.D., Professor, Department of Mechanical Engineering and Materials
Science, University of Pittsburgh

Minking K. Chyu, Ph.D., Professor and Department Chair, Department of Mechanical
Engineering and Materials Science, University of Pittsburgh

Shi-Chune Yao, Ph.D., Professor, Department of Mechanical Engineering, Carnegie Mellon
University

Dissertation Director: Laura A. Schaefer, Ph.D., Professor, Department of Mechanical
Engineering and Materials Science, University of Pittsburgh

Copyright © by Michael Ikeda
2012

A NOVEL MULTIPLE-PHASE, MULTIPLE-COMPONENT, THERMAL LATTICE BOLTZMANN MODEL

Michael Ikeda, PhD

University of Pittsburgh, 2012

The lattice Boltzmann method (LBM) is gaining traction as a powerful approach to fluid flow simulation. In this work, developments toward the incorporation of more complex physical phenomena into the LBM are presented. As will be discussed, existing approaches are currently inadequate for thermal flows with wall interactions and multiple components. A novel methodology will be detailed, which enables the simulation of multiphase, multicomponent, thermal flows. The need for these simulation techniques is clear. As energy densities in electronic devices rapidly increase, improved two-phase microchannel heat exchanger designs are of great interest. Similarly, with the implementation of phase separation as a method of flow manipulation in microdevices, understanding the flow dynamics of multiple phases in microchannels is vital. However, experimental studies have thus far shown a great deal of variety in the flow patterns and instabilities that develop at the microscale level. Thus, numerical techniques capable of simulating such conditions are desirable. While traditional computational fluid dynamics (CFD) methods are based on macroscale equations, and molecular dynamics simulations seek to model the microscopic behavior of individual molecules, the LBM takes a mesoscopic approach. Based on the linearized kinetic lattice Boltzmann equation, particle interactions are directly implemented, while the movement of those particles is confined to a discrete lattice. This makes the LBM very useful in modeling interfacial dynamics and multiphase flows, while avoiding the enormous computational complexity of a direct MD simulation.

The novel contributions of this work are: a) the combination of the Peng-Robinson equation of state with a recently developed linear approximation of the interparticle interaction gradient for the improvement of the multiphase, single-component, thermal (MPSC-T) LBM, b) the development of a thermally-dependent wall interaction model for dynamic contact angle simulation in the MPSC-T LBM, c) an analysis of the stability region of the interparticle interaction parameters in a multiphase, immiscible, multicomponent, isothermal (MPiMC-IT) model, and d) the development of a multiphase, immiscible, multicomponent, thermal (MPiMC-T) model using a density-weighted coupling of macroscopic properties.

TABLE OF CONTENTS

1.0 INTRODUCTION	1
1.1 Motivation	1
1.2 Computational Fluid Dynamics	2
1.2.1 Traditional CFD	2
1.2.2 Kinetic Theory	3
1.2.2.1 Microscopic Molecular Dynamics	4
1.2.2.2 The Mesoscopic Lattice Boltzmann Model	4
1.3 Voids in the LBM Field	5
1.4 Organization	6
2.0 THE LATTICE BOLTZMANN METHOD	9
2.1 Linearization of the Boltzmann Transport Equation	9
2.2 Discretization of the Boltzmann-BGK Equation	11
2.2.1 Projection onto a Hermite Basis and Truncation of the Polynomials	11
2.2.2 Discretization of the Velocity Space via Quadrature	13
2.3 Hydrodynamic Boundary Conditions	17
2.3.1 Solid Boundaries	17
2.3.1.1 Dry-node BCs	18
2.3.1.2 Wet-node BCs	18
2.3.2 Open Boundary Conditions	19
2.4 Forces: The Exact Difference Method	20
2.5 Single-phase, Single-component, Isothermal Model (SPSC-IT) Results	21
2.6 Physical Translation	24

3.0 MULTIPHASE LBM	27
3.1 Interparticle Potentials	27
3.2 Gradient Operator Discretization	29
3.3 Multiphase, Single-component, Isothermal Model (MPSC-IT) Results	35
4.0 THERMAL MODEL	38
4.1 Thermal Forces	39
4.2 Thermal Boundary Conditions	40
4.3 Single-phase, Single-component, Thermal Model (SPSC-T) Results: Rayleigh-Bénard Convection	41
4.4 Multiphase, Single-component, Thermal Model (MPSC-T) Results: Spinodal Decomposition	41
4.5 A Novel Wall Interaction Model	47
4.5.1 Wall Interaction Parameter Determination	50
4.5.2 Wall Interaction Model Results	56
4.6 Multiphase, Single-component, Thermal Model (MPSC-T) Results: Bubble Simulations	60
5.0 MULTICOMPONENT MODEL	66
5.1 Intercomponent Interactions	66
5.2 Multiphase, Immiscible, Multicomponent, Isothermal Model (MPiMC-IT) Results: Static Droplet	68
5.3 Incorporation of a Thermal Model	72
5.3.1 Stability Analysis of Interaction Parameters	72
5.3.2 Reconstruction of Macroscopic Variables	73
5.4 Multiphase, Immiscible, Multicomponent Thermal Model (MPiMC-T) Results	81
5.4.1 Static Thermal Conduction	81
5.4.2 Static Droplet	86
5.4.3 Thermocapillary Migration	91
6.0 CONCLUSIONS AND FUTURE WORK	99
6.1 Primary Contributions	99

6.1.1 Multiphase, single component, isothermal model gradient operator approximation	99
6.1.2 Multiphase, single component, thermal wall interaction model	99
6.1.3 Multiphase, immiscible, multicomponent, isothermal model stability analysis	100
6.1.4 Multiphase, immiscible, multicomponent, thermal model	100
6.2 Future Work	101
6.2.1 Incorporation of the Wall Interaction Model in MPiMC-T model	101
6.2.2 Gradient Approximations	102
6.2.3 Homogeneous Nucleation	102
6.2.4 Higher-Order Thermal Lattice Boltzmann Model	102
6.2.5 Comparison to Alternative Multiphase Methods	103
BIBLIOGRAPHY	105

LIST OF TABLES

1	Coefficients for the quadratic fits of contact angles vs. wall interaction parameters at various temperatures.	54
2	Coefficients for the cubic fits of contact angles vs. wall interaction parameters at various temperatures.	54
3	The exponential function parameters determined for the quadratic coefficients.	55
4	The exponential function parameters determined for the cubic coefficients. . .	55
5	Experimental coefficient sets.	56
6	Root mean square errors (RMSE) between the LBM simulation results and the experimental functions for each fit type.	59

LIST OF FIGURES

1	The common lattice structures utilizing (a) nine velocities in two dimensions and (b) nineteen velocities in three dimensions (including the zeroth velocities).	14
2	Inlet boundary layout.	20
3	Domain configuration for gravity-driven Poiseuille flow through a 2D slit.	22
4	Velocity profiles of gravity and pressure-driven Poiseuille flows through 2D slits.	23
5	Domain configuration for shear-driven Couette flow in a 2D slit.	24
6	Velocity profiles of shear-driven Couette flow.	25
7	Comparison of different effective mass models used for calculating the interparticle interaction potentials.	29
8	Grid-independence test of the multiphase model in a periodic domain showing the density ratio, normalized by the maximum density ratio, as grid resolution is increased.	32
9	Comparison of different methods of approximating the gradient operator in the interparticle interaction force equation.	33
10	Comparison of different values of A used in the linear combination gradient approximation of the gradient operator in the interparticle interaction force equation.	34
11	Pv diagram of the binodal curve and an isotherm used for multiphase simulation initialization.	36
12	An isothermal, static droplet (red) at equilibrium with surrounding vapor (blue).	36
13	An isothermal, static vapor bubble (blue) at equilibrium with surrounding liquid (red).	37

14	Temperature contours and velocity vectors, given in lattice units, of pure conduction and Rayleigh-Bénard convection between a heated lower wall and a cooled upper wall with periodic BCs at the sides ($Pr = 1$).	42
15	The spinodal decomposition process showing phase separation due to an unstable density initialization evolved isothermally.	44
16	The spinodal decomposition process showing phase separation due to an unstable density initialization evolved using the passive-scalar thermal model. .	45
17	Evolution of the total mass, the liquid mass, and the vapor mass in the domain through time during the spinodal decomposition process (normalized by the total initial mass) for the isothermal and thermal models.	46
18	Density contours showing the progression of a typical simulation of a droplet (red) wetting the bottom wall of a periodic 2D channel filled with vapor (blue) at various timesteps.	48
19	Grid independence of the contact angle measurement to within the measurement error ($< 1^\circ$).	49
20	Contact angles vs. wall interaction parameters	51
21	Polynomial fits of contact angles vs. wall interaction parameters	53
22	LBM simulation results using wall interaction parameter curve fits based on the specified contact angle coefficient set.	57
23	The initial density contours of a vapor bubble (blue) surrounded by liquid (red). .	62
24	Density contours of bubble (blue) dissolution into the surrounding liquid (red) shown at various timesteps of the simulation.	62
25	Density contours of the boiling process, showing the expansion of a vapor bubble (blue) due to an initial liquid (red) superheat at various timesteps of the simulation.	63
26	The time evolution of the vapor mass fraction during boiling, depicting the phase change process.	64
27	Density contours of various contact angle functional forms at 100,000 timesteps during a flow boiling simulation showing the effect on flow boiling dynamics of the wall wetting interaction model.	65

28	The two numerical grids for each chemical component showing the reduced density contours of a typical 2D, two phase, two component droplet simulation.	69
29	Reduced density cross-sections of a liquid water droplet in air at 450 K. The density ratio is 152:1.	70
30	Reduced density cross-sections of a liquid water droplet in air at 600 K. The density ratio is 13:1.	71
31	Reduced density cross-sections showing a ratio error where the zero-density region of the water is larger than the vapor phase region of the air.	74
32	Stability region analysis of intercomponent interaction parameters at the specified temperatures.	75
33	Overlap of the stable regions of the intercomponent interaction parameters from 450 K to 625 K.	78
34	Initial reduced density contours showing the two liquid layers (red) and zero-density regions (blue) on the two grids of the 2D, two component, thermal conduction simulation.	82
35	Initial reduced temperature cross-section (taken at $x = 50$ LU) and reduced temperature contours of the 2D, two component, thermal conduction simulation.	83
36	Reduced temperature cross-sections of grid one (taken at $x = 25$ LU) showing the time evolution of the thermal profile of the 2D, two component, thermal conduction simulation. Each line represents a single timestep, with darker colors corresponding to increasing times.	84
37	Final reduced density cross-sections and reduced temperature contours of grid one of the 2D, two component, thermal conduction simulation.	85
38	Residual temperature error between the simulation results and the theoretical solution as the 2D, two component thermal conduction simulation evolves through time.	85
39	Temperature and velocity errors that result from using different coupling models in the MPiMC-T model as the thermal conduction simulation evolves through time.	87

40	Comparison of the evolution of the total temperature in the domain using different coupling models in the MPiMC-T LB model for a static droplet simulation.	89
41	Temperature and velocity errors that result from relaxing the coupling requirements in the MPiMC-T model as the static droplet simulation evolves through time. Note that the results from TC, VC, and TCVC all overlap for the temperature errors, but only the results from VC and TCVC overlap for the velocity errors.	90
42	Comparison of the spurious currents in the steady-state static droplet simulation using the model with no coupling and the model with both temperature and velocity-coupling.	92
43	Progression of a liquid droplet surrounded by air due to thermocapillary migration shown at various timesteps during the simulation.	94
44	Droplet location during thermocapillary migration studies at various temperatures.	96
45	Thermocapillary droplet migration velocities, normalized by the 25 K thermal gradient case.	97
46	Droplet location during thermocapillary migration studies at various temperatures. Filled datapoints represent those used for the determination of the droplet velocity in the quasi-steady flow regime.	98

1.0 INTRODUCTION

1.1 MOTIVATION

Thermal fluid flows, especially those with multiple phases and multiple components, are ubiquitous. However, the dynamics of these systems are not well understood. The study of thermal fluid flows is therefore of great interest from the perspective of both fundamental scientific research and engineering applications. Furthermore, the interaction between liquids and solids is significant to innumerable natural and engineering processes, and yet the physics governing liquid-solid dynamics are not clear. The presence of phase transitions further complicates the resulting dynamics of this problem. An excellent review on the many gaps in the fundamental knowledge of the phase transition process at contact lines and the breadth of applications that could benefit from an improved understanding of these physics was recently presented by Sefiane, et al. [1]. The flow boiling process that occurs in microchannels has itself been the subject of intense experimental inquiry in the past decade [2–12]. What is clear from all of these studies is that significantly more investigation is needed to shed light on these phenomena.

In this work, a method is developed to investigate aspects of the underlying physics behind multiphase, multicomponent, thermal flows through direct numerical simulation (DNS). This will aid in the development of more efficient and effective engineering devices. The applications that could benefit from this work range from large-scale, boiling water reactor design, to small-scale, lab-on-a-chip flow control. For instance, consider microelectronic cooling systems. Following Moore’s law, the number of transistors on a microchip has doubled every two years. Unfortunately, as transistors decrease in size, it becomes more and more difficult to remove their high energy fluxes through their shrinking footprints. Consequently,

Moore's law has been bottlenecked by thermal issues [13, 14]. It has long been known that microchanneled, two-phase cooling systems can play a significant role in solving the high energy density problem of microelectronics [14, 15]. However, research has proven that there is a large variation in the flow patterns and instabilities depending on the specific conditions of the study. Accurate numerical techniques could prove of great use in determining the cause of many of the peculiarities that arise during flow boiling in microchannels, leading to the development of improved cooling systems.

1.2 COMPUTATIONAL FLUID DYNAMICS

The field of computational fluid dynamics (CFD) concerns the numerical study of transport phenomena through the solution of partial differential equations (PDEs) in discrete space and time. The equations to be solved, and the manner in which they are discretized, can vary greatly depending on the problem of interest. Over the last 50 years, the solution of the Navier-Stokes (NS) equations using finite volume and finite difference approaches has dominated the fluid flow modeling community. However, in the past two decades, alternative approaches have arisen and are beginning to take hold due to their ability to capture more complex flow dynamics.

1.2.1 Traditional CFD

The NS equations are a macroscopic viewpoint of fluid flow as they are derived from the application of Newton's Second Law to a control volume and express conservation of momentum [16]. When combined with conservation of mass and energy, these equations describe the bulk transport of the macroscopic properties of a fluid: density, velocity, and temperature. Discretizing the equations in space and time and solving them numerically yields the flow properties at each node of the grid. As CFD techniques have evolved and their utility in both research and industry have been proven, there has been considerable interest in modeling more diverse and more complex flow fields. Highly accurate and efficient schemes are now

capable of solving a multitude of problems, but some regimes, such as turbulent flows and multiphase flows, are still the subject of intense research. Flows which occur when multiple phases are present provide a particularly interesting complication as the phase separation process is a consequence of long-range molecular interactions. Given that no consideration is given in the macroscopic NS equations to molecular behavior, the simulation of multiple phases is very difficult with these models.

Multiphase NS solvers currently account for the phase separation artificially by tracking the location of the interface between phases. In Lagrangian mesh routines, the mesh boundary, which defines the interface, must be constantly regenerated while the interface moves. In Cartesian meshing schemes, two of the most common approaches are the volume of fluid (VOF) method and the level-set method (LSM). These schemes involve front-tracking the interface, in which either the volume fraction of vapor or the distance to the interface, respectively, is advected through the domain [17, 18]. However, continuously updating a mesh or solving an advection equation is difficult and extremely computationally expensive. With this complexity compounding the already immense task of direct numerical simulation using the NS equations, these solvers become prohibitively expensive for realistic applications. Thus, different models are needed for multiphase simulations.

1.2.2 Kinetic Theory

While traditional fluid dynamics and thermodynamics give descriptions of the macroscopic transport in a system, they do nothing to describe the molecular behaviors that cause the macroscopic effects that can be observed. Kinetic theory, on the other hand, uses the knowledge that fluids are composed of a large number molecules to describe why flows behave the way they do [19]. Each molecule is treated as a particle with a position and a velocity. All of the particles are then allowed to flow through the domain and collide with other particles, obeying classical mechanics. This process of streaming and collision, when averaged over the very large number of molecules in a system, gives a fluid its macroscopic properties of density, velocity, and temperature.

1.2.2.1 Microscopic Molecular Dynamics The most exact manner in which fluid flows can be numerically simulated is through the Molecular Dynamics (MD) approach. As the name implies, this method uses the actual dynamics of individual molecules, allowing each one to move and collide according to Newton's equations of motion. Potential functions are used to describe the interactions between molecules, and the many-body problem is solved through time, deterministically. However, realistic systems are comprised of a vast number of molecules, and these simulations quickly become massive in size and computational difficulty. Consequently, only very small systems, with limited numbers of molecules, are capable of being modeled with current computational resources. As computing power increases, these simulations will become more powerful as they take into account the real system dynamics in a molecular context. At this time though, the MD approach is simply not feasible for macroscale flow simulations. Furthermore, from the perspective of macroscale dynamics, the great detail captured in MD simulations is, to a large extent, unnecessary.

1.2.2.2 The Mesoscopic Lattice Boltzmann Model To reduce the complexity of the MD models, mesoscopic approaches are being developed. A mesoscopic model describes behaviors in between the macroscopic and the microscopic. Instead of completely neglecting molecular interactions or meticulously accounting for the motion of each molecule, a mesoscopic model deals with the averages of molecular behaviors. This concept is fundamental to the field of statistical mechanics. Pioneered by Ludwig Boltzmann in the second half of the 17th century, statistical mechanics claims that given the extremely large number of particles in a macroscopic system, not only is a statistical approach necessary, but it is also more appropriate. The information lost through these assumptions is negligible in regard to the overall system dynamics while the reduction in computational difficulty is immense. The lattice Boltzmann method (LBM) was developed from this perspective. Starting from the MD approach described above, the individual molecules can be lumped into groups, and only allowed to move in predefined directions. Each group can then be represented by functions of the probability that it exists at a certain location and time, with a particular velocity. The evolution of those functions through space and time is described mathematically by the Boltzmann transport equation (BTE). The power of the LBM to solve complex flows is only

beginning to be recognized. Its potential is evidenced by the interest forming in industry for simulations based on these models. For instance, Porsche AG recently formed a partnership with Exa Corporation, one of the sole providers of commercial LB CFD code, for use in their product development process [20]. The LBM is now being applied to problems involving flows in porous media, binary and ternary flows, microfluidics, particulate and suspension flows, and even rarefied gas flows [21–25].

This rapid growth in interest is due to some key differences between the LBM and conventional finite difference and finite volume-based CFD techniques. The use of a method rooted in kinetic theory leads to phase separation that occurs spontaneously through particle interactions. This alleviates the need for the complex and computationally expensive interface tracking algorithms described above. Furthermore, in the LBM, the pressure is obtained locally at every lattice point from an equation of state, rather than through the solution of Poisson’s equation. This represents an enormous parallelization advantage over what is, in traditional CFD approaches, a global process. Finally, the convection operator is linear in the LBM, avoiding a major source of numerical instability and complication.

1.3 VOIDS IN THE LBM FIELD

Despite the many advantages of the LBM, the vast majority of multiphase research utilizing the LBM has focused on isothermal flows. In fact, most studies do not consider the energy equation in any form. A search in Scopus reveals that of the articles discussing the lattice Boltzmann method, nearly 90% of them do not even mention thermal effects [26]. Furthermore, those simulations that do acknowledge thermal variations typically do not use a correct representation of the temperature [27–29]. They rely instead on a simplified equation of state (EOS), which is independent of the temperature, to incorporate phase separation. This makes it impossible to model real thermal systems, especially those that include the phase change processes that occur in two-phase heat exchangers. Recent work by Yuan and Schaefer [30, 31] has addressed this issue by incorporating realistic equations of state into the LBM. This has led to further research that implements a true temperature [32–35].

One particularly interesting area of investigation concerns the numerical approximation of the gradient operator used to calculate interaction forces between particles. In this work, a recently developed linear combination approximation is utilized for the first time with the Peng-Robinson EOS, the results of which are presented in Chapter 3.

While a real temperature is included in these models, the evolution of the temperature distribution is still neglected. As a result, an analysis of the phase change process using this methodology is still not possible. To remedy this shortcoming, a passive-scalar treatment of the temperature is implemented for the solution of the energy equation. This leads to a complication concerning the thermal dependence of wall wetting behavior in multiphase systems. Consequently, a new model for thermally-varying wall interactions is developed and implemented in the thermal, multiphase LB model. This work is detailed in Chapter 4.

Furthermore, while multiphase, multicomponent models have recently been considered [18, 36], thermal effects have not yet been incorporated into these models either. This is due largely to the increased complexity that is introduced by thermal models. Specifically, realistic system initialization is vital and the stable regions of the interaction parameters that control interparticle potentials become highly important. However, by neglecting real temperature profiles, these LB models are similarly incapable of analyzing realistic systems from even a qualitative perspective. In this work, a model is presented that can incorporate real thermodynamics in a multiphase, multicomponent system. This requires the determination of stability zones of interaction parameters, as well as a novel coupling of the particle velocities. The details of this methodology are presented in Chapter 5.

1.4 ORGANIZATION

Before delving into the numerical results from this project, it is first necessary to review the underpinnings of the lattice Boltzmann method. Chapter 2 covers the development of the standard LBM, including a discussion concerning boundary conditions and body force implementation. This material is largely considered to be standard practice in the LBM community and makes up the foundation of the LB models utilized here. Example results are

provided in these sections which were implemented as benchmarks to validate the underlying code of the more complex models developed in this work.

This overview is followed by a presentation of the extensions of the standard LBM. This includes a description of the methodology for phase and component interactions, as well as a discussion concerning thermal models. In each chapter, the generally accepted methodology and the results based on such, are presented. These are followed by specific, novel developments to the models and results unique to this work. Each subsequent chapter can, in general, be considered a systematic increase in the complexity of the LBM through the inclusion of more complex physical phenomena. The progression of the presented results will proceed as follows (asterisks denote novel work):

- I) Chapter 2: Single-phase, single-component, isothermal LBM (SPSC-IT)
 - a. Poiseuille flow simulation
 - b. Couette flow simulation
- II) Chapter 3: Multiphase, single-component, isothermal LBM (MPSC-IT)
 - a. Comparison of numerical schemes for the gradient operator
 - b. Binodal curves based on the Peng-Robinson EOS and the linear combination gradient approximation (LCGA)*
 - c. Static droplet and bubble simulations using the Peng-Robinson EOS and the LCGA*
- III) Chapter 4: Single-phase, single-component, thermal LBM (SPSC-T)
 - a. Pure conduction
 - b. Rayleigh-Bénard Convection
- IV) Chapter 4: Multiphase, single-component, thermal LBM (MPSC-T)
 - a. Wall interaction model development*
 - b. Flow boiling simulation*
- V) Chapter 5: Multiphase, immiscible, multicomponent, isothermal LBM (MPiMC-IT)
 - a. Static droplet simulation
 - b. Interparticle interaction parameter stability analysis*
- VI) Chapter 5: Multiphase, immiscible, multicomponent, thermal LBM (MPiMC-T)*
 - a. Static thermal conduction*

- b. Static droplet simulation*
- c. Thermocapillary migration analysis*

VII) Chapter 6: Conclusions and future work

2.0 THE LATTICE BOLTZMANN METHOD

Despite some common misconceptions, the Boltzmann equation itself is more fundamental than the traditional Navier-Stokes (NS) equations. The assumptions made in the derivation of common lattice Boltzmann schemes, such as first or second order truncations, are only simplifications used in the discretization process, no different than the modifications made to the NS equations for their numerical solution. While the most common LBM schemes are only capable of recovering the density and momentum at the level of NS dynamics for low Mach number flows (to the second order), this is by no means a constraint on the Boltzmann equation itself. For example, LB methods have recently been utilized to model compressible flows [37]. Indeed, alternative discretizations and numerical schemes can be chosen to improve the accuracy of the simulations. To avoid confusion on this point, the mathematical derivation of the lattice Boltzmann equation is presented here in a fully rigorous manner, following the work of Shan, et al. [38].

2.1 LINEARIZATION OF THE BOLTZMANN TRANSPORT EQUATION

The lattice Boltzmann method is based on the numerical solution of the Boltzmann transport equation (BTE). The BTE is a kinetic equation which describes the evolution of the particle distribution function (PDF), $f(\boldsymbol{x}, \boldsymbol{\xi}, t)$, in which $\boldsymbol{\xi}$ and \boldsymbol{x} are the particle velocity vector and spatial configuration vector, respectively:

$$\frac{\partial f}{\partial t} + \boldsymbol{\xi} \cdot \nabla_{\boldsymbol{x}} f + \frac{\boldsymbol{F}}{m} \cdot \nabla_{\boldsymbol{\xi}} f = \boldsymbol{\Omega}, \quad (2.1)$$

where the collision integral, Ω , represents the change in f due to interparticle collisions, \mathbf{F} is a force field, and ∇_x and ∇_ξ are the gradient operators in the configuration and velocity spaces, respectively. Because of the high dimensions of the distribution function and the complexity of the collision integral, direct solution of the full Boltzmann equation is a formidable task for both analytical and numerical techniques. Therefore, one of the most frequently used simplifications of the BTE is the linearization of the collision operator, first performed by Bhatnagar, Gross, and Krook (BGK) [39]. The BGK approximation assumes that the effect of the collision between particles is to drive the fluid in a linear fashion towards a local equilibrium state, $f^{(0)}$, i.e. $\Omega = -\lambda(f - f^{(0)})$. This approximation yields the Boltzmann-BGK equation:

$$\frac{\partial f}{\partial t} + \boldsymbol{\xi} \cdot \nabla_x f + \mathbf{a} \cdot \nabla_\xi f = -\frac{1}{\tau}(f - f^{(0)}), \quad (2.2)$$

where τ is the relaxation time, $\mathbf{a} = \mathbf{F}/m$ is the acceleration due to a field, \mathbf{F} , and the equilibrium distribution function (EDF), $f^{(0)}$, can be described by the Maxwell-Boltzmann distribution:

$$f^{(0)}(\mathbf{x}, \boldsymbol{\xi}, t) = \frac{\rho(\mathbf{x}, t)}{(2\pi\theta(\mathbf{x}, t))^{\frac{D}{2}}} \exp\left[-\frac{(\mathbf{u}(\mathbf{x}, t) - \boldsymbol{\xi})^2}{2\theta(\mathbf{x}, t)}\right]. \quad (2.3)$$

The macroscopic hydrodynamic variables are defined as the first N velocity moments of the PDF, i.e. density, ρ , is the zeroth moment and momentum, $\rho\mathbf{u}$, is the first moment of the PDF:

$$\rho(\mathbf{x}, t) = \int f \, d\boldsymbol{\xi} \quad (N = 0), \quad (2.4)$$

$$\rho\mathbf{u}(\mathbf{x}, t) = \int f \boldsymbol{\xi} \, d\boldsymbol{\xi} \quad (N = 1). \quad (2.5)$$

It is possible to derive higher order moments as well, which describe the energy evolution and momentum flux, but this is beyond the scope of this work and is well-detailed in the literature [38]. The first two moments are adequate to describe the hydrodynamic evolution of NS-level dynamics. This fact will be elucidated in the following section as the velocity space of the Boltzmann equation is discretized for the formulation of the lattice Boltzmann equation (LBE).

2.2 DISCRETIZATION OF THE BOLTZMANN-BGK EQUATION

There are two broad methods of discretizing the Boltzmann-BGK equation. Traditionally, the EDF is expanded as a Taylor series and truncated to the second order of the fluid velocity [40]. This approach was derived from the lattice gas automata (LGA), the precursor to the LBM [41, 42]. The order of the truncation was chosen *a posteriori* in order to recover the NS equations upon application of the coefficient-matching Chapman-Enskog multiscale analysis. While this methodology is utilized almost exclusively in the literature, it is not mathematically rigorous and is the cause of many of the misconceptions concerning the limitations of the LBM. Recently, the discretization procedure of the LBM was reformulated as a Hermite series expansion and truncation of the continuum Boltzmann-BGK equation, similar to the Grad 13-moment equation [38, 43]. In this manner, the discretization procedure is consistently defined. This process can be summarized as follows:

1. Projection of the PDF and EDF onto a Hilbert sub-space via their expansion as orthonormal Hermite polynomials in the velocity space;
2. Truncation of the PDF and EDF polynomials to the desired accuracy, which is determined by the number, N , of required velocity moments;
3. Application of a Gauss-Hermite (GH) quadrature for the truncated particle distributions and velocity moments, yielding the lattice Boltzmann equation (LBE) and the corresponding discrete expressions for density and momentum.

2.2.1 Projection onto a Hermite Basis and Truncation of the Polynomials

In order to solve Equations (2.2) - (2.5) numerically, they must first be mapped onto a discrete space. This can be accomplished by projecting $f(\mathbf{x}, \boldsymbol{\xi}, t)$ onto an orthogonal basis spanned by the Hermite polynomials. A Hermite basis is chosen because a velocity moment of degree N is completely resolved by the expansion coefficients up to that same order N . Thus, lower order moments are not affected by the truncation of higher-order terms [43]. The immensely beneficial consequence of this is that a PDF can be approximated by its projection spanned by the first N Hermite polynomials, while maintaining exact reproduction of its velocity

moments of orders less than or equal to N , just as if the full PDF, without truncation, were utilized in the calculation. The projection and truncation of f is expressed mathematically as:

$$\begin{aligned} f(\mathbf{x}, \boldsymbol{\xi}, t) &= \omega(\boldsymbol{\xi}) \sum_{n=0}^{\infty} \frac{1}{n!} \mathbf{a}^{(n)}(\mathbf{x}, t) \mathbf{H}^{(n)}(\boldsymbol{\xi}) \\ &\approx f^{(N)}(\mathbf{x}, \boldsymbol{\xi}, t) = \omega(\boldsymbol{\xi}) \sum_{n=0}^N \frac{1}{n!} \mathbf{a}^{(n)}(\mathbf{x}, t) \mathbf{H}^{(n)}(\boldsymbol{\xi}), \end{aligned} \quad (2.6)$$

where $\mathbf{a}^{(n)}$ and $\mathbf{H}^{(n)}$, both tensors of rank n , are the expansion coefficients and Hermite polynomials, respectively. The weight function associated with the Hermite polynomials, $\omega(\boldsymbol{\xi})$, is defined as:

$$\omega(\boldsymbol{\xi}) = \frac{1}{(2\pi)^{D/2}} \exp\left(\frac{\boldsymbol{\xi}^2}{2}\right), \quad (2.7)$$

where $\boldsymbol{\xi}^2 = \boldsymbol{\xi} \cdot \boldsymbol{\xi}$, and the expansion coefficients are given by:

$$\mathbf{a}^{(n)}(\mathbf{x}, t) = \int f(\mathbf{x}, \boldsymbol{\xi}, t) \mathbf{H}^{(n)}(\boldsymbol{\xi}) d\boldsymbol{\xi}. \quad (2.8)$$

Using the tensor expansion of $\mathbf{H}^{(n)}$, the first few expansion coefficients, which are identified as the hydrodynamic variables, can be obtained:

$$\rho = a^{(0)}, \quad (2.9)$$

$$\rho \mathbf{u} = \mathbf{a}^{(1)}, \quad (2.10)$$

$$\boldsymbol{\Pi} = \mathbf{a}^{(2)} - \rho(\mathbf{u}^2 - \boldsymbol{\delta}). \quad (2.11)$$

Here, it becomes clear why Equation (2.6) is valid. Due to the orthogonality of the Hermite polynomials, the first N velocity moments of the PDFs are only influenced by lower order Hermite coefficients. Therefore, truncation of the higher order terms (i.e. $\mathbf{a}^{(n>N)} = 0$), does not affect the accuracy of the first N moments. A similar procedure can be applied to the equilibrium distribution function, $f^{(0)}$, to obtain its truncated form and the associated expansion coefficients, $\mathbf{a}_0^{(n)}$. While this derivation will not be given in detail, it can be shown through a Chapman-Enskog analysis that, for the recovery of NS level dynamics, the order of truncation of the EDF must be one greater than the order of the velocity moments ($N + 1$). In other words, if momentum is required at the NS level ($N = 1$), the order of truncation

of the EDF should be two; if momentum flux and energy are desired, the truncation should be to order three. A detailed description behind this effect is presented in the seminal work by Shan, et al. [38]. Importantly, it can be seen that this result mimics that of the original coefficient-matching procedure utilized in most LBM analyses. For the simulation of the density and velocity fields with NS level dynamics, the zeroth and first velocity moments should be calculated using a second order truncation of the EDF.

2.2.2 Discretization of the Velocity Space via Quadrature

The truncated distribution function, $f^{(N)}$, which is a partial sum of the Hermite series, as shown in Equation (2.6), can be uniquely described by its values at a set of discrete nodes, or abscissae. The process of finding a minimum set of abscissae is based on the Gauss-Hermite quadrature. In short, the Boltzmann-BGK equation can be solved for $f^{(N)}$ by discretizing the velocity space as a set of velocities that correspond to the nodes of the GH quadrature.

The rules of the quadrature require the degree of precision of the quadrature, q , to be greater than or equal to $2N + 1$. The most commonly used lattice for 2-D simulations is the $D2Q9$ structure, as shown in Figure 1a, which corresponds to a GH quadrature with an algebraic degree of precision of five [38]. In 3-D, a fifth degree quadrature is also used, yielding the standard $D3Q19$ model illustrated in Figure 1b. In this notation, $DxQy$ represents the lattice structure in x dimensions with y discrete velocity directions, including the zeroth velocity.

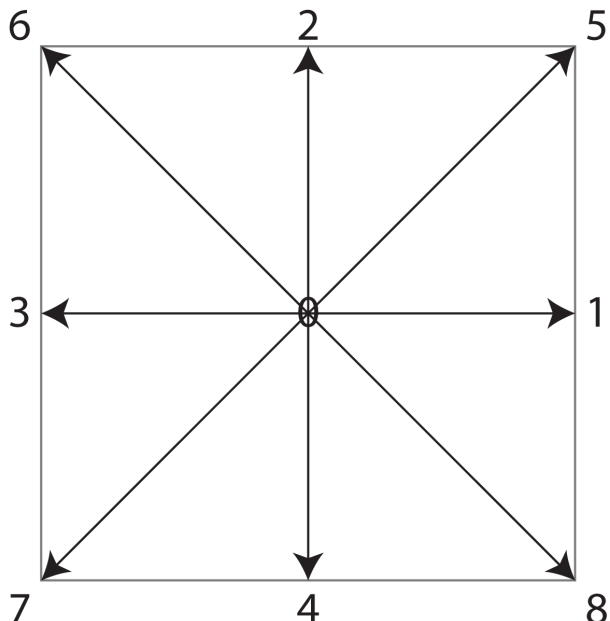
Applying a GH quadrature, the Hermite expansion coefficients can be expressed as:

$$\mathbf{a}^{(n)} = \sum_{\alpha=1}^d \frac{w_{\alpha}}{\omega(\boldsymbol{\xi}_{\alpha})} f^N(\mathbf{x}, \boldsymbol{\xi}_{\alpha}, t) \mathbf{H}^{(n)}(\boldsymbol{\xi}_{\alpha}), \quad (2.12)$$

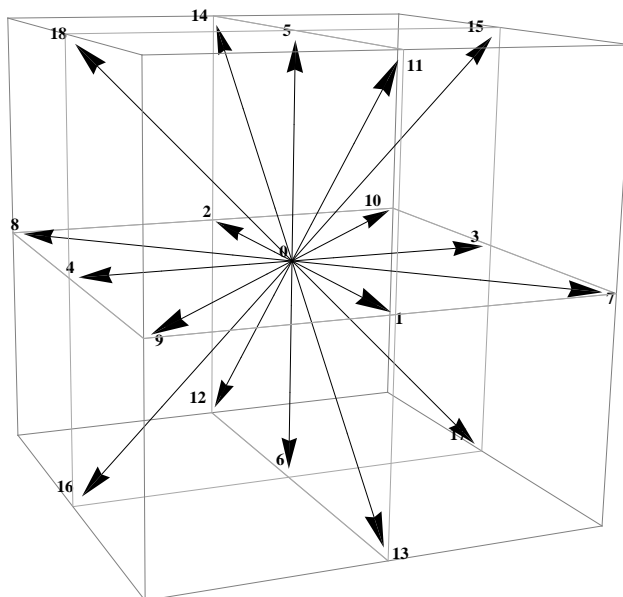
and defining $f_{\alpha}(\mathbf{x}, t) = \frac{w_{\alpha} f^N(\mathbf{x}, \boldsymbol{\xi}_{\alpha}, t)}{\omega(\boldsymbol{\xi}_{\alpha})}$, with $\alpha \in [1, d]$, where d is the number of discrete velocities, yields the following expressions for the macroscopic variables:

$$\rho = \sum_{\alpha=1}^d f_{\alpha}, \quad (2.13)$$

$$\rho \mathbf{u} = \sum_{\alpha=1}^d f_{\alpha} \boldsymbol{\xi}_{\alpha}. \quad (2.14)$$



(a) $D2Q9$



(b) $D3Q19$

Figure 1: The common lattice structures utilizing (a) nine velocities in two dimensions and (b) nineteen velocities in three dimensions (including the zeroth velocities).

The D2Q9 model, for example, has the following form of lattice velocities and weights for a lattice speed, $c = \Delta x / \Delta t$:

$$\boldsymbol{\xi}_\alpha = \begin{cases} (0, 0), & \alpha = 1; \\ (\pm 1, 0)c, (0, \pm 1)c, & \alpha = 2, 3, 4, 5; \\ (\pm 1, \pm 1)c, & \alpha = 6, 7, 8, 9. \end{cases} \quad (2.15)$$

$$w_\alpha = \begin{cases} 4/9, & \alpha = 1; \\ 1/9, & \alpha = 2, 3, 4, 5; \\ 1/36, & \alpha = 6, 7, 8, 9. \end{cases} \quad (2.16)$$

The discrete formulations of the EDF and force terms can be combined, i.e. $f_a^{(eq)} = f_a^{(0)} + \tau \mathbf{F}_a$, leads to the discrete Boltzmann-BGK equation:

$$\frac{\partial f_a}{\partial t} + \boldsymbol{\xi}_a \cdot \nabla_x f_a = -\frac{1}{\tau} [f_a - f_a^{(eq)}], \quad (2.17)$$

where the discrete form of the equilibrium distribution function is given as:

$$f_a^{(0)} = \omega_a \rho \left\{ 1 + \underbrace{\boldsymbol{\xi}_a \cdot \mathbf{u}}_{\text{1st}} + \underbrace{\frac{1}{2} [(\boldsymbol{\xi}_a \cdot \mathbf{u})^2 - u^2 + (\theta - 1)(\xi_a^2 - D)]}_{\text{2nd order}} + \dots \right\}, \quad (2.18)$$

for $u^2 = \mathbf{u} \cdot \mathbf{u}$ and $\xi_a^2 = \boldsymbol{\xi}_a \cdot \boldsymbol{\xi}_a$.

Finally, to solve these equations numerically, Equation (2.17) is discretized in space and time. While many discretization schemes can be implemented, the most common procedure is to first utilize forward differencing in time, followed by upwinding and downwinding for the convection and collision terms. This leads to the well-established, second-order form of the fully discretized LB equation [21, 40]:

$$f_a(\mathbf{x} + \Delta x, t + \Delta t) - f_a(\mathbf{x}, t) = -\frac{1}{\tau} [f_a(\mathbf{x}, t) - f_a^{(eq)}(\rho, \mathbf{u})], \quad (2.19)$$

where $\Delta x = \boldsymbol{\xi}_a \Delta t$ for a timestep of Δt . From a Chapman-Enskog expansion under the low Mach number assumption, it can be shown that this corresponds to the Navier-Stokes equations with a kinematic viscosity of [44]:

$$\nu = (\tau - \frac{1}{2}) c_s^2 \Delta t, \quad (2.20)$$

where c_s is the speed of sound in lattice units (LUs), and is equal to $c/\sqrt{3}$ for the D2Q9 and D3Q19 models. The specification of lattice units corresponds to the value of the variable in the lattice domain, as opposed to its value in physical units. This difference will become more clear in regards to the physical properties discussed in Section 2.6.

The procedure for solving Equation (2.19) is two-stage. First, the collision procedure is carried out, relaxing the current PDFs towards their equilibrium distributions:

$$\tilde{f}_\alpha(\mathbf{x}, t) = f_\alpha(\mathbf{x}, t) - \frac{1}{\tau} [f_\alpha(\mathbf{x}, t) - f_\alpha^{(eq)}(\rho, \mathbf{u})], \quad (2.21)$$

which is a purely local process. This is followed by the streaming step in which particles move along the lattice directions to neighboring nodes:

$$f_\alpha(\mathbf{x} + \Delta\mathbf{x}, t + \Delta t) = \tilde{f}_\alpha(\mathbf{x}, t). \quad (2.22)$$

In the streaming step, communication is only between nodes and their neighbors. This is contrary to the solution of the incompressible NS equations, which requires a global evaluation of the elliptic Poisson's equation for the pressure calculation. The concept of streaming and collision is a remnant of the lattice gas automata (LGA) on which the LBM was initially constructed. Based on the formulation presented here, it is possible to simply treat the LBM as the direct solution of discretized PDFs on the nodes of a numerical grid. In fact, if modifications are made to the spatial and temporal discretizations presented above, it becomes necessary to do so. However, the streaming and collision processes provide an analog to the underlying kinetic theory, and are therefore preserved when allowed by the numerical scheme.

2.3 HYDRODYNAMIC BOUNDARY CONDITIONS

Boundary conditions (BCs) present one of the great difficulties in all CFD simulations. Whether one is solving the Navier-Stokes equations or the Boltzmann transport equation, the specified values of the macroscopic properties along walls, inlets, and outlets can have a profound effect on both the accuracy and the stability of a simulation. In the LBM, BCs are further complicated by the need to translate between the macroscopic information and the particle distribution functions. While it is simple to determine macroscopic properties from PDFs using the equations shown in Section 2.2.2, there is no unique way to calculate PDFs from macroscopic properties. Consequently, an enormous variety of BCs have been developed for the LBM, and work is still ongoing to improve their accuracy [30, 36, 45, 46]. There is little consensus on which BCs are best, but an excellent overview of straight-wall BCs is presented by Latt and Chopard [47]. In order to advance the development of other aspects of the LBM, some commonly accepted BCs have been implemented here, which have been proven to work well for most simulations. Where possible, this work has been developed to allow the straight-forward implementation of other forms of BCs with minimal effort.

2.3.1 Solid Boundaries

Consider first a fluid node lying inside a domain, adjacent to a solid boundary. This node will have a set of PDFs, each associated with a specified velocity vector. As the streaming step is carried out, these PDFs will flow away from this node, into nodes that lie in the directions of the velocity vectors. At the same time, PDFs from the surrounding nodes will flow into this node. However, the PDFs coming from a solid boundary node are unknown. It is these values that must be determined by the boundary conditions.

There are two primary classes of solid wall boundary conditions, dry-node and wet-node. In dry-node conditions, the boundary node is part of the solid and therefore its PDFs do not evolve with the flow. In wet-node BCs, the boundary nodes where the PDFs are modified are part of the fluid domain. As such, these PDFs are associated with macroscopic

fluid properties and they participate in the flow dynamics of the simulation. The primary difference between these two methods is the physical location of the boundaries.

2.3.1.1 Dry-node BCs Dry-node BCs represent the classic boundary conditions of the LBM. The full-way bounce-back condition (FWBBC) and the halfway bounce-back condition (HWBBC) belong to this class of BCs. In the FWBBC, the collision step of the LBM is modified. At a boundary node, the PDFs that would typically stream from it are unknown since the node is a solid. Thus, any PDFs that are coming into the boundary node are reflected directly backward. As such, the PDFs coming into a fluid node from boundary nodes are the PDFs that were previously flowing from that fluid node, towards those boundary nodes. In this manner, any PDFs that would have been entering the domain that are unknown are replaced with PDFs that would have been leaving the domain, conserving mass and momentum at the boundary. This BC is extremely easy to implement as it is independent of wall orientation, and it successfully mimics the no-slip wall condition. However, it has been shown that the FWBBC is only first order accurate, which leads to the degradation of the accuracy of the otherwise second order accurate LBM [30, 48].

The HWBBC corrects this issue by placing the boundary halfway between the boundary nodes and the fluid nodes. In this way, the PDFs that would be leaving the domain in the streaming step are copied to the PDFs that are flowing in the opposite direction, which would have otherwise come from the boundaries and been unknown. This corresponds to a modification of the streaming step. The HWBBC introduces a dependence on the wall orientation and creates a physical boundary that exists between two nodes, but it maintains the second order accuracy of the simulation.

2.3.1.2 Wet-node BCs The intention of wet-node BCs is to capture the second order accuracy of the HWBBC, while preserving the on-site boundary condition of the FWBBC. This becomes possible due to the treatment of the boundary node as part of the fluid. In this configuration, a boundary node will have macroscopic properties, such as density and velocities, which can be set to the desired boundary condition values. There are a number of wet-node BCs, but the Zou-He BC (ZHBC) is used in this work [46]. The ZHBC only

replaces the unknown PDFs, leaving the rest unmodified. This construction corresponds to a fictitious fluid element outside of the domain that streams into the boundary node in order to elicit the correct hydrodynamic conditions at that boundary node. A full description of the formulation and implementation is given by Zou and He [46], as well as by Latt and Chopard [47], and will not be repeated here. However, it is important to note that this BC was chosen for its local nature (only PDFs at the local node are required) and its explicit form in both two and three dimensions. The ZHBC has been shown to be stable at moderately low Reynolds numbers and is second order accurate on straight wall boundaries.

2.3.2 Open Boundary Conditions

In addition to wall BCs, open BCs are also needed for flow simulations. The periodic boundary condition is the easiest BC to implement, and it can be applied directly to the post-collision PDFs as:

$$f_\alpha(\text{inlet}) = f_\alpha(\text{outlet}) \quad \forall \alpha \in [1, d]. \quad (2.23)$$

Similarly, zero derivative and extrapolation BCs can be implemented directly:

$$\text{Zero Derivative : } f_\alpha(i=1, j) = f_\alpha(i=2, j), \quad (2.24)$$

$$f_\alpha(i=nx, j) = f_\alpha(i=nx-1, j), \quad (2.25)$$

$$\text{Extrapolation : } f_\alpha(i=1, j) = 2f_\alpha(i=2, j) - f_\alpha(i=3, j), \quad (2.26)$$

$$f_\alpha(i=nx, j) = 2f_\alpha(i=nx-1, j) - f_\alpha(i=nx-2, j), \quad (2.27)$$

for an inlet at $i = 1$ and an outlet at $i = nx$.

For a fixed velocity inlet condition, the HWBBC can be modified to add momentum to each PDF flowing into the domain to achieve the desired velocity condition. This will result in an inlet boundary halfway between the first fluid node of the domain and one fictitious boundary node external to the domain. The boundary node PDF is calculated as:

$$f_{\bar{\alpha}}(\text{boundary}) = f_\alpha(\text{fluid}) + 2w_\alpha\rho \frac{3}{c^2} \mathbf{e}_{\bar{\alpha}} \cdot \mathbf{u}(\text{inlet}), \quad (2.28)$$

where, $\bar{\alpha}$ is the velocity vector flowing into the domain, and α is the vector flowing in the opposite direction, as shown in Figure 2 [36].

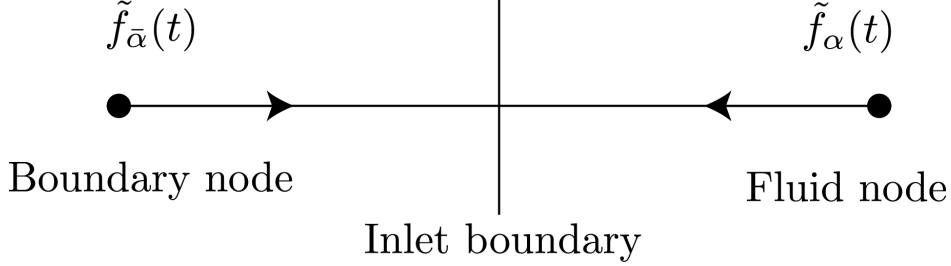


Figure 2: Inlet boundary layout.

2.4 FORCES: THE EXACT DIFFERENCE METHOD

Implementation of forces in the LBM is vitally important. Not only are external forces universal in any flow field, but as will be shown in later sections, the separation of phases and components in the LBM is introduced through the existence of interparticle forces. It must first be stated that there is ongoing debate about the best method of incorporating forces into the LBM [49–53]. Until recently, the shifted velocity method has been the most common approach. In this method, before the collision step, the forces are implemented by adding momentum to each particle via a shift of the velocity used to calculate the equilibrium distributions:

$$\mathbf{u}^{eq} = \mathbf{u} + \tau \Delta \mathbf{u}, \quad (2.29)$$

where $\Delta \mathbf{u} = \mathbf{F} \Delta t / \rho$. However, Kupershtokh has shown that this is effectively a first order method, and to maintain the second order accuracy of the LBM, forces should instead be implemented through a shift in the distribution function [54]. This method, known as the Exact Difference Method (EDM) gives the following form to the discrete LBE:

$$f_{\alpha}(\mathbf{x} + \Delta \mathbf{x}, t + \Delta t) = f_{\alpha}(\mathbf{x}, t) - \frac{1}{\tau} [f_{\alpha}(\mathbf{x}, t) - f_{\alpha}^{(eq)}(\rho, \mathbf{u})] + \Delta f_{\alpha}, \quad (2.30)$$

where,

$$\Delta f_{\alpha} = f_{\alpha}^{(eq)}(\rho, \mathbf{u} + \Delta \mathbf{u}) - f_{\alpha}^{(eq)}(\rho, \mathbf{u}), \quad (2.31)$$

and $\Delta \mathbf{u}$ is calculated in the same manner as the velocity-shifting method. In this manner, Kupershtokh found that a system at equilibrium, if exposed to a short pulse of a uniform

force, will remain at equilibrium, but with a velocity increase of $\Delta\mathbf{u}$, as expected [54]. Furthermore, the EDM was shown to remove the erroneous dependence of the density on relaxation time [34, 53]. It should be noted however, in the case of $\tau = 1$, the EDM and the traditional velocity shifting method are equivalent.

Any number of forces, such as those which occur at the contact lines at walls (\mathbf{F}_w), the forces that result from interparticle interactions ($\mathbf{F}_{a,a}$), and the forces which arise due to surface tension variations, can be incorporated in the same way [30, 36]. A body force, for instance, takes the form:

$$\mathbf{F}_b = \rho(\mathbf{x})\mathbf{a}, \quad (2.32)$$

where \mathbf{a} is the acceleration in lattice units. Forces can be summed to determine the total force acting on the system:

$$\mathbf{F}_{total} = \mathbf{F}_w + \mathbf{F}_{a,a} + \mathbf{F}_b + \dots, \quad (2.33)$$

which is then easily incorporated into the LB model through the EDM. At this point, the LBM is capable of simulating a single-phase, single-component, isothermal flow with wall interactions and forcing. In order to validate this base code, analytic Poiseuille and Couette flow benchmarks are considered.

2.5 SINGLE-PHASE, SINGLE-COMPONENT, ISOTHERMAL MODEL (SPSC-IT) RESULTS

Gravity-driven Poiseuille flow through a 2D slit is first simulated in order to verify the Zou-He wall condition, an open boundary periodic boundary condition, and the application of a simple body force to the standard LBM. The domain configuration for this simulation is illustrated in Figure 3. The analytic solution to this flow through a horizontal slit of width L , subjected to an acceleration, g , acting in the x-direction, is well known [55]:

$$U(y) = \frac{g}{2\nu} \left[\left(\frac{L}{2} \right)^2 - y^2 \right]. \quad (2.34)$$

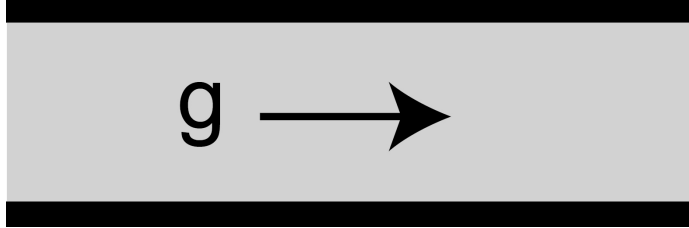


Figure 3: Domain configuration for gravity-driven Poiseuille flow through a 2D slit.

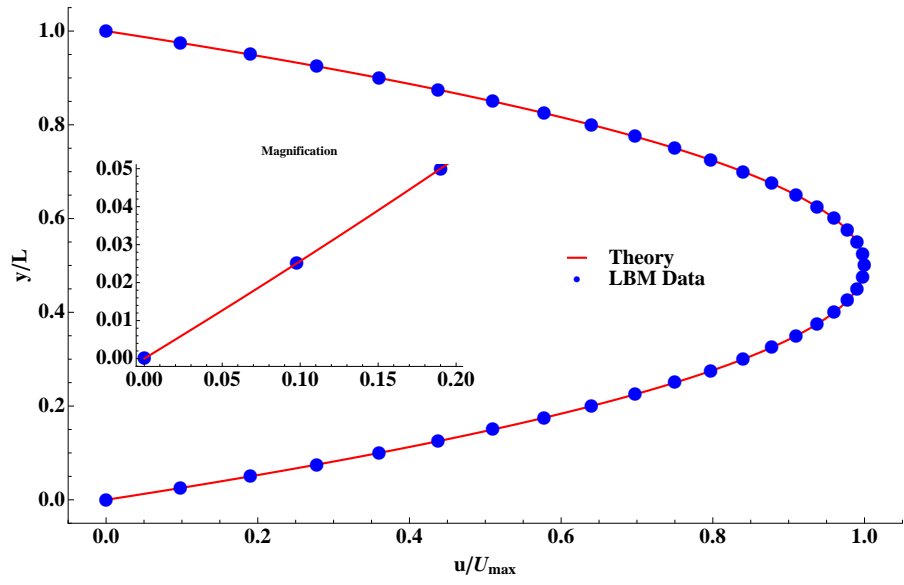
The theoretical result (—) and the simulated data (●) are shown in Figure 4a. As can be seen, the reproduction of gravity-driven Poiseuille flow is excellent. Additionally, the no-slip condition is well defined on the boundary node by the Zou-He BC, as highlighted by the magnified inset of the velocity profile near the wall. Pressure-driven Poiseuille flow is also simulated to confirm the ability to introduce a pressure gradient along a channel. Figure 4b displays the L2-norm residual error associated with the refinement of the lattice. The residuals converge as lattice resolution is increased as expected, proving the existence of grid independence of the simulation. Furthermore, the slope of the residual line on a log-log plot is also analyzed and it is verified that the simulation numerics are of second order.

Next, to validate a moving boundary, shear-driven Couette flow is simulated, again for a 2D slit, as shown in Figure 5. In Figure 6a, the velocity profiles at $x/L = 0.5$ are shown as the flow develops through time from rest to the linear solution that is expected. The final result, shown in Figure 6b, matches the analytic solution:

$$U(y) = U_{wall} \frac{y}{L}, \quad (2.35)$$

for a slit of width L and a wall moving at a speed of U_{wall} in the x-direction.

These simulation results are based on established techniques and are shown here purely as a validation and verification that the base LBM implementation is performing properly. It is on this base that further functionality is built for the simulation of more complex flow phenomena. The methodologies for these developments are described in the following chapters.



(a) Gravity-driven velocity profile

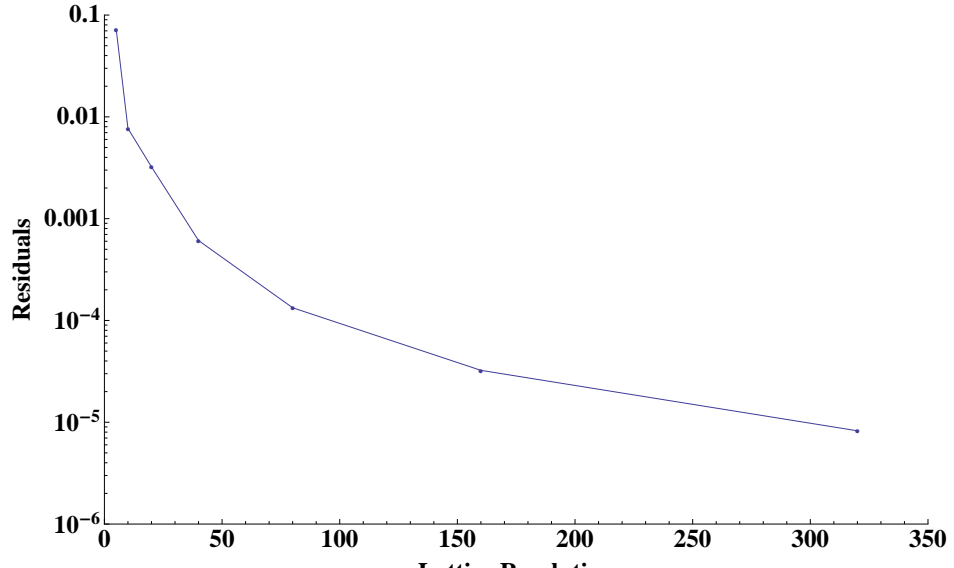


Figure 4: Velocity profiles of gravity and pressure-driven Poiseuille flows through 2D slits.



Figure 5: Domain configuration for shear-driven Couette flow in a 2D slit.

2.6 PHYSICAL TRANSLATION

Before delving into more complex models, it is worth a brief aside on the physical, non-dimensional, and lattice parameters that are used throughout this work. A more in-depth explanation of the differences between all of these values can be found in the literature [56]. In these simulations, some of the lattice parameters are fixed to common values. For instance, it is assumed that the spatial and temporal discretization parameters, Δx and Δt , are both unity. This preserves the notion of streaming and collision described in Section 2.2. Additionally, the relaxation parameter in the hydrodynamic LBE is often fixed to one. While these parameters can take on different values, these are common values used in LB simulations. However, this leads to some restraints when the lattice parameters are translated to the physical and non-dimensional units that describe real systems. First, the relationship between the relaxation parameter and viscosity implies, for $\tau = 1$, that:

$$\nu_{LU} = \frac{c_s^2}{2}, \quad (2.36)$$

where the subscript LU , describes a quantity in lattice units. The Reynolds number can then be expressed in terms of both lattice units and physical units as:

$$Re = \frac{u_p L_p}{\nu_p} = \frac{u_{LU} L_{LU}}{\nu_{LU}}, \quad (2.37)$$

where the subscript p denotes physical units, and u and L are characteristic velocity and length parameters, respectively. The lattice velocity can subsequently be replaced on the

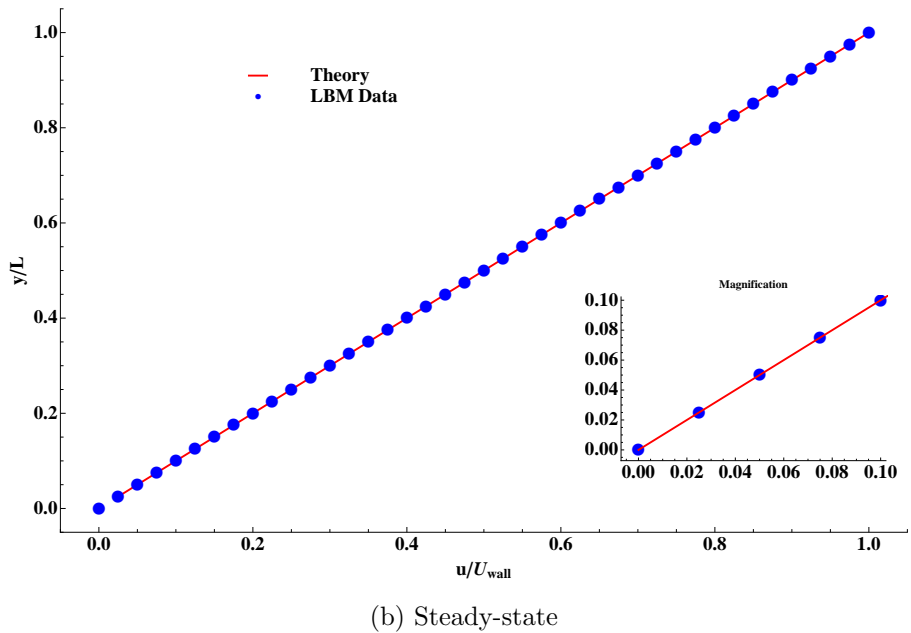
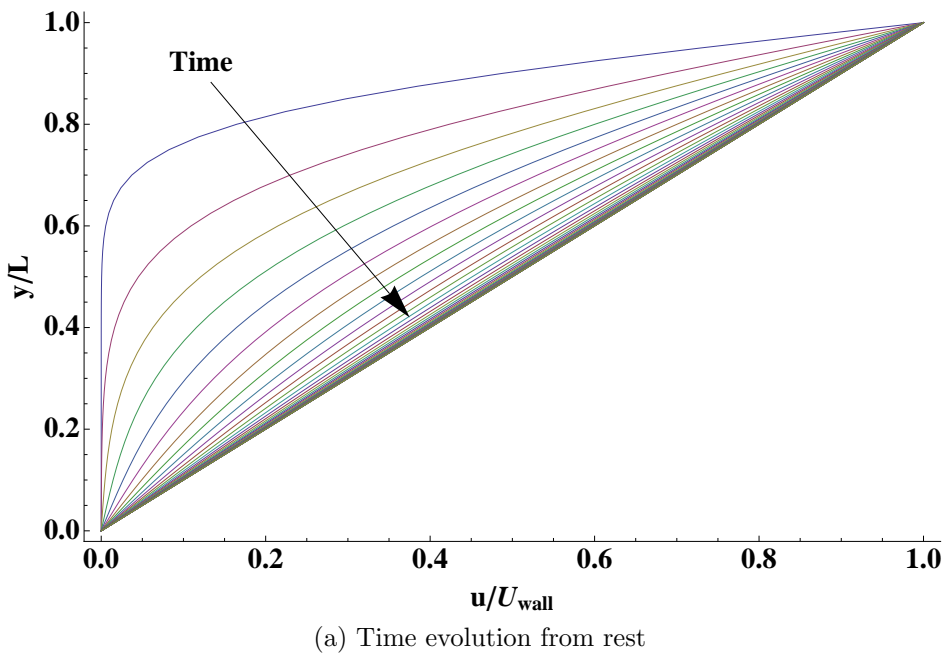


Figure 6: Velocity profiles of shear-driven Couette flow.

right-hand side by the lattice characteristic length divided by the lattice characteristic time, t_{LU} , yielding:

$$\frac{u_p L_p}{\nu_p} = \frac{L_{LU}^2}{\nu_{LU} t_{LU}}. \quad (2.38)$$

However, the length and time in lattice units can be represented by the discretization parameters, which are both fixed to one, and the viscosity in lattice units was specified in Equation (2.36). Therefore, for this configuration:

$$\frac{u_p L_p}{\nu_p} = \frac{2}{c_s^2}. \quad (2.39)$$

For the D2Q9 and D3Q19 models, $c_s^2 = 1/3$, which gives:

$$\frac{u_p L_p}{\nu_p} = 6. \quad (2.40)$$

Thus, if the substance is fixed, only the characteristic velocity or the characteristic length can be specified, with the other being automatically determined:

$$L_p = \frac{6\nu_p}{u_p}, \quad (2.41)$$

$$u_p = \frac{6\nu_p}{L_p}. \quad (2.42)$$

For example, if water with a kinematic viscosity of around $1 \times 10^{-6} m^2/s$ is considered, and a reference velocity of $0.1 m/s$ is used for that water flowing through a channel, the simulation will correspond to a channel width of $60 \mu m$. This is within the range of many of the previous numerical and experimental analyses of flow boiling phenomena, and is therefore implemented here [12, 17, 57]. This limitation is only present when the lattice parameters are fixed to these common values. It is possible to allow the parameters to vary, and the numerics in this work have been developed so that they may be modified, but doing so adds additional degrees of freedom which are not necessary for the results shown here. Furthermore, fixing these values ensures that the simulation remains in the low Reynolds and Mach number limits that are required to obtain the incompressible NS equations via the Chapman-Enskog analysis.

3.0 MULTIPHASE LBM

3.1 INTERPARTICLE POTENTIALS

While the LBM developed to this point can be used to simulate single phase flow with body forces, the power of the LBM lies in its ability to model more complex flows, such as those with multiple phases. As described in Chapter 1, phase separation, as well as the separation of immiscible components, occurs due to long-range molecular interactions. To incorporate these interactions into the LBM, many methods have been developed. The Shan and Chen (SC) model of interparticle pseudopotentials is the original method and is still the most versatile [21, 27, 58–60]. In the SC model, the interparticle potential in the long wavelength limit is defined as [58]:

$$V = \kappa g_f \psi^2, \quad (3.1)$$

where κ is a lattice-dependent parameter, g_f is a parameter which controls the strength of the interaction, and ψ is an effective mass. The effective mass can be related to the equation of state of the system through the thermodynamic pressure, p , as:

$$p = \rho R T + \frac{1}{2} g_f R T \psi^2, \quad (3.2)$$

where R is the universal gas constant and T is the temperature. In the original SC model, the effective mass is written for a simple, non-ideal equation of state as:

$$\psi_{SC} = \rho_0 \left[1 - \exp \left(\frac{-\rho}{\rho_0} \right) \right], \quad (3.3)$$

for a reference density, ρ_0 . However, this formulation corresponds to an equation of state in which the liquid phase is highly compressible [60]. To mitigate this problem, Yuan and

Schaefer developed a thermodynamically consistent model by calculating the effective mass using a pressure found directly from realistic equations of state [30, 31]:

$$\psi_{YS} = \sqrt{\frac{2(p(\mathbf{x}) - c_s^2 \rho(\mathbf{x}))}{c_0 g_f}}. \quad (3.4)$$

For the Peng-Robinson EOS used in this work, the pressure is:

$$p = \frac{\rho R T}{1 - b\rho} - \frac{a\alpha\rho^2}{1 + 2b\rho - b^2\rho^2}, \quad (3.5)$$

where $a = 2/49$, $b = 2/21$, and α is:

$$\alpha = \left[1 + (0.37464 + 1.54226\omega - 0.26992\omega^2) \left(1 - \sqrt{\frac{T}{T_c}} \right) \right]^2. \quad (3.6)$$

In these expressions, ω is the acentric factor of the substance and T_c the critical temperature. This model has been proven to greatly increase the ability of the LBM to simulate high density ratio, multiphase flows, previously a severe limitation of the SC model. Furthermore, Yuan and Schaefer have shown a large decrease in the spurious currents that typically plague many simulations based on the SC-LBM.

These two models can be compared more rigorously by considering the potentials that arise from each. Figure 7 shows the potentials for the SC and the YS models, as functions of the density. Also included is the simple case of $\psi = \rho$, which is often utilized in basic multiphase models. It is clear that the YS model gives a far more realistic form of the potential, whereas the other two models fail to predict the strong potential that should occur at higher densities. It is this aspect that is responsible for avoiding mass collapse in the LBM (i.e. the strong repulsive core effect).

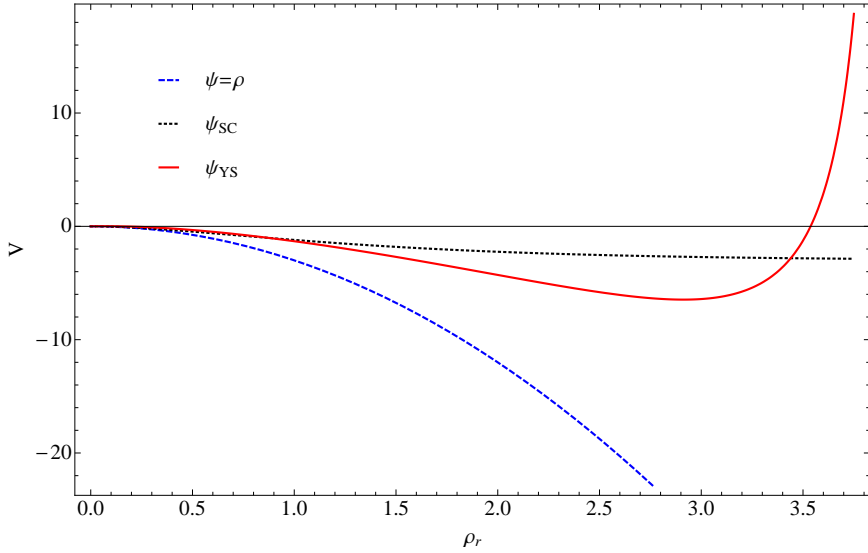


Figure 7: Comparison of different effective mass models used for calculating the interparticle interaction potentials.

3.2 GRADIENT OPERATOR DISCRETIZATION

In order to implement an interparticle potential into the LBM scheme, the force generated on each particle is calculated from the gradient of the potential function. This force can then be introduced into the LBM through the exact difference method described in Section 2.4. In order to solve for the force numerically, a finite difference scheme is used to discretize the gradient operator. However, the method in which this is implemented can vary. The most common approach is to first expand the gradient such that the force on a particle of type a , due to another particle, also of type a , is calculated as:

$$\mathbf{F}_{a,a} = -\nabla V, \quad (3.7)$$

$$= -\gamma \nabla \psi^2, \quad (3.8)$$

$$= -2\gamma \psi \nabla \psi, \quad (3.9)$$

where the lattice parameters and interaction strength parameter have been combined here, for simplicity, into a generic parameter, γ . The designation of particle type corresponds to

the chemical component. For instance, type a could refer to water, such that the force acting between two water particles is $\mathbf{F}_{a,a}$. This notation is extraneous in the discussion of single-component models, but will become important in later chapters. Thus, it is included here for completeness. The gradient in Equation (3.9) can then be discretized using a second order, central finite difference scheme. In two dimensions, this gives the following components of the force at node (i, j) :

$$F_x(i, j) = -2\gamma\psi(i, j) \left\{ c_1 [\psi(i + 1, j) - \psi(i - 1, j)] + c_2 [\psi(i + 1, j + 1) - \psi(i - 1, j + 1) + \psi(i + 1, j - 1) - \psi(i - 1, j - 1)] \right\}, \quad (3.10)$$

$$F_y(i, j) = -2\gamma\psi(i, j) \left\{ c_1 [\psi(i, j + 1) - \psi(i, j - 1)] + c_2 [\psi(i + 1, j + 1) - \psi(i + 1, j - 1) + \psi(i - 1, j + 1) - \psi(i - 1, j - 1)] \right\}. \quad (3.11)$$

It is clear that the force at node (i, j) is calculated using the value of the effective mass both at neighboring nodes, as well as the local node itself. This is in contrast to the direct evaluation of Equation (3.8), in which the value of ψ^2 would be determined at each node, leading to the calculation of the force using neighboring values alone:

$$F_x(i, j) = -\gamma \left\{ c_1 [\psi^2(i + 1, j) - \psi^2(i - 1, j)] + c_2 [\psi^2(i + 1, j + 1) - \psi^2(i - 1, j + 1) + \psi^2(i + 1, j - 1) - \psi^2(i - 1, j - 1)] \right\}, \quad (3.12)$$

$$F_y(i, j) = -\gamma \left\{ c_1 [\psi^2(i, j + 1) - \psi^2(i, j - 1)] + c_2 [\psi^2(i + 1, j + 1) - \psi^2(i + 1, j - 1) + \psi^2(i - 1, j + 1) - \psi^2(i - 1, j - 1)] \right\}. \quad (3.13)$$

These two methods, referred to as a local approximation and a mean value approximation, respectively, can both be easily implemented numerically. However, they yield different results, with different levels of stability. This is due to the fact that these gradients are evaluated at phase boundaries, and larger density ratios between phases correspond to larger gradients. Therefore, the gradient calculation can become unstable when local node information is neglected completely. Kupershtokh recently developed a method to combine the two approaches using a linear combination of the two approximations [53]. This leads to

greater stability and more accurate reproduction of a multiphase system through the use of a fitting parameter, A , that controls the contribution of each approximation:

$$\mathbf{F}_{a,a} = A\gamma_1\nabla\psi^2 + (1 - A)\gamma_2\psi\nabla\psi. \quad (3.14)$$

The generic parameters, γ_1 and γ_2 are used again for clarity, without loss of generality. These three methods, the local approximation, the mean value approximation, and the linear combination gradient approximation (LCGA), can be compared by implementing each one separately in the lattice Boltzmann scheme and simulating a liquid bar surrounded by its own vapor in a periodic domain. The size of the domain is chosen by first checking for grid-independence of the multiphase model. This is defined as the domain size at which the density ratio between the liquid and the vapor is constant with increasing grid resolution. As shown in Figure 8, a square domain with a side 50 lattice units (LUs) in length is sufficient to give a reasonable level of grid-independence, where a spatial lattice unit is defined as Δx , in this work equal to one. Once the simulation has converged to a steady-state, the equilibrium densities of the liquid and the vapor are examined. This simulation is performed for a variety of temperatures, allowing for the reconstruction of binodal curves. The results of this study are shown in Figure 9 for water, and are compared to the theoretical results calculated from Maxwell's equal area rule (EAR). It can be seen that the LCGA greatly improves the accuracy of the calculation. By maintaining a more accurate reproduction of the densities, the simulations also remain stable at lower temperatures. This is because the pure local approximation and the pure mean value approximation both lead to density ratios much larger than what physically occurs, resulting in the divergence of the method at higher temperatures. Furthermore, the use of the A fitting parameter in the linear combination gradient approximation allows the adjustment of the force for further improvement of the simulation results. Figure 10 shows a comparison of different values of A , and their effect on the reproduction of the binodal curve. The results shown here are the first implementation of Kupershokh's LCGA with the Peng-Robinson equation of state in an LBM simulation. A fitting parameter of $A = -0.225$ is found to yield accurate results for the PR-EOS based simulation. With this value, simulations at reduced temperatures below 0.6 are possible, and the accurate reproduction of density ratios beyond 1000:1 can be achieved.

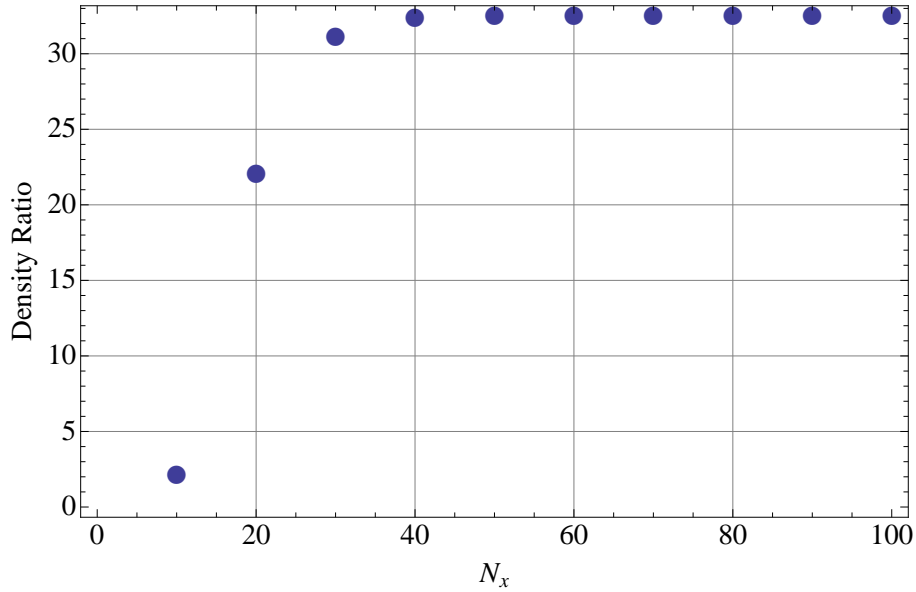


Figure 8: Grid-independence test of the multiphase model in a periodic domain showing the density ratio, normalized by the maximum density ratio, as grid resolution is increased.

Clearly, the linear combination approximation is a correlative method that relies upon comparison to theoretical data. Nevertheless, because the value of A is constant over the range of the conditions considered, this method provides an accurate approximation of the discrete gradient operator for this work. It is possible that more rigorous numerical schemes could be implemented for a stable approximation of the gradient at the phase boundaries, but with added complexity and computational cost [38, 53, 61]. For example, essentially non-oscillatory (ENO) and weighted essentially non-oscillatory (WENO) methods have been specifically developed for gradient calculations around discontinuities that arise at shock interfaces. These methods avoid the calculation of the gradient at the discontinuities by dynamically selecting numerical schemes with stencils that do not include the discontinuity. However, it should be noted that any discrete gradient operator must maintain sufficient isotropy to prevent the uncontrolled growth of spurious currents around the phase boundaries. For the purposes of this work, more complex schemes are not necessary.

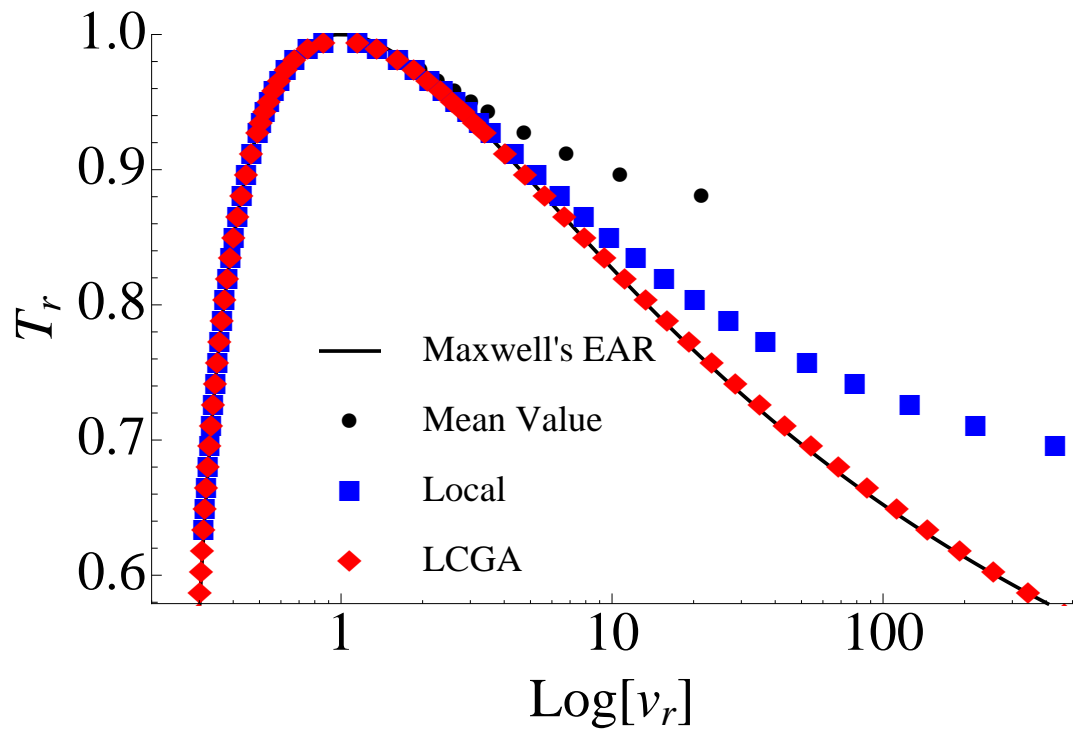


Figure 9: Comparison of different methods of approximating the gradient operator in the interparticle interaction force equation.

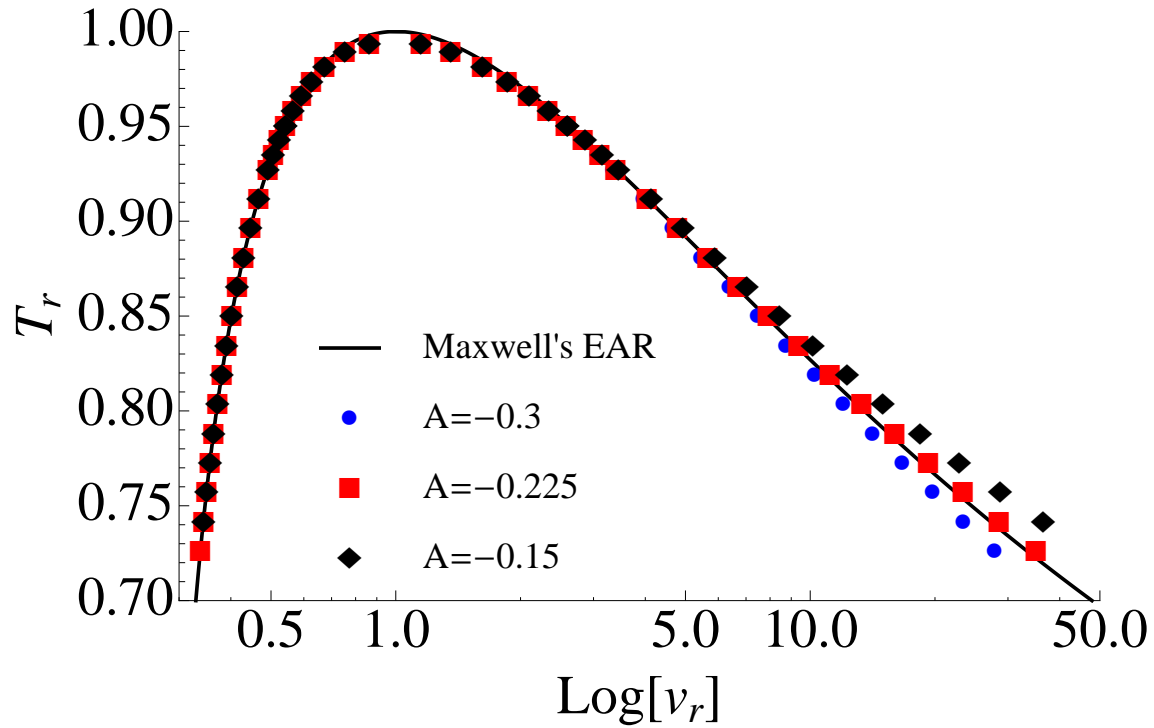


Figure 10: Comparison of different values of A used in the linear combination gradient approximation of the gradient operator in the interparticle interaction force equation.

3.3 MULTIPHASE, SINGLE-COMPONENT, ISOTHERMAL MODEL (MPSC-IT) RESULTS

The capability of the MPSC-IT model is demonstrated here by simulating a static droplet and bubble. The static droplet is modeled first with periodic boundary conditions in every direction. The system is initialized with a higher density region in the center of the domain. The initialization is performed by selecting the simulation temperature, then using Maxwell's equal area rule to calculate the pressure, p_r , the liquid density, ρ_r^L , and the vapor density, ρ_r^V , that correspond to the saturation conditions of a system at thermodynamic equilibrium [62]. These values represent the locations that an isotherm intersects the binodal coexistence curve of a pressure-volume (Pv) diagram, as shown in Figure 11. The radius of the droplet, r_0 , is subsequently chosen and the pressure is augmented within the droplet due to the effect of surface tension, σ_0 , following Laplace's Law [63]:

$$p_{in} = p_{out} + \frac{2\sigma_0}{r_0}. \quad (3.15)$$

The initial value of the surface tension can be determined by first neglecting any pressure difference and allowing a droplet to equilibrate. The radius and pressure difference can then be analyzed and used to calculate a value for σ_0 . The inclusion of this pressure increase in the initial state simply improves the speed of convergence because the size of the droplet will not change appreciably over the course of the simulation as it equilibrates. Similarly, if a non-circular region is specified, the droplet will minimize its surface energy and form into a circle, but initializing the domain with a circular droplet decreases the time to convergence. Figures 12a and 12b show the density and velocity plots, respectively, for the droplet. The nonzero velocities that can be seen surrounding the droplet are referred to as spurious currents and are common in multiphase models. These erroneous currents are a result of the anisotropy of the discrete gradient operator used for the calculation of the interparticle forces [38]. This becomes clear when a flat interface is considered, as the magnitudes of the spurious currents rapidly decrease to a negligible 10^{-9} . These currents are greatly reduced by using more advanced equations of state [31]. The currents shown in Figure 12b for example, are less than 10^{-2} in magnitude for a density ratio of 100. Similarly, a static bubble can be

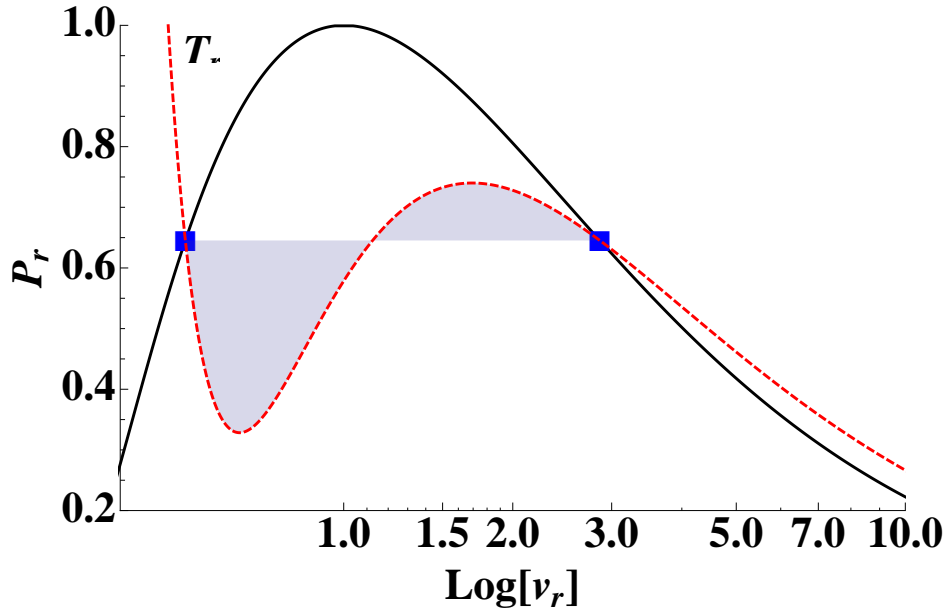


Figure 11: Pv diagram of the binodal curve (—) and an isotherm (---). Maxwell's equal area rule, represented by the equality of the shaded regions, is utilized to determine the saturation properties (■) used for the initial conditions of multiphase simulations.

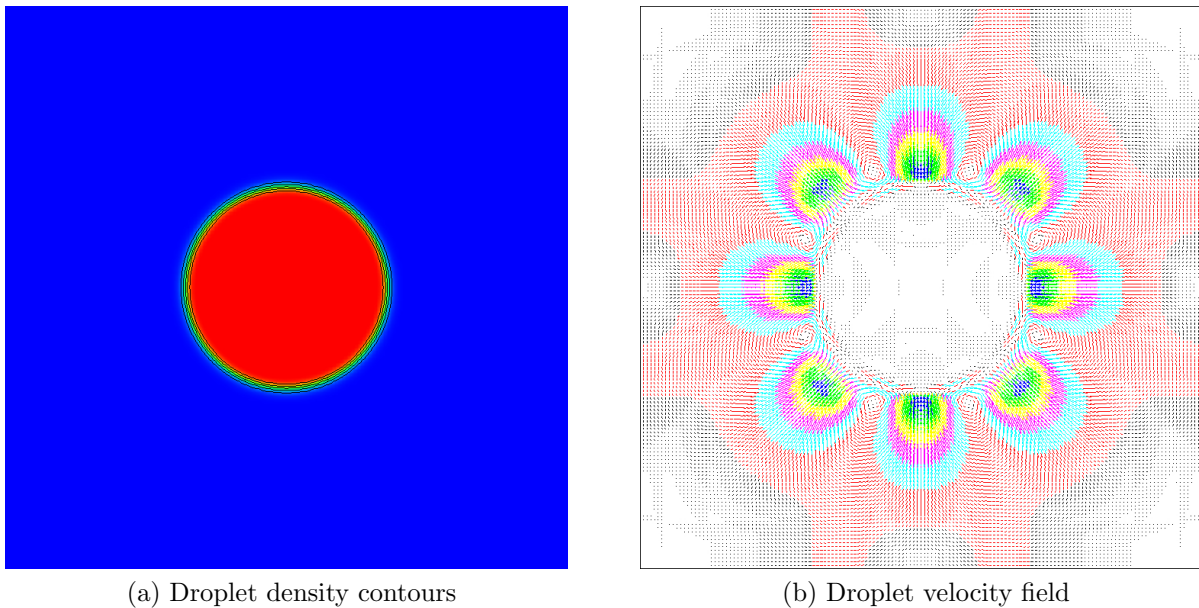
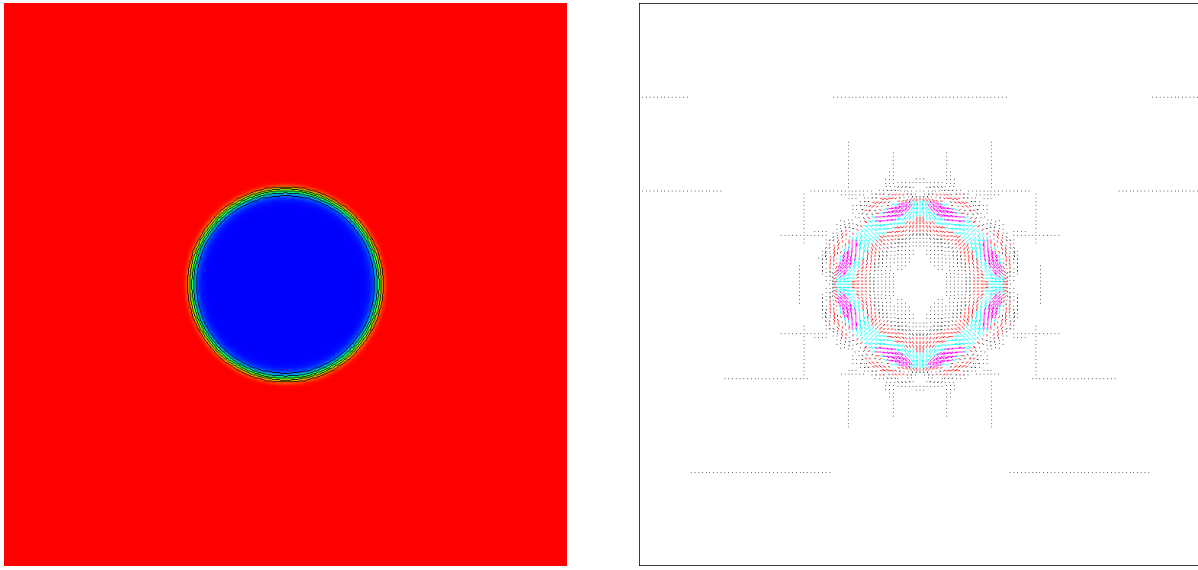


Figure 12: An isothermal, static droplet (red) at equilibrium with surrounding vapor (blue).



(a) Bubble density contours

(b) Bubble velocity field

Figure 13: An isothermal, static vapor bubble (blue) at equilibrium with surrounding liquid (red).

simulated by specifying a lower density inclusion surrounded by a higher density bulk fluid. Convergence to the steady state is rapid, as can be seen in Figures 13a and 13b. When comparing the vector fields of the bubble to those of the droplet, it can be seen that the spurious currents have a much larger effect in the low density phase. This is due to the fact that forces generated at the interfaces from the interparticle potentials will be of the same magnitude in both phases. However, when those forces are applied to the low density phases, there is a more significant effect.

This concludes the implementation of the multiphase model into the LBM. It has been shown that the combination of Kupershtokh's linear combination gradient approximation with Yuan and Schaefer's Peng-Robinson EOS formulation of the Shan-Chen interparticle interaction potential is capable of reproducing binodal curves accurately over a range of temperatures. However, thermal variations are not considered in these simulations. In the following chapter, the incorporation of thermal dynamics is presented.

4.0 THERMAL MODEL

The discussion has thus far focused only on the hydrodynamics of the system. However, thermal systems require an evaluation of the energy equation as well. There are a variety of methods in which thermal effects can be incorporated into the LBM. The most popular and straightforward approach is the passive-scalar method. In this approach, the temperature field is passively advected by the hydrodynamics of the system. Neglecting the viscous and compressive heating effects, as well as heat sources, the temperature, T , obeys the PDE:

$$\frac{\partial T}{\partial t} + \mathbf{u} \cdot \nabla T = \nabla \cdot (\hat{\alpha} \nabla T), \quad (4.1)$$

where \mathbf{u} is the macroscopic velocity and $\hat{\alpha}$ is the thermal diffusivity. Recognizing that the divergence of the gradient of a scalar is a scalar, and comparing this to Equation (2.2), the advantage of this approach becomes obvious. Due to the passive nature of the temperature field, this equation can be solved by the same method as the density by simply defining a second PDF corresponding to the temperature, $g_\alpha(\mathbf{x}, t)$, such that:

$$g_\alpha(\mathbf{x} + \Delta x, t + \Delta t) = g_\alpha(\mathbf{x}, t) - \frac{1}{\tau_T} [g_\alpha(\mathbf{x}, t) - g_\alpha^{(0)}(T, \mathbf{u})], \quad (4.2)$$

where τ_T is a dimensionless relaxation time corresponding to the rate at which the temperature dynamics approach their equilibrium. The thermal equilibrium PDF takes the same form as Equation (2.18) for a second order method:

$$g_\alpha^{(0)} = w_\alpha T \left[1 + \boldsymbol{\xi}_\alpha \cdot \mathbf{u} + \frac{1}{2} (\boldsymbol{\xi}_\alpha \cdot \mathbf{u})^2 - \frac{1}{2} u^2 \right]. \quad (4.3)$$

The temperature, as with the density, is then just the sum of the thermal PDFs:

$$T = \sum_{\alpha=1}^d g_\alpha, \quad (4.4)$$

and the thermal diffusivity can be defined for this formulation just as the viscosity was previously, giving:

$$\hat{\alpha} = (\tau_T - \frac{1}{2})c_s^2\delta t, \quad (4.5)$$

which leads to a variable Prandtl number of:

$$Pr = \frac{\nu}{\hat{\alpha}} = \frac{2\tau - 1}{2\tau_T - 1}. \quad (4.6)$$

It should be noted however, that to maintain the validity of this approach, the thermal dynamics of the system cannot be advected faster than the hydrodynamics will allow. Thus, the Prandtl number should be restricted to values less than or equal to one, or the simulation will become inaccurate and eventually unstable.

4.1 THERMAL FORCES

In the thermal LBM, gravity forces can lead to buoyancy-driven flow when there are temperature variations in the system. These effects can be implemented directly through a body force term under the Boussinesq approximation. For a single phase system [30]:

$$F_{buoy} = \rho(\mathbf{x})\beta g(T - T^*)\hat{j}, \quad (4.7)$$

where β is the thermal expansion coefficient, which can be calculated from the Rayleigh number (Ra) as:

$$\beta = \frac{\nu\hat{\alpha}Ra}{g\Delta T L^3}, \quad (4.8)$$

g is the acceleration due to gravity, $T^* = T_{wall} - y\Delta T$ is a reference temperature, assumed to be equal to the temperature at the pure conduction state, and \hat{j} is the direction in which gravity is acting, assumed here to be parallel to the y -axis. When multiple phases are present, the buoyancy force will include one term due to density differences of phases and another from density differences caused by thermal variations within each phase. Together, these can be approximated as [30]:

$$F_{buoy} = \rho(\mathbf{x})g \left[\left(1 - \frac{\langle \rho \rangle}{\rho(\mathbf{x})} \right) - \beta(T - T^*) \right] \hat{j}, \quad (4.9)$$

where $\langle \rho \rangle$ is the density averaged over the entire domain. These forces are then simply added to the total force expression shown in Equation (2.33) and incorporated into the LBM using the EDM described in Section 2.4.

4.2 THERMAL BOUNDARY CONDITIONS

There are two common choices for the thermal wall boundary condition: isothermal walls and constant heat flux walls. An excellent description of the derivation of the conditions is given by Bao [36], so only a brief overview will be given here. For an isothermal wall at temperature T_w , the unknown PDFs are assumed to take the form of their equilibrium distribution, as given in Equation (4.3), with an unknown temperature T' . This unknown temperature can then be determined using the prescribed wall temperature. For example, for the D2Q9 model shown in Figure 1a at a lower boundary, the expression becomes:

$$T' = \frac{6}{1 + 3v_y + 3v_y^2} (T_w - g_0 - g_1 - g_3 - g_4 - g_7 - g_8), \quad (4.10)$$

where the sum of the unknown PDFs has been replaced by the sum of their equilibrium distributions. Using the equilibrium distribution equation again with the value of T' , gives the unknown PDFs.

The constant heat flux case is based on the same methodology but first involves calculating the wall temperature from a specified temperature gradient at the wall. For instance, a second order one-sided finite difference scheme can be used:

$$\left. \frac{\partial T}{\partial y} \right|_{i,1} = \frac{4T' - T_{in} - 3T_w}{2\Delta y}, \quad (4.11)$$

where T_{in} is the temperature at the node one normal step into the domain, and Δy is the distance to that node. After solving this expression for T_w , this value can be used in Equation (4.10) to establish the boundary condition in the same manner as for the isothermal case.

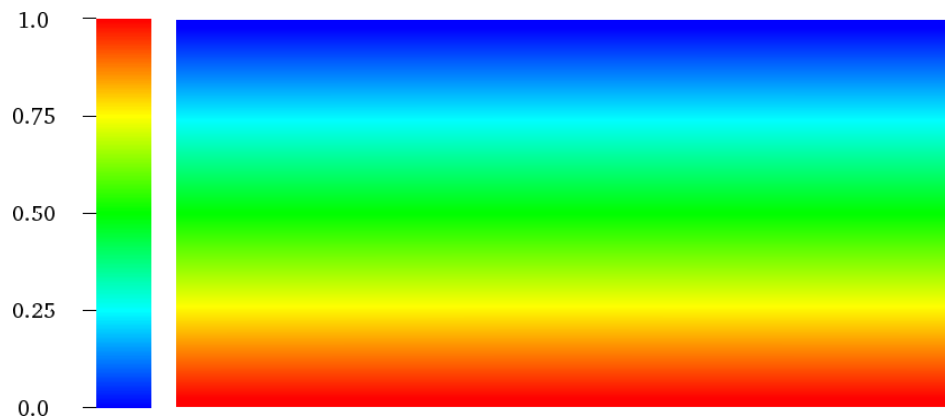
4.3 SINGLE-PHASE, SINGLE-COMPONENT, THERMAL MODEL (SPSC-T) RESULTS: RAYLEIGH-BÉNARD CONVECTION

Briefly returning to the single-phase model described in Chapter 2, a single-phase, single-component, thermal simulation can be performed for validation of the thermal model. In a multiphase model, the temperature and density are supplied to an equation of state for the calculation of the pressure, and this pressure is used for the determination of the intermolecular forces via an effective mass, ψ . In the single-phase model, however, these forces can be neglected. The only remaining interaction between density and temperature corresponds to the density differences that are a consequence of thermal variations, which are implemented as discussed in Section 4.1.

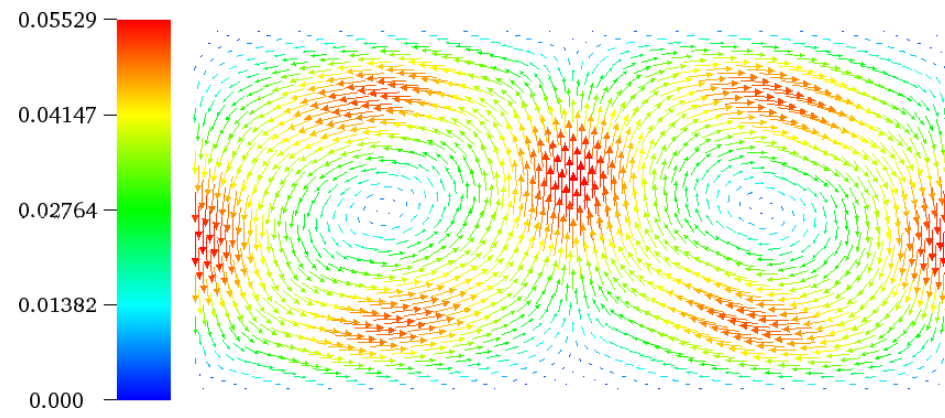
A standard benchmark for a single-phase thermal flow is Rayleigh-Bénard convection (RBC). In this configuration, a layer of fluid under the influence of gravity is placed in a 2D horizontal slit of height L , with the bottom wall fixed at a higher temperature than the top wall. When the Rayleigh number ($Ra = g\beta\Delta TL^3/\nu\alpha$) is small, the fluid will remain at rest, and the temperature profile will reflect the pure conduction state shown in Figure 14a. However, once a critical Rayleigh number is surpassed, any small perturbations will cause the onset of convection. Convection rolls, displayed by the velocity vectors in Figure 14b, will develop and the system will eventually find a steady state with a distinct temperature profile, depicted in Figure 14c. For the case of a 2D horizontal slit with periodic sides, the critical Rayleigh number determined from linear stability theory is $Ra_c = 1708$. Even with a coarse grid of 100×50 , the critical Rayleigh number of the LBM is found to be a very acceptable value of ~ 1715 .

4.4 MULTIPHASE, SINGLE-COMPONENT, THERMAL MODEL (MPSC-T) RESULTS: SPINODAL DECOMPOSITION

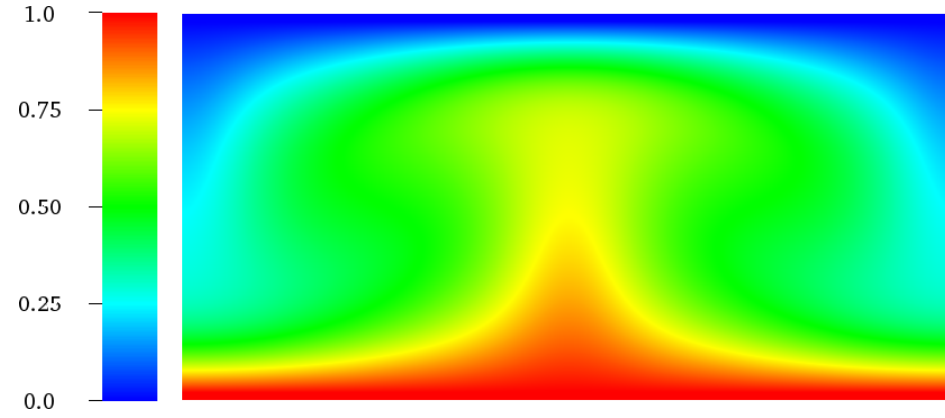
The next step is the reintroduction of the particle interaction forces for a multiphase, single-component, thermal model. The capability of this model can be shown by simulating the



(a) Temperature contours at $Ra = 10^3$



(b) Velocity vectors at $Ra = 10^4$



(c) Temperature contours at $Ra = 10^4$

Figure 14: Temperature contours and velocity vectors, given in lattice units, of pure conduction and Rayleigh-Bénard convection between a heated lower wall and a cooled upper wall with periodic BCs at the sides ($Pr = 1$).

spinodal decomposition process. This simulation is initialized by choosing an unstable density state equal to $0.9\rho_c$, plus or minus a small random perturbation. The consequence is the rapid segregation of distinct liquid and vapor phases. Figures 15a-15f and 16a-16f show the progression of this process through time for the isothermal and the thermal models, respectively. Recall that the isothermal model is based on the solution and evolution of the hydrodynamic lattice Boltzmann equation, involving the PDFs designated by f_α . However, in the isothermal model, it is assumed that the temperature used in the evaluation of the equation of state is always the same, and the thermal PDF equation for g_α is never solved. In the thermal case, conversely, both the hydrodynamic PDF equation (f_α) and the thermal PDF equation (g_α) are solved. Clearly, both models quickly move away from the unstable density, forming liquid and vapor regions. An initial value smaller than the critical density is used simply to bias the simulation so that droplets are formed in the final state, rather than bubbles, but any unstable initial density will lead to the decomposition process. Both models show the ability of the LBM to capture the phase change process. This is verified by calculating the total liquid and vapor masses in the domains through time, displayed in Figure 17a for the isothermal simulation and in Figure 17b for the thermal model. It can be seen that in both models mass is conserved. Furthermore, the change of phase from the unstable initial states, classified in the figures as pure vapor ($\rho_c < 1$), to separate liquid and vapor states, is clear in both cases.

The importance of the thermal model is elucidated through comparison of the two sets of results. In the isothermal model, droplets of liquid either rapidly shrink due to evaporation if they are below a critical radius, or grow due to condensation if they are above it. This is a consequence of the lack of a thermal barrier to the phase change process in the isothermal model. Realistically, when evaporation or condensation occurs, there is a slight temperature change at the inclusion surface due to absorption or release of latent heat. This acts as a stabilizing mechanism, slowing the phase change process. This effect is visible when the progression of the density contours of the isothermal and thermal models are compared, as evidenced by the longer residence times and greater stability of the small droplets in the thermal case (as noted by the circled droplets in each set of figures).

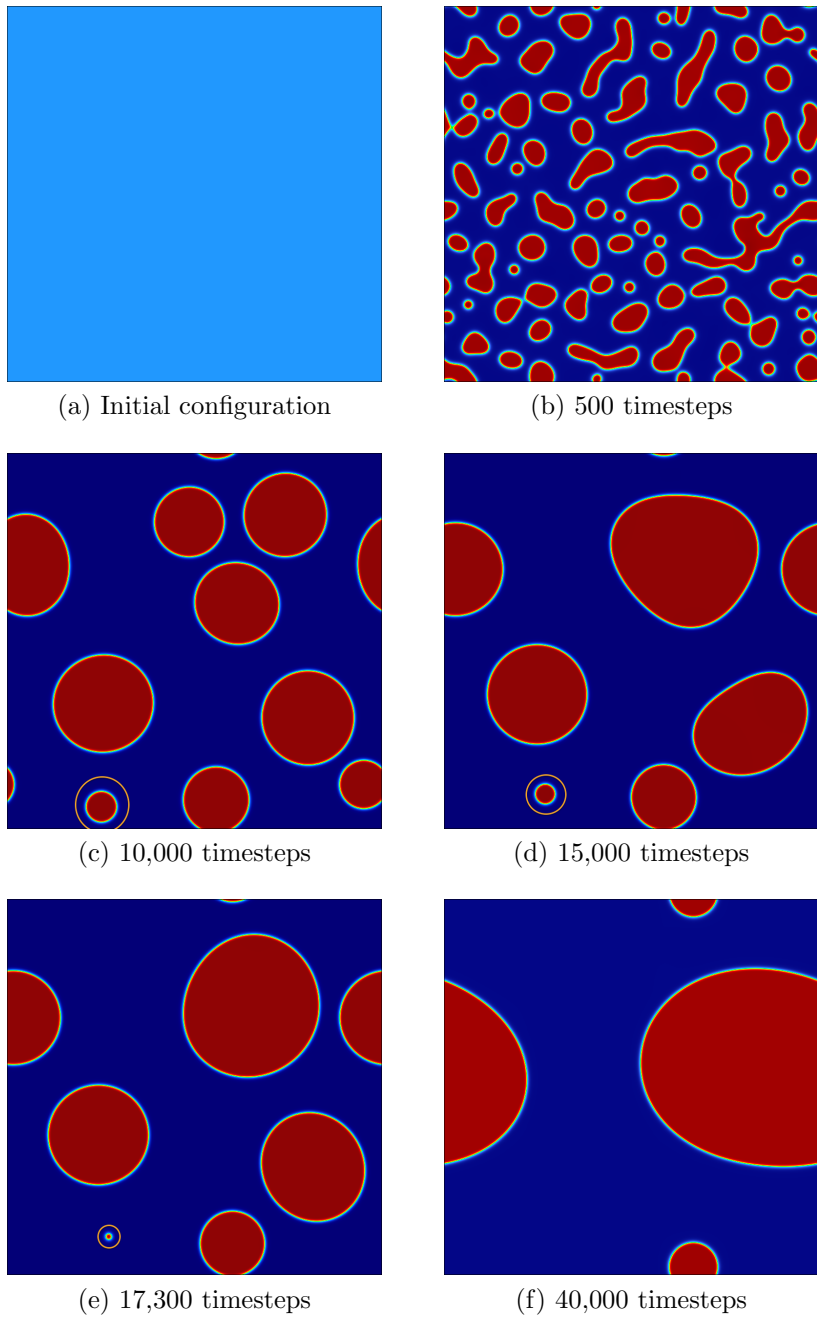


Figure 15: The spinodal decomposition process showing phase separation into liquid (red) and vapor (blue) due to an unstable density initialization evolved isothermally. Specific timesteps are chosen to highlight the short residence time ($< 10,000$ timesteps) of small drops, circled in (c)-(e).

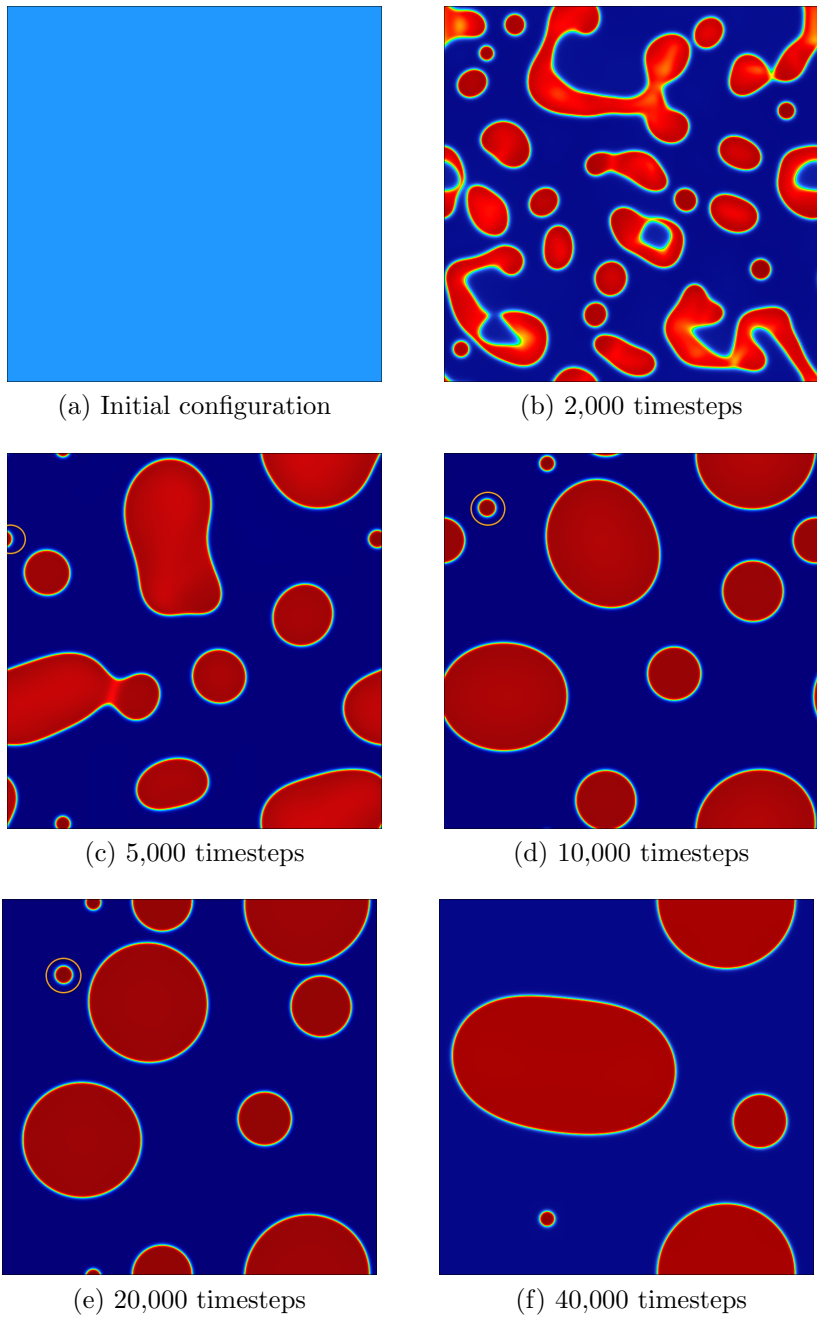
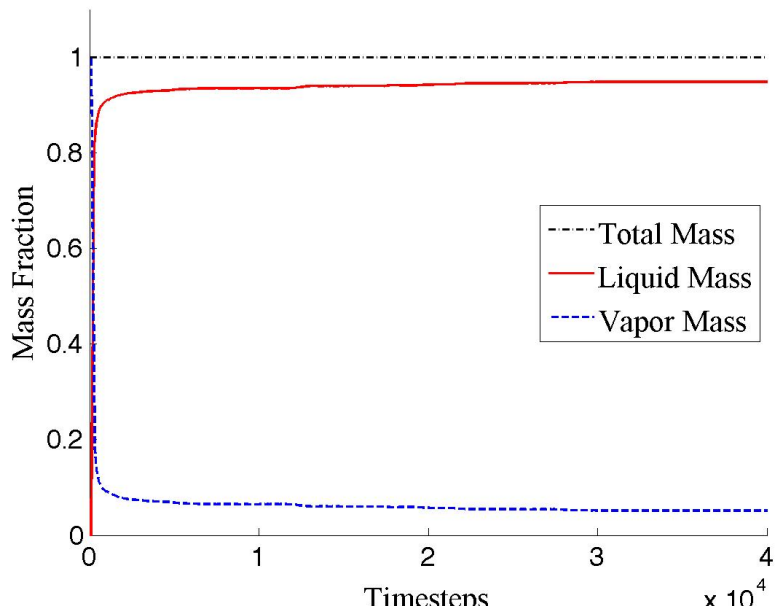
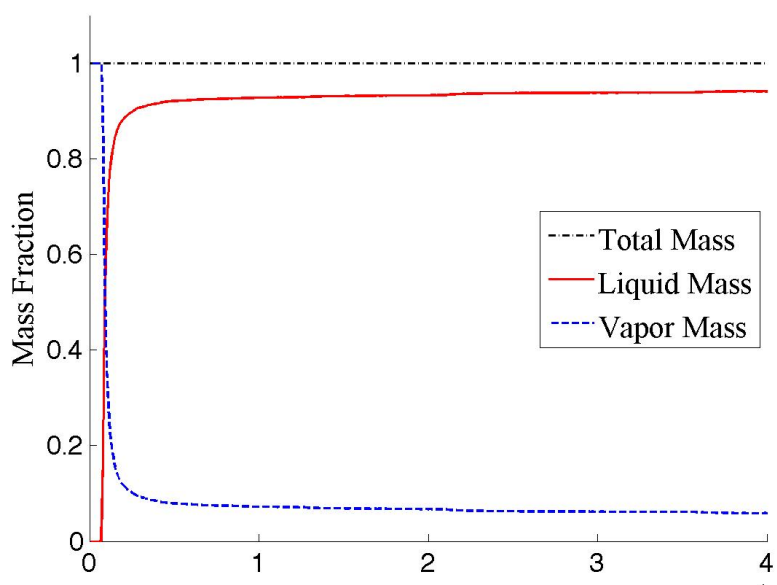


Figure 16: The spinodal decomposition process showing phase separation into liquid (red) and vapor (blue) due to an unstable density initialization evolved using the passive-scalar thermal model. Specific timesteps are chosen to highlight the long residence time ($> 15,000$ timesteps) of small drops, circled in (c)-(e).



(a) Isothermal Model



(b) Thermal Model

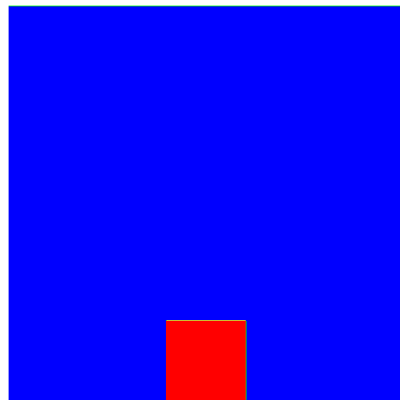
Figure 17: Evolution of the total mass, the liquid mass, and the vapor mass in the domain through time during the spinodal decomposition process (normalized by the total initial mass) for the isothermal and thermal models.

4.5 A NOVEL WALL INTERACTION MODEL

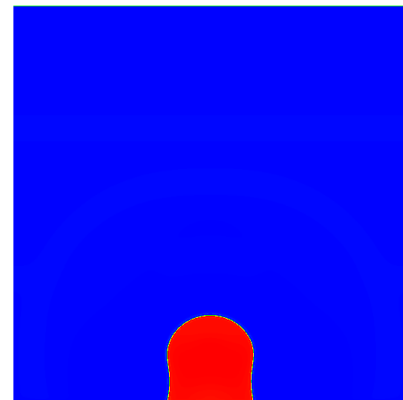
The thermal, multiphase model can also be analyzed in the presence of solid boundaries. However, this brings up an interesting complication when phase boundaries come into contact with walls. Consider, for instance, a 2D channel, periodic in the x-direction, with a droplet of liquid water resting on the bottom wall. The walls are treated using the Zou-He boundary condition in order to reproduce the no-slip condition at the wall. The domain is initialized by calculating the saturation liquid and vapor densities at a given temperature from the Peng-Robinson equation of state, then fixing a square section of the domain as liquid, with the surrounding area specified as vapor. The density contours of the progression of a typical simulation are shown in Figures 18a - 18d. As can be seen, the droplet minimizes its surface energy by forming a spherical cap shape as it wets the wall. The degree of wetting can be controlled in the LBM through an additional interaction force between the fluid particles and the wall. This force occurs thermodynamically due to the difference between the solid-liquid and the solid-vapor surface energies. The formulation of this force in the lattice Boltzmann model mimics the interparticle interaction forces used for phase separation:

$$F_w = \rho(\mathbf{x})g_w\nabla\rho_w(\mathbf{x}), \quad (4.12)$$

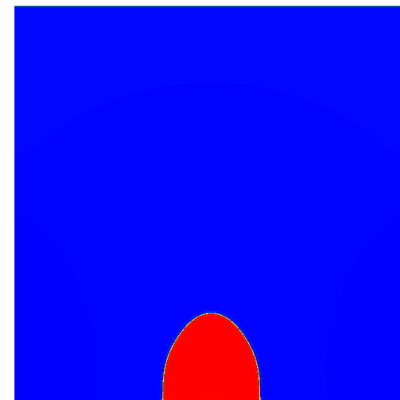
where the strengths of the interactions are controlled via a wall interaction parameter, g_w , and $\rho_w(\mathbf{x})$ is a binary value representing the existence (1) or absence (0) of the wall. This force is implemented one layer above the boundary nodes that are treated with the wet-node Zou-He boundary condition. In this manner, the force is not applied at the same nodes where the zero-velocity no-slip condition is enforced. This avoids the generation of a singularity, which would ultimately result in divergence of the simulation. As the grid resolution increases, the influence of this numerical consideration will be reduced. This can be seen by the grid independence evaluation of the contact angle measurements shown in Figure 19. Typically, the value of g_w is simply changed in order to demonstrate variability in wetting behavior. While this is adequate for an isothermal system, in order to model more complicated thermal problems, this parameter needs to be based on the local wall temperature, rather than fixed globally.



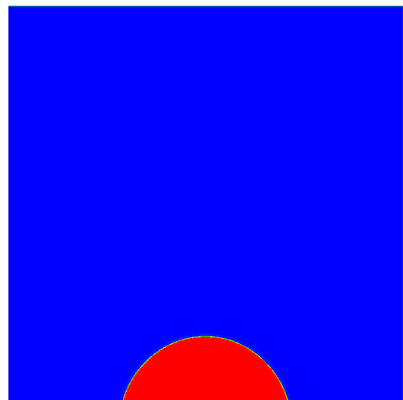
(a) Initial configuration



(b) 1,000 timesteps



(c) 2,000 timesteps



(d) 20,000 timesteps

Figure 18: Density contours showing the progression of a typical simulation of a droplet (red) wetting the bottom wall of a periodic 2D channel filled with vapor (blue) at various timesteps.

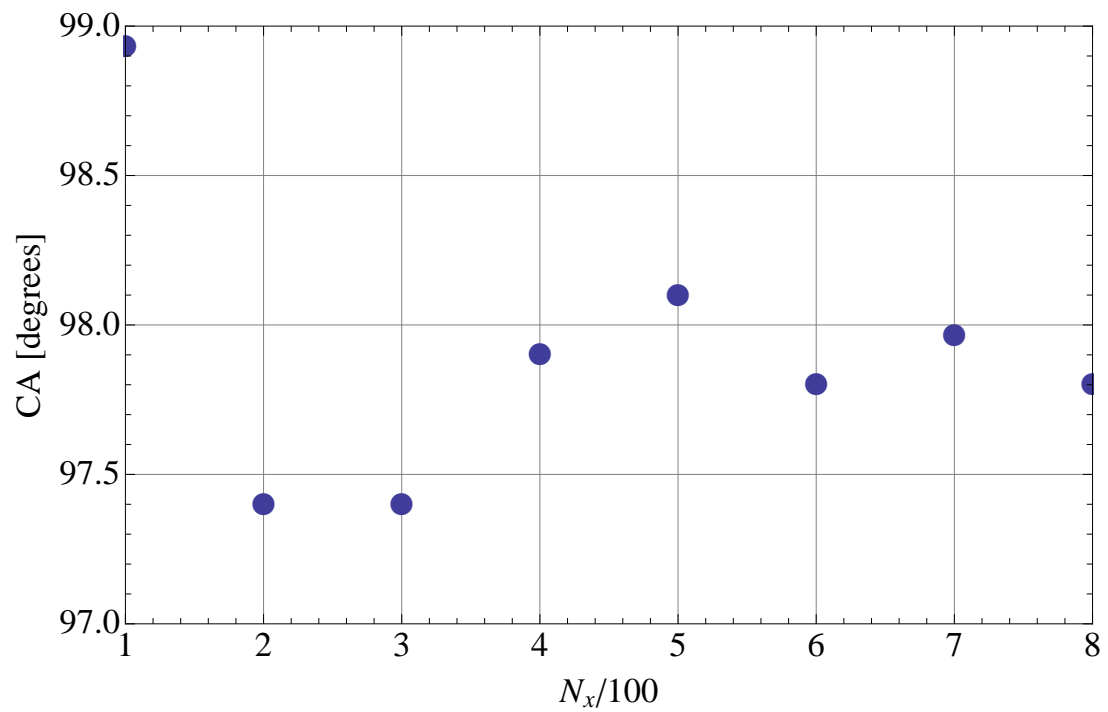


Figure 19: Grid independence of the contact angle measurement to within the measurement error ($< 1^\circ$).

The magnitude of this problem is shown in Figure 20. Here, two isothermal simulations are performed at two different temperatures. Although the difference is only $175K$, the contact angles that arise when each simulation is carried out using the same value for the interaction parameter are vastly different. For instance, if $g_w = 0.003$, the contact angle of the simulation performed at $450K$ is approximately 70° , whereas the contact angle at $625K$ is approximately 160° . This is an issue often neglected in LBM simulations, where g_w is typically left as constant, regardless of the wall temperature.

4.5.1 Wall Interaction Parameter Determination

To overcome this problem, it is necessary to calculate the wall interaction parameter based on the local temperature. This requires a function for the contact angle and a function for the wall interaction parameter, both with respect to temperature. In this work, a general second order polynomial is used for the contact angle [64]:

$$CA_{exp}(T) = A_{exp}T^2 + B_{exp}T + C_{exp}. \quad (4.13)$$

In this manner, the methodology remains substance independent, and the specific relationship can be chosen based on the fluid and solid pair to be modeled. To determine the relationship between the wall interaction parameter and the temperature, a large number of isothermal simulations are first carried out using a range of g_w values. The contact angles are measured once the simulation has converged to a steady state by first mapping the diffuse interface to a line at $\rho_r = 1$, then utilizing the NIH ImageJ Contact Angle Java plugin [65]. This works by fitting a spherical cap onto the interface, then calculating a tangent line using a user-defined baseline. Each contact angle was measured three times, with an error of less than one degree for all measurements.

Once the contact angles from each isothermal simulation are determined, a polynomial is fit to the data, as shown in Figure 21. Both quadratic and cubic fits are considered, which have the following forms, respectively:

$$CA(g_w, T = T_0) = A_0^q g_w^2 + B_0^q g_w + C_0^q, \quad (4.14)$$

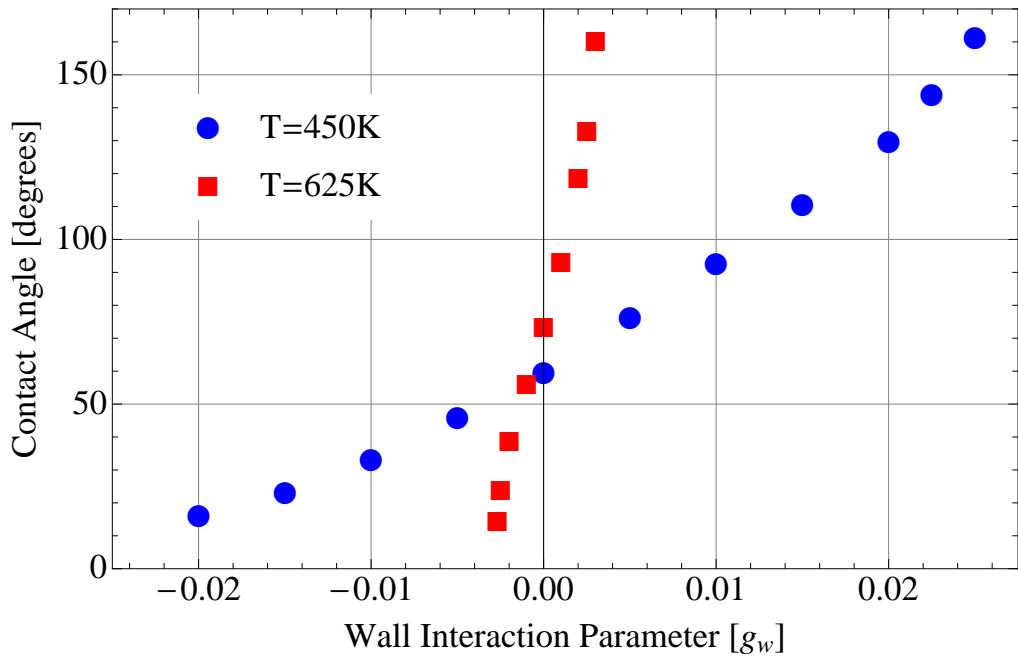


Figure 20: Contact angles vs. wall interaction parameters at $T = 450K$ (●) and $T = 625K$ (■).

and

$$CA(g_w, T = T_0) = A_0^c g_w^3 + B_0^c g_w^2 + C_0^c g_w + D_0^c. \quad (4.15)$$

Cubic polynomials will provide more accurate fits, but at the cost of having to solve a cubic equation. In the isothermal problem, this is a negligible calculation that is only performed at the beginning of the simulation. However, for a thermally varying simulation, this calculation increases the runtime as it must be performed at every wall node and each timestep, using the current local temperature. Thus, both fits are tested.

The coefficients obtained from these fits are shown in Tables 1 and 2. These coefficients are next fit over the temperatures in order to determine temperature dependent coefficients ($A^c(T)$, $B^c(T)$, etc.). It was found that the best fit for these coefficients was either a one term, two parameter, or two term, four parameter, exponential function of the form:

$$A^i(T) = a \exp(bT) + c \exp(dT). \quad (4.16)$$

These values are given for the quadratic and cubic fits in Tables 3 and 4.

Next, Equation (4.13) is combined with either Equation (4.14) or (4.15), depending on the curve fit that is being analyzed, to determine an expression for g_w . In the quadratic case, the equation takes the form:

$$\begin{aligned} & A^q(T)g_w^2 + B^q(T)g_w + \\ & [C^q(T) - (A_{exp}T^2 + B_{exp}T + C_{exp})] = 0. \end{aligned} \quad (4.17)$$

This can be solved simply for g_w using the quadratic equation. In the cubic case, the equation takes the form:

$$\begin{aligned} & A^c(T)g_w^3 + B^c(T)g_w^2 + C^c(T)g_w + \\ & [D^c(T) - (A_{exp}T^2 + B_{exp}T + C_{exp})] = 0, \end{aligned} \quad (4.18)$$

which is solved using a Newton-Raphson solver, with the solution to the quadratic case chosen as an initial guess.

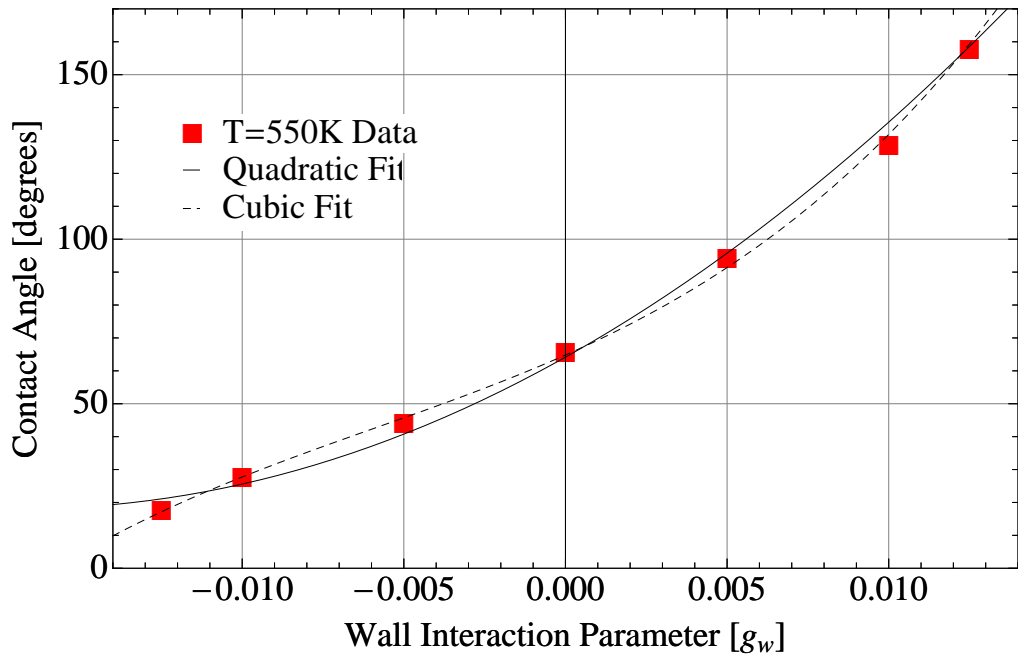


Figure 21: Quadratic (—) and cubic (---) polynomial fits for the determination of the contact angle as a function of the wall interaction parameter at $T = 550K$ (■).

Table 1: Coefficients for the quadratic fits of contact angles vs. wall interaction parameters at various temperatures.

T [K]	A_0^q	B_0^q	C_0^q
450	38448.50	2929.42	58.82
475	33240.55	3247.76	66.84
500	79144.31	3662.27	60.20
525	80432.58	4177.09	69.55
550	164318.01	5499.32	64.15
575	187427.46	6864.32	72.58
600	373294.88	11216.44	71.20
625	1329106.03	22663.58	72.48

Table 2: Coefficients for the cubic fits of contact angles vs. wall interaction parameters at various temperatures.

T [K]	A_0^c	B_0^c	C_0^c	D_0^c
450	272101.95	36045.81	2831.75	59.11
475	391284.56	29965.16	3138.26	67.21
500	1108160.53	75013.69	3370.32	60.58
525	1134372.59	77584.54	3958.11	69.71
550	8533136.73	149877.46	4351.62	64.80
575	18110748.85	149543.13	5709.52	73.46
600	115116056.25	291877.99	7643.66	71.81
625	1120542283.04	902421.90	15620.99	73.65

Table 3: The exponential function parameters determined for the quadratic coefficients.

Param.	$A^q(T)$	$B^q(T)$	$C^q(T)$
a	9.67E+02	3.14E+02	-9.20E-05
b	8.60E-03	4.91E-03	1.70E-01
c	7.94E-12	1.21E-08	2.53E+00
d	6.32E-02	4.46E-02	0.00E+00

Table 4: The exponential function parameters determined for the cubic coefficients.

Param.	$A^c(T)$	$B^c(T)$	$C^c(T)$	$D^c(T)$
a	3.03E-16	7.74E+02	3.28E+02	-6.11E-05
b	9.05E-02	8.90E-03	4.73E-03	1.41E-01
c	0.00E+00	4.20E-12	9.57E-13	9.50E+00
d	0.00E+00	6.34E-02	5.89E-02	0.00E+00

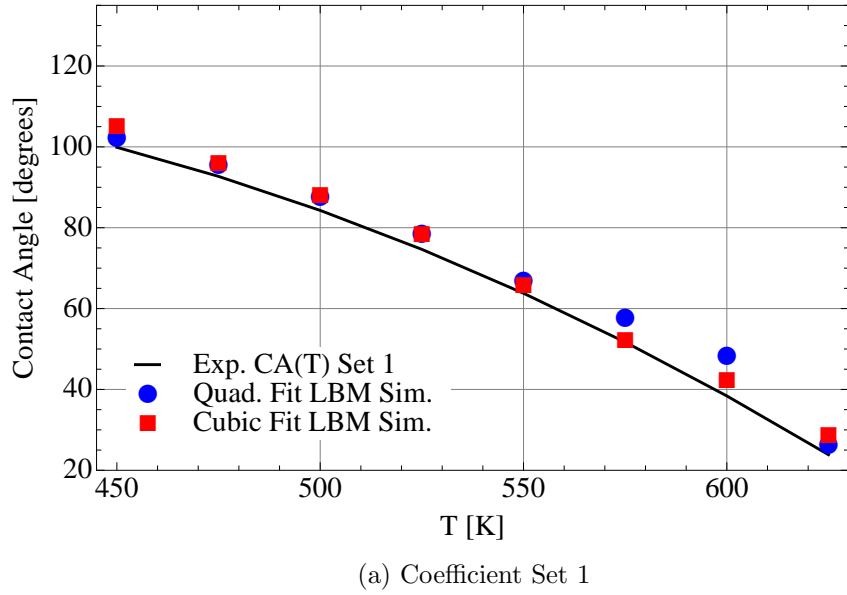
Table 5: Experimental coefficient sets.

Coefficient Set	A_{exp}	B_{exp}	C_{exp}
Set 1	-410	400	20
Set 2	-400	400	20
Set 3	-380	400	20
Set 4	-350	400	20

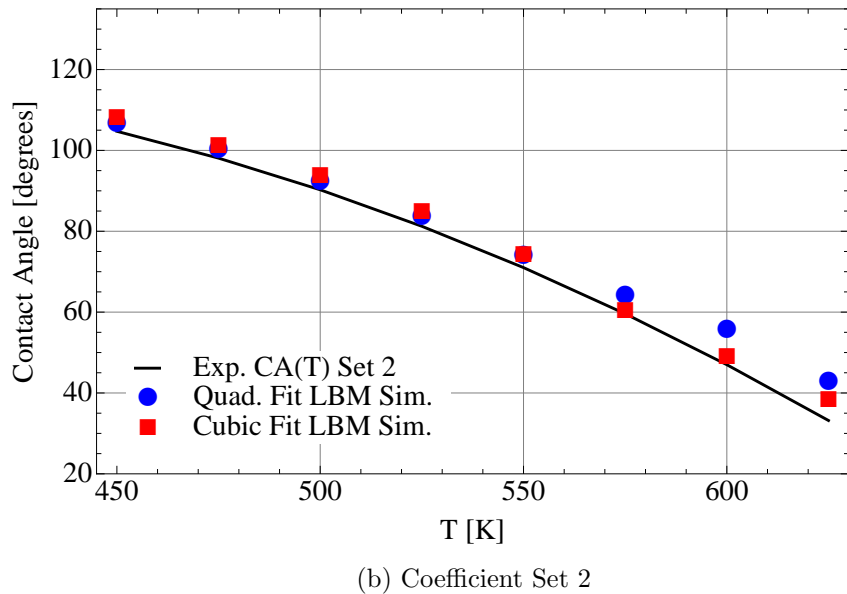
4.5.2 Wall Interaction Model Results

Simulations are performed for four instances of Equation (4.13), the coefficients of which are given in Table 5. This is done by utilizing either Equation (4.17) or Equation (4.18) for the determination of g_w , which is implemented into Equation (4.12) for the calculation of the interparticle force that results from interactions with the walls. Each time a function is fit to the data, an error is introduced in the calculation; however, these errors can be controlled by choosing appropriate fits at each step. The results from the sets of experimental function coefficients using this method are shown in Figures 22a - 22d. As can be seen, it is now possible to calculate the wall interaction parameter as part of the simulation, rather than specifying it *a priori*. This allows for simulating the temperature dependent variation of wetting characteristics, as determined by a general functional relationship between contact angle and temperature. The root mean square errors (RMSEs) for each set of simulation results, as compared to the experimental functional form used to calculate the wall interaction parameters, are specified in Table 6.

It was found that the accuracy of the quadratic fits of the coefficients improves as the contact angle increases. Higher contact angles correspond to larger (less negative) values of A_{exp} and lower temperature simulations. This relationship can be understood after reconsideration of Figures 20 and 21. The contact angle data fall in line with both the quadratic and the cubic fits with reasonable accuracy for larger contact angle values and lower tem-

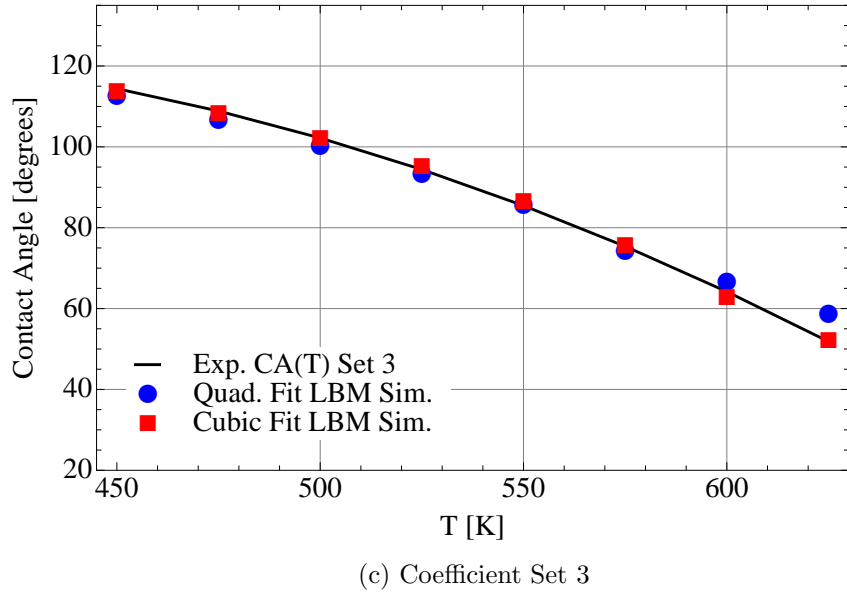


(a) Coefficient Set 1

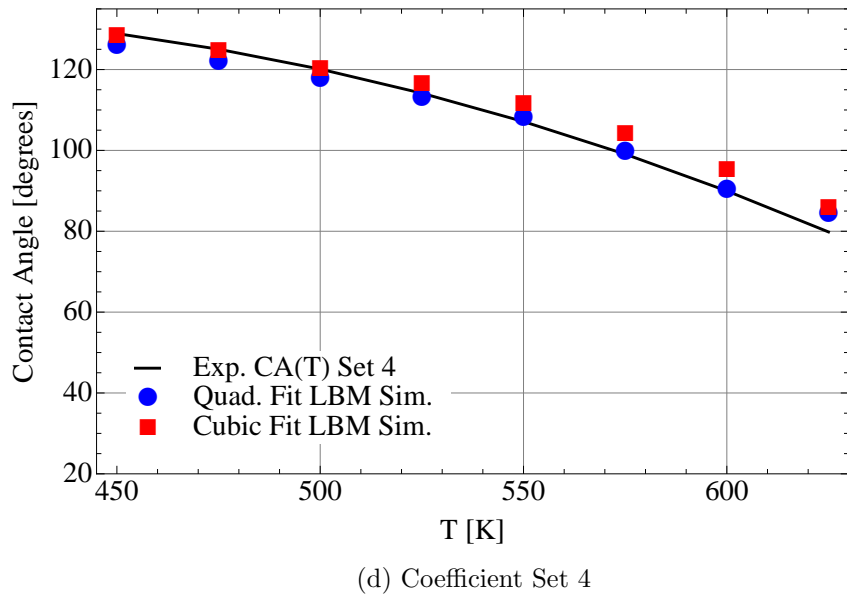


(b) Coefficient Set 2

Figure 22: LBM simulation results using wall interaction parameter quadratic (\bullet) and cubic (\blacksquare) curve fits based on the specified contact angle coefficient set (-). Continued on next page.



(c) Coefficient Set 3



(d) Coefficient Set 4

Figure 22: LBM simulation results using wall interaction parameter quadratic (\bullet) and cubic (\blacksquare) curve fits based on the specified contact angle coefficient set (—). Continued from previous page.

Table 6: Root mean square errors (RMSE) between the LBM simulation results and the experimental functions for each fit type.

Coefficient Set	Fit Type	RMSE
Set 1	Quadratic	4.83
Set 1	Cubic	3.73
Set 2	Quadratic	5.30
Set 2	Cubic	3.47
Set 3	Quadratic	2.84
Set 3	Cubic	0.76
Set 4	Quadratic	2.42
Set 4	Cubic	3.91

peratures. Conversely, at the lower contact angles which occur with experimental functions with smaller (more negative) values of A_{exp} , as well as at higher temperatures, the cubic fit becomes much more reliable. Therefore, it is likely worth the extra cost of solving the cubic equation in order to maintain accurate wetting behavior over a larger range of contact angles and temperatures. The quadratic form should be utilized only in the case where it is guaranteed that the contact angles will remain large and the temperatures will remain low.

It is important to emphasize that these results are based on the premise of fitting to a dataset. In this work, a general functional form for the data is utilized and a few variations of this expression are tested, but this remains a correlative method. Future work would greatly benefit from basing the wall interaction calculation specifically on the variation in surface energies that develop due to thermal fluctuations. This approach would be more rigorous and would provide a predictive, rather than correlative, methodology. However, there is still a large gap in the knowledge of the thermodynamics surrounding the wetting process, and many of the theories necessary for such an approach are still a matter of significant debate

[66–70]. Thus, the current model serves as a middle ground by which accurate data can be reliably retrieved in a thermal LBM simulation utilizing experimental correlations. This development marks a significant increase in the fidelity of thermal lattice Boltzmann models based on the pseudopotential wall interaction method.

4.6 MULTIPHASE, SINGLE-COMPONENT, THERMAL MODEL (MPSC-T) RESULTS: BUBBLE SIMULATIONS

The case of flow boiling in a microchannel is now examined. It is well known that wall interactions can have a large impact on the dynamics of multiphase flows. Thus, the previously developed wall interaction model is incorporated here. Results comparing different functional forms are shown at the end of this section, further justifying the importance of this model in thermal, multiphase flow simulations with wall interactions.

For comparison, a simple bubble simulation is first performed. This is necessary because bubble simulations are very sensitive to initial conditions (ICs) and boundary specifications. In fact, there is a distinct lack of thermal bubble simulations in the literature, and existing results either neglect the real thermodynamics of the system or consider only the bubble development in dynamic flows or simplified domains, without comparison to a stable, realistic base case [71–76]. This validity of such approaches is questionable as there is uncertainty about the origin of flow behaviors. Jain, et al., for instance, examined a static bubble under simplified, full periodic boundary conditions [33]. When periodic boundaries are used, a bubble simulation will quickly stabilize if initialized accurately. However, open inlet and outlet boundary conditions on a horizontal slit are much more difficult to resolve due to the inherent instability of bubbles in unbounded domains. A thermal bubble in a horizontal slit with open ends, first without any flow or heating influences, is modeled here. These simulations are then used as a base case against which the flow dynamics and heating effects can be observed. The density configuration of the initial conditions is shown in Figure 23. From these ICs, the progression of the bubble without any forced flow or heating influences

can be seen in Figures 24a-24d. For this particular initialization, the bubble is smaller than the critical stability radius, and therefore it quickly dissolves into the surrounding liquid.

The boiling case can be analyzed in comparison to this base case. The initial system matches the description given above, depicted in Figure 23, consisting of a single, small bubble in a horizontal slit with open ends. The only modification is the implementation of superheat (T_{sh}) to the liquid that fills the domain, such that $T_{liquid} = T_{vapor} + T_{sh}$. Figures 25a-25d present the density contours as the flow develops through time. This progression, as compared to Figures 24a-24d of the bubble without any heating effects, shows the expansion of the bubble, rather than its dissolution, due to phase change caused by the initial liquid superheat. This leads to the stable growth of the bubble in the channel. For verification of this effect, the evolution of the vapor mass fraction in the channel through time can be compared between the two cases, as shown in Figure 26. The phase change effect can clearly be seen in the second simulation with the liquid superheat.

Finally, a comparison of the wall interaction functions can be considered. Figures 27a - 27d show the density contours at 100,000 timesteps, during the flow development for four different contact angle functions. The functions correspond to Coefficient Set 1, Set 3 and Set 4, described in the previous section and given in Table 5, as well as a fourth set which has the same B_{exp} and C_{exp} coefficients, but uses $A_{exp} = -440$. The influence of the different contact angle models is clear and there is clearly a significant effect on the flow boiling dynamics.

This concludes the development of the single component, multiphase, thermal model. With these improvements, it is now possible to model complex wetting behavior, as well as simulate the dynamic phase change process. However, many systems contain more than a single chemical component. For instance, the boiling of water often takes place in the presence of air. In order to model this more complex behavior, a model capable of handling multiple components, in addition to the multiple phases and thermal variations shown here, is needed. The following chapter addresses this void.



Figure 23: The initial density contours of a vapor bubble (blue) surrounded by liquid (red).

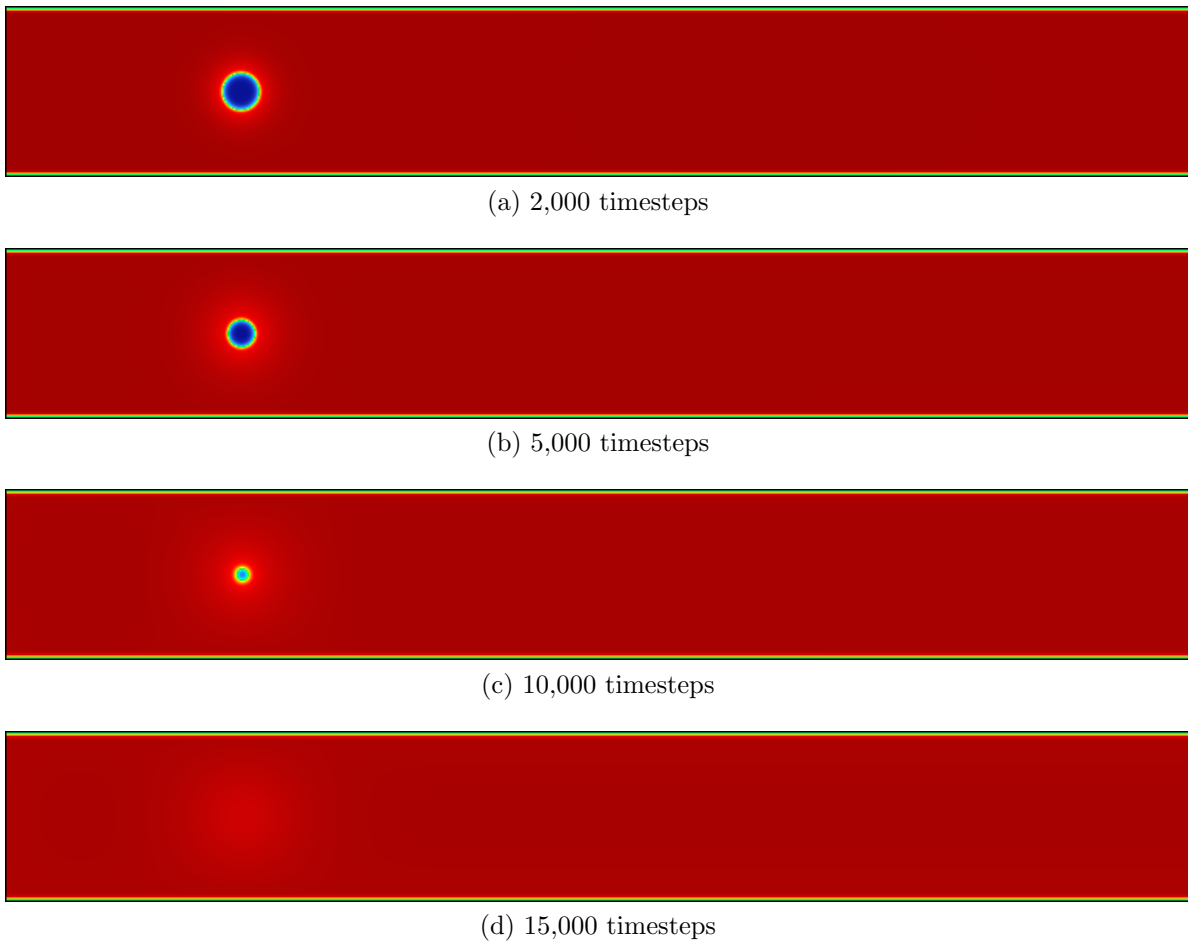


Figure 24: Density contours of bubble (blue) dissolution into the surrounding liquid (red) shown at various timesteps of the simulation.

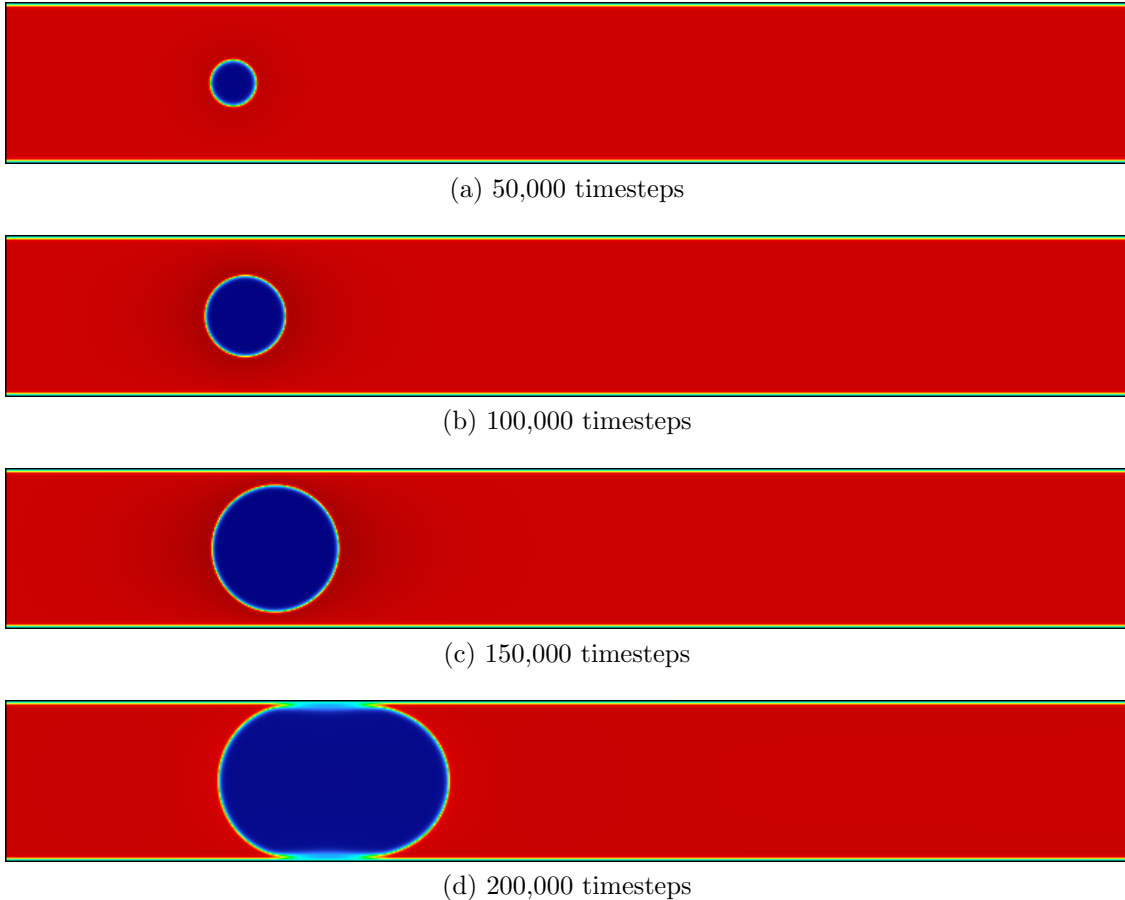


Figure 25: Density contours of the boiling process, showing the expansion of a vapor bubble (blue) due to an initial liquid (red) superheat at various timesteps of the simulation.

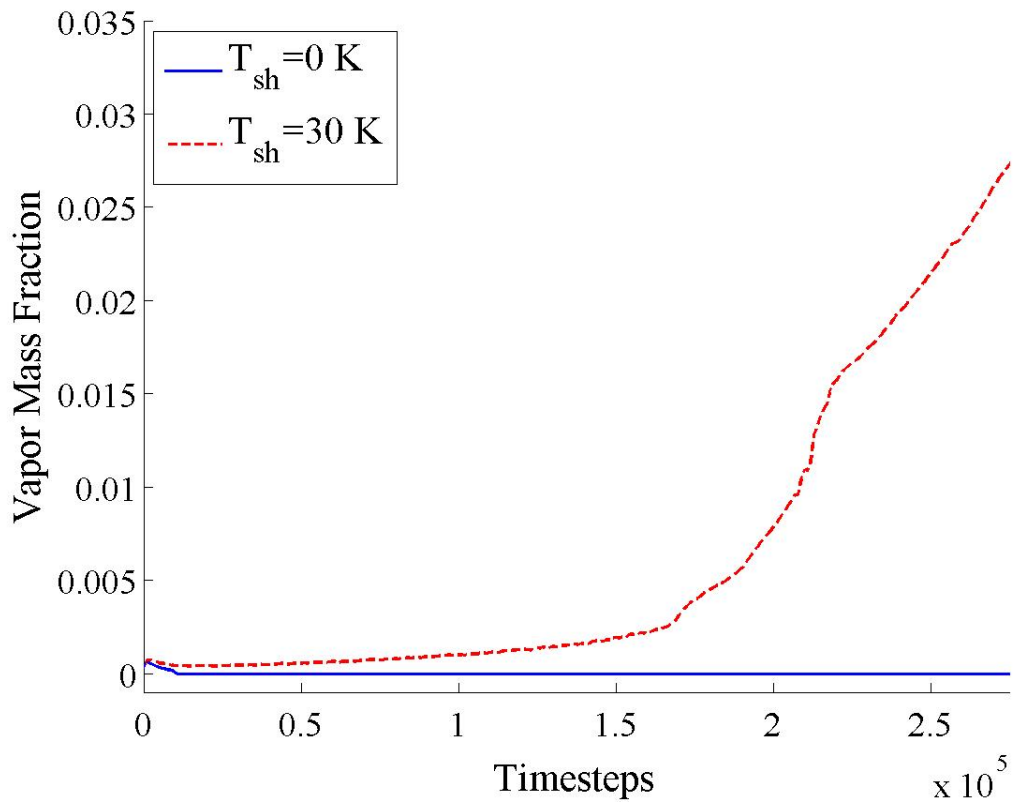


Figure 26: The time evolution of the vapor mass fraction during bubble dissolution (—) and boiling (---), depicting the phase change process that occurs due to an initial liquid superheat of T_{sh} .

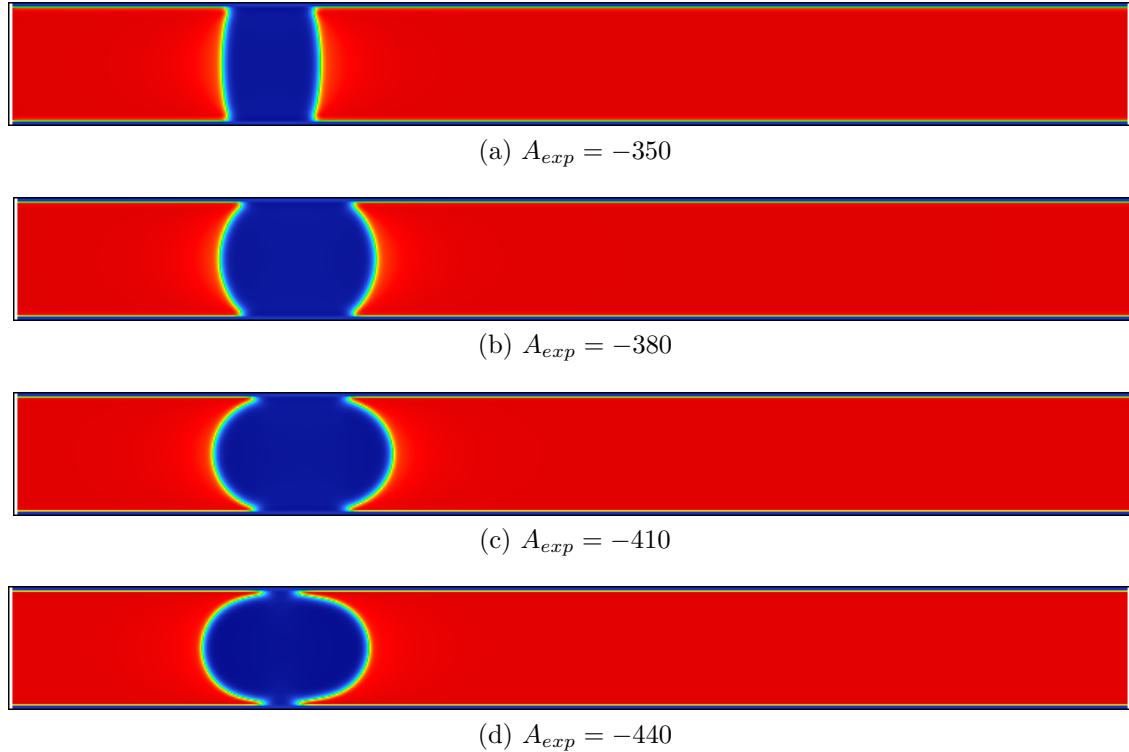


Figure 27: Density contours of various contact angle functional forms at 100,000 timesteps during a flow boiling simulation showing the effect on flow boiling dynamics of the wall wetting interaction model.

5.0 MULTICOMPONENT MODEL

5.1 INTERCOMPONENT INTERACTIONS

The existence of more than one chemical component adds a great deal of complication to a system's dynamics. However, the lattice Boltzmann method benefits from the ability to treat each component using a separate PDF. For instance, in a system of two components, Component A and Component B , one set of PDFs will represent Component A ($f_{\alpha,A}$) and another set will represent Component B ($f_{\alpha,B}$). Each set of PDFs can be evolved separately following the lattice Boltzmann equation, and its individual velocity moments will represent the density and velocity vector of its own component:

$$\rho_{A,LU} = \sum_{\alpha=1}^d f_{\alpha,A}, \quad (5.1)$$

$$\rho_{B,LU} = \sum_{\alpha=1}^d f_{\alpha,B}, \quad (5.2)$$

$$\rho_{A,LU} \mathbf{u}_{A,LU} = \sum_{\alpha=1}^d f_{\alpha,A} \boldsymbol{\xi}_\alpha, \quad (5.3)$$

$$\rho_{B,LU} \mathbf{u}_{B,LU} = \sum_{\alpha=1}^d f_{\alpha,B} \boldsymbol{\xi}_\alpha. \quad (5.4)$$

The subscript LU , which was introduced in Section 2.6, is used again to denote that the densities and velocity vectors are represented in the lattice domain. In the previous chapters, this was assumed to be the case and was therefore not explicitly expressed. However, in later sections, it is necessary to carefully distinguish between lattice values and physical values. Therefore, the subscript is now used when referring to densities, velocities, and temperatures

for consistency throughout the chapter. All other variables, such as the effective mass ψ , are assumed to still be in lattice units unless specifically stated otherwise.

The individual components are allowed to interact in a manner similar to the phase interactions developed in Chapter 3. In this case, interparticle pseudopotentials are utilized, which correspond to the attraction and repulsion of the different chemical components, instead of the phases [21]. The multiphase and multicomponent models have recently been combined by Bao and Schaefer, along with the implementation of advanced equations of state, to formulate a high-density ratio, multiphase, multicomponent model [18, 36, 77]. The intercomponent force acting on a particle of Component A due to a particle of Component B , takes the form:

$$F_{A,B} = c_0 \psi_A g_{A,B} \nabla \psi_B, \quad (5.5)$$

where $c_0 = 6$ for the $D2Q9$ and $D3Q19$ models, and $g_{A,B}$ is an interparticle interaction strength parameter that controls the interaction between the A and B chemical components. The domain for a two component simulation is configured by overlaying two numerical grids, one for each component. Each grid contains information about the PDFs, the density, the temperature, and the effective mass of its own component. As before, the particles within one grid are allowed to interact with themselves (intracomponent interaction) through the multiphase interactions already discussed. However, these particles can now also interact with the particles from the other grid (intercomponent interactions) through Equation (5.5). The grid corresponding to Component A will be influenced by $F_{A,B}$ via a velocity shift or the exact difference method. Similarly, the grid which contains information about Component B will be influenced by the intercomponent force $F_{B,A}$, taking the form:

$$F_{B,A} = c_0 \psi_B g_{B,A} \nabla \psi_B, \quad (5.6)$$

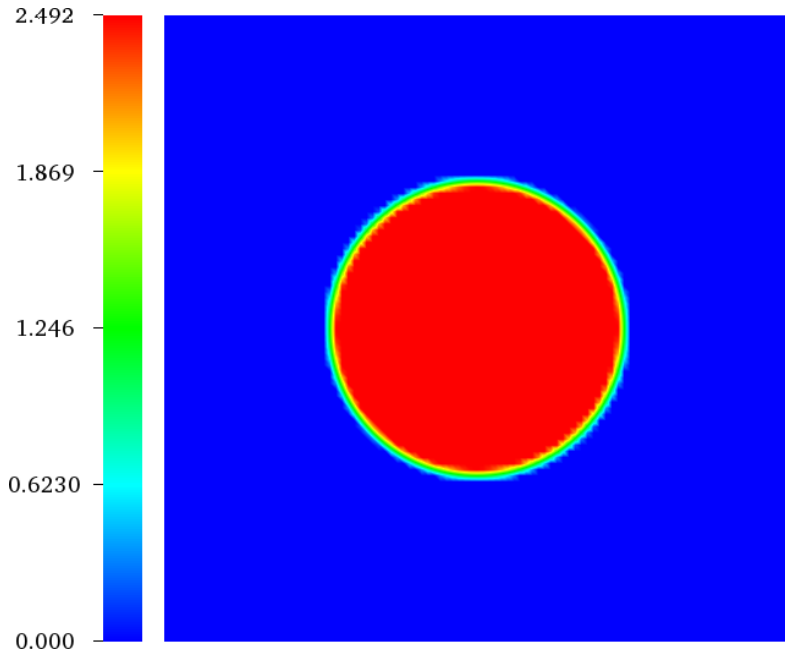
which is based on the intercomponent interparticle interaction strength $g_{B,A}$.

An example initialization of the two grids for a 2D simulation based on the two phase, two component model is illustrated in Figure 28. Grid one has a high-density, liquid region of Component A at its center and is surrounded by a zero-density region. On grid two, the nodes corresponding to the liquid region on grid one are initialized as a zero-density region and the nodes corresponding to the zero-density region on grid one are the low-density, vapor

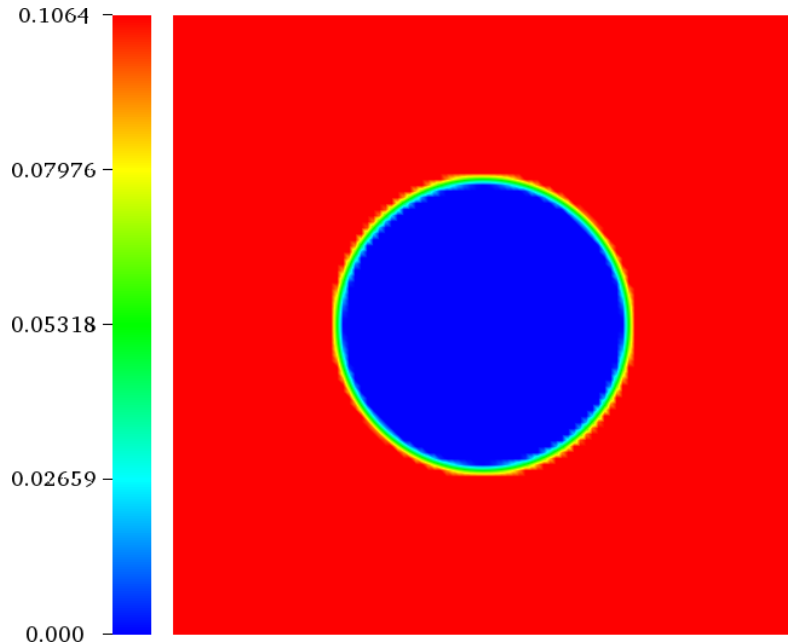
region of Component *B*. It is important to note that a zero-density region is not feasible in a numerical simulation. Implementation of such a region would lead to discontinuities in the gradient calculation and divergence of the simulation. Figure 28 shows the zero-density regions to have densities of exactly zero; however, this is just for clarity of explanation. In practice, it is necessary that in regions which are indicated as having zero-densities, small non-zero values are used. Thus, when the zero-density region is mentioned throughout this work, the region is, in actuality, a low density region. As will be discussed in the following sections, it is necessary to verify that this small value is actually small enough that the effect of this region is minimized to maintain an accurate simulation of immiscible substances.

5.2 MULTIPHASE, IMMISCIBLE, MULTICOMPONENT, ISOTHERMAL MODEL (MPIMC-IT) RESULTS: STATIC DROPLET

Utilizing the intercomponent interaction contributions of Equations (5.5) and (5.6) for the force calculations, two isothermal simulations are performed of a liquid water droplet surrounded by air in a fully periodic domain. The reduced density cross-sections at $T_p = 450$ K and $T_p = 600$ K are shown in Figures 29 and 30, respectively. The cross-sections are taken at the horizontal centerline ($y = 50$ LUs). The density ratio at $T_p = 450$ K is 152:1 and at $T_p = 600$ K is 13:1. The zero-density regions can also be seen in both of these figures as the lower density section of each line. Importantly, these zero-density regions have densities greater than zero, but less than the primary phase in that region. Specifically, the zero-density region of the water (Water_{zero}) lies below the vapor region of the air (Air_{vapor}) and the zero-density region of the air (Air_{zero}) lies below the liquid region of the water (Water_{liquid}). This requirement ensures that the behavior exhibited by the interphase and intercomponent interactions is dominated by the phases of interest, rather than the zero-density regions.



(a) Grid one: Liquid droplet of Component *A* (red) surrounded by a zero-density region (blue).



(b) Grid two: Vapor region of Component *B* (red) surrounding a zero-density region (blue).

Figure 28: The two numerical grids for each chemical component showing the reduced density contours of a typical 2D, two phase, two component droplet simulation.

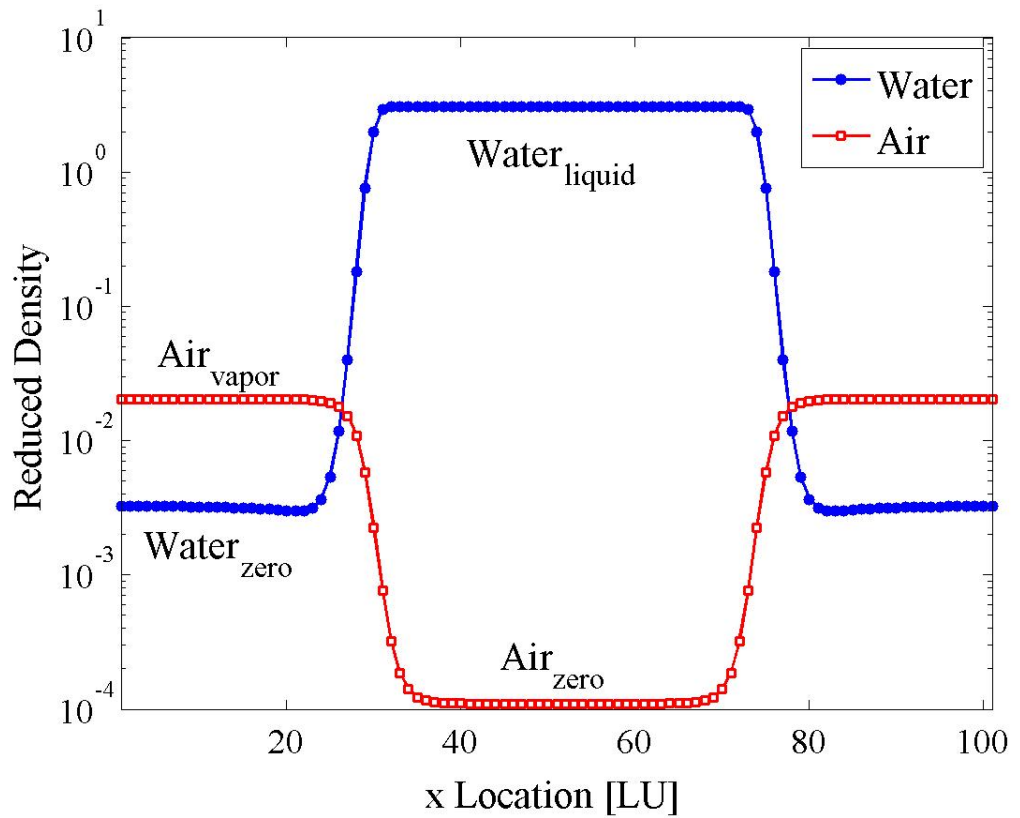


Figure 29: Reduced density cross-sections of a liquid water droplet in air at 450 K. The density ratio is 152:1.

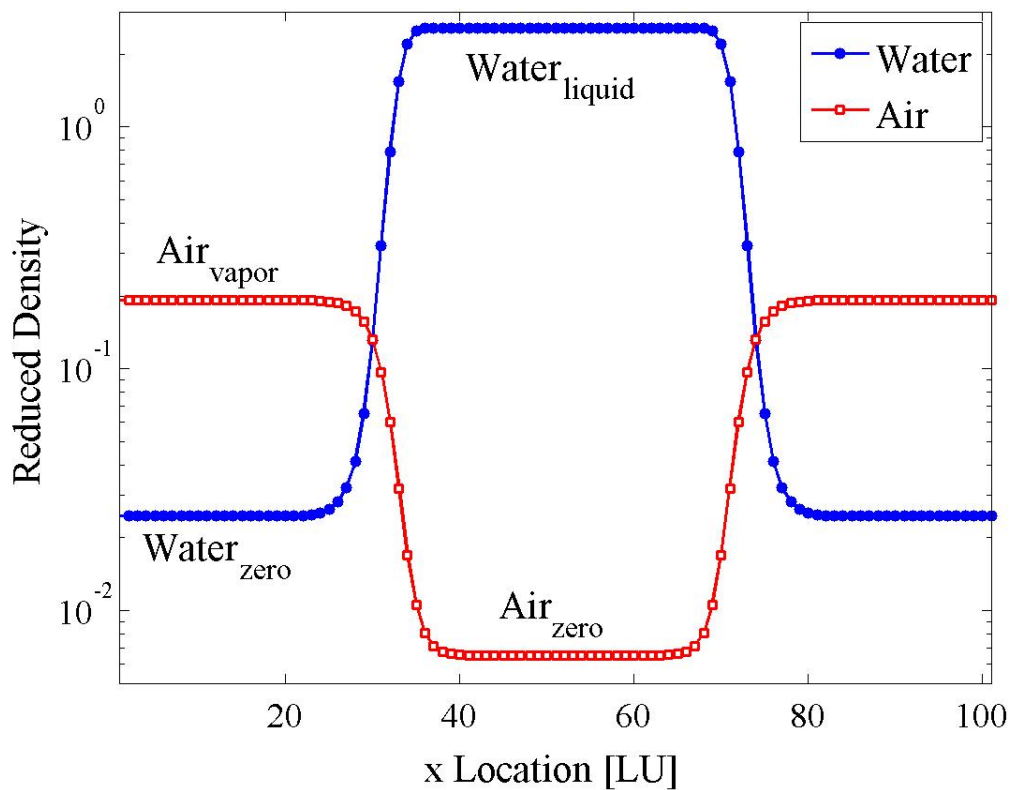


Figure 30: Reduced density cross-sections of a liquid water droplet in air at 600 K. The density ratio is 13:1.

5.3 INCORPORATION OF A THERMAL MODEL

While Bao and Schaefer have greatly improved the multiphase, multicomponent LBM [36, 77], thermal effects have not yet been incorporated into these models. This is an important aspect, as many of the engineering systems of interest have significant temperature variations. However, just as the admittance of thermal variations led to an obstacle with the wall interaction force parameter, adding a passive-scalar model to the multicomponent framework leads to complications with the intercomponent interparticle interaction parameters and contradictions with regards to the macroscopic variables.

5.3.1 Stability Analysis of Interaction Parameters

One particular issue concerns the stability of the simulation at different values of intercomponent interaction strength parameters ($g_{A,B}$ in Equation (5.5) and $g_{B,A}$ in Equation (5.6)). Thus far, nothing was said concerning the magnitude or determination of these parameters. Before delving into the thermal model, it is necessary to better understand the effects that the variation of these parameters have on the model's stability. To that end, a stability region analysis is undertaken to examine the interparticle interaction parameter ranges which lead to stable simulations. In this study, the $g_{A,B}$ and $g_{B,A}$ parameters are varied over a wide range. This range was chosen such that the stability domain is bounded over the set of temperatures considered. It is found that there are three possible outcomes: 1) convergence to a stable and valid density ratio, 2) complete divergence of the simulation, or 3) convergence to a stable, but erroneous density ratio. An erroneous density ratio here is defined as one in which the density of the vapor phase component is less than that of the zero-density region of the liquid phase component. An example of such a system is shown by the reduced density cross-sections depicted in Figure 31. As discussed previously, it is not possible to use a true zero-density region and consequently, the zero-density regions actually correspond to small, non-zero values. However, for certain values of $g_{A,B}$ and $g_{B,A}$, this causes problems. When the vapor phase of Component B (Air_{vapor} in the case of Figure 31) has a density smaller than that of the zero-density region of Component A (Water_{zero} in Figure 31), the

interaction between the liquid phase of Component A and the zero-density region of Component A ($\text{Water}_{\text{liquid}}$ and $\text{Water}_{\text{zero}}$) is greater than the interaction between the liquid phase of Component A and the vapor phase of Component B ($\text{Water}_{\text{liquid}}$ and $\text{Air}_{\text{vapor}}$). While this may be valid for a miscible, multicomponent mixture, if immiscible dynamics are intended, such a simulation will yield inaccurate behavior. In this work, immiscibility is desired, for reasons which will be discussed in the following section, and therefore the parameters which lead to this state are indicated separately in this analysis and are not considered to be part of the valid stability region.

The stability analysis is performed for a variety of temperatures to determine the stability region for each temperature. These results are shown in Figures 32a-32e for temperatures from 450 K to 625 K. Clearly, the region of stability shifts as the temperature changes. This highlights the importance of this study. If only a single temperature is used to find stable parameters, it is possible that in a thermal simulation, temperature changes could lead to unstable simulations. Therefore, from this information, the overlap in the stability regions is analyzed by selecting only interaction pairs that are stable across all of the temperatures considered. In this manner, a set of parameters can be found that will, in a thermal study, continue to yield stable and valid density ratios as the temperature of the simulation varies. Figure 33 displays the region of overlap between all of these simulations and it can be seen that values of $g_{A,B}=0.05$ and $g_{B,A}=0.005$ will maintain stability over thermal variations spanning from 450 K to 625 K at a minimum.

5.3.2 Reconstruction of Macroscopic Variables

With the interaction parameters well-defined, a treatment of the thermal phenomena in the MPMC model can now be evaluated. For a binary fluid with thermal effects and multiple phases, four equations must be considered: a hydrodynamic evolution equation and a thermal evolution equation for each component. However, as shown in Equations (5.3) and (5.4), there are separate velocities for each component despite the fact that these occur on overlapping nodes of the two numerical grids (i.e. at the same spatial location). Similarly, the same will occur for the temperatures, with the corresponding nodes on the two grids

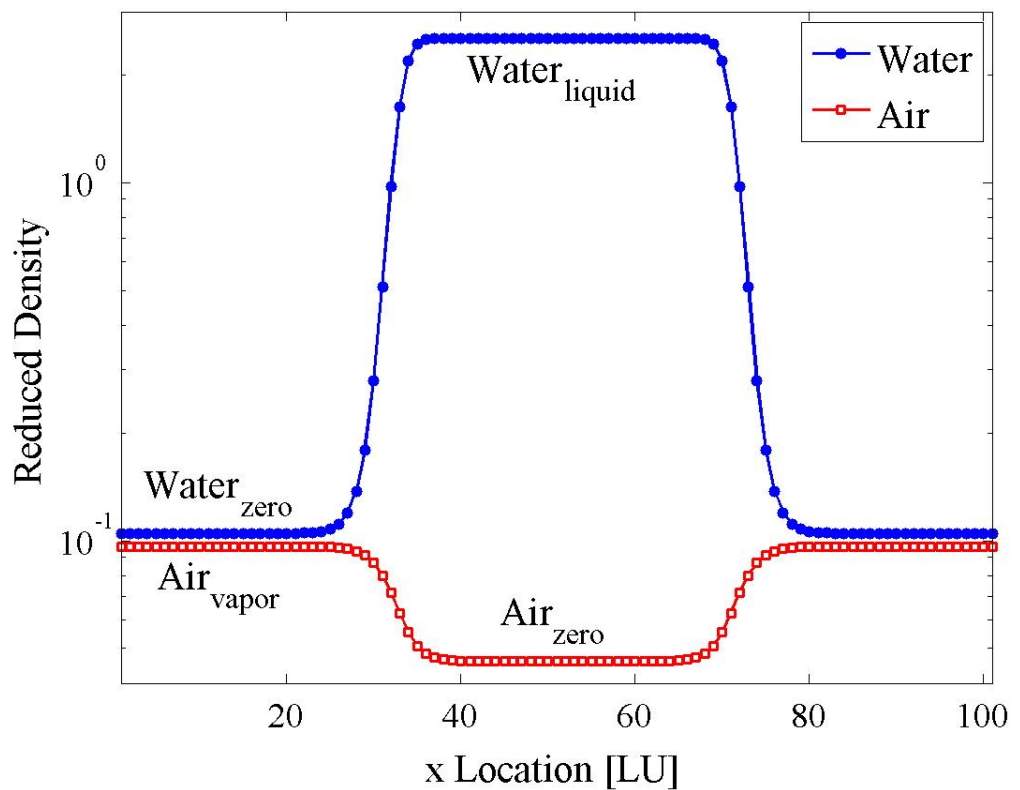
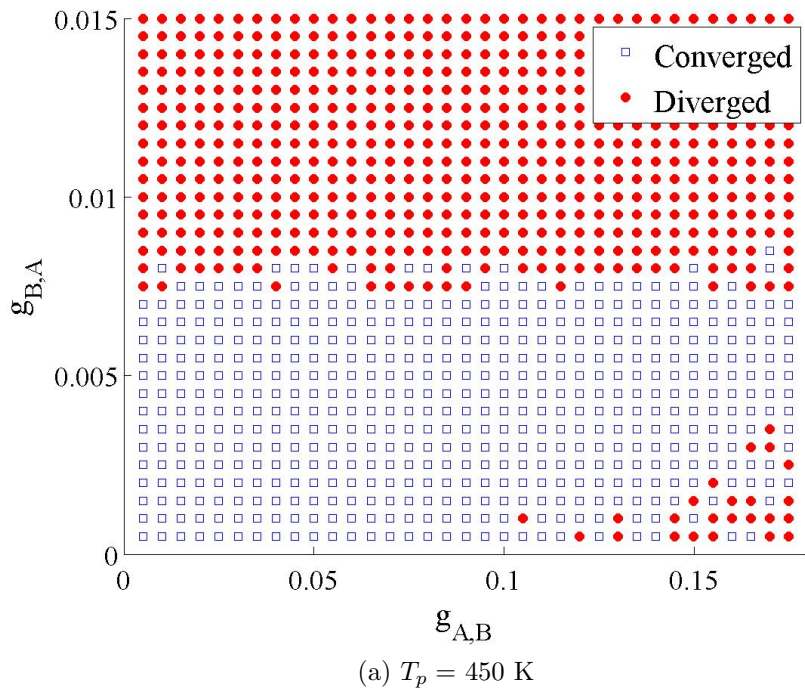
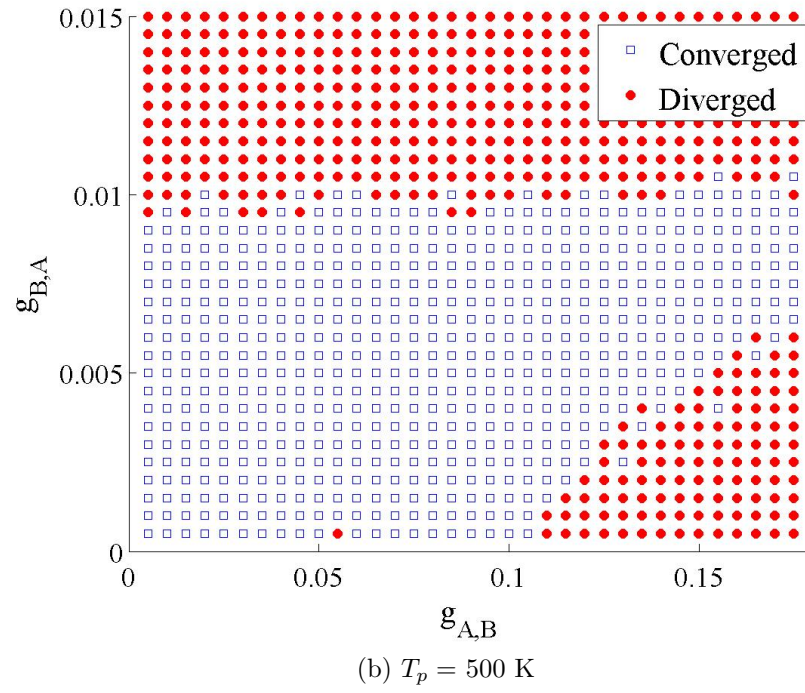


Figure 31: Reduced density cross-sections showing a ratio error where the zero-density region of the water is larger than the vapor phase region of the air.



(a) $T_p = 450$ K



(b) $T_p = 500$ K

Figure 32: Stability region analysis of intercomponent interaction parameters at the specified temperatures (continued on next page).

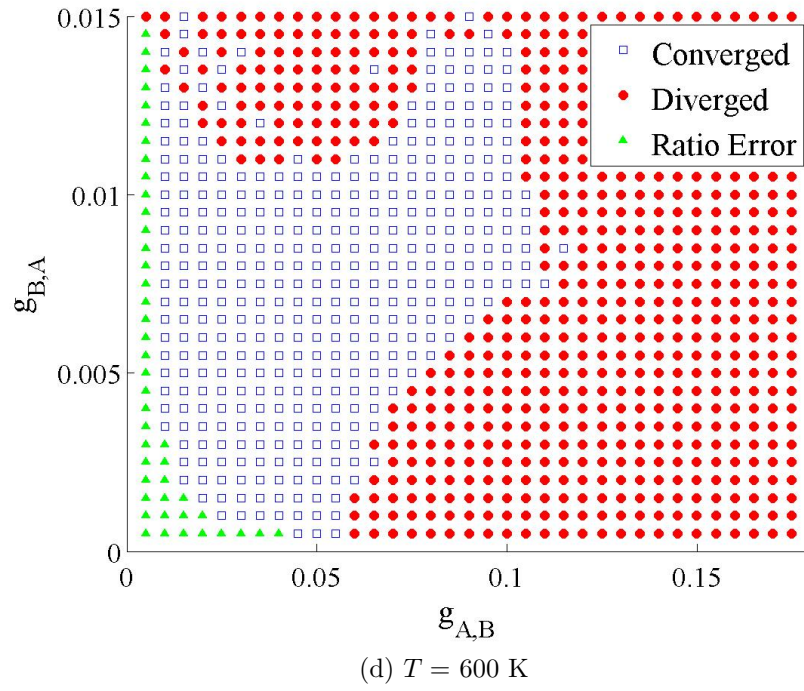
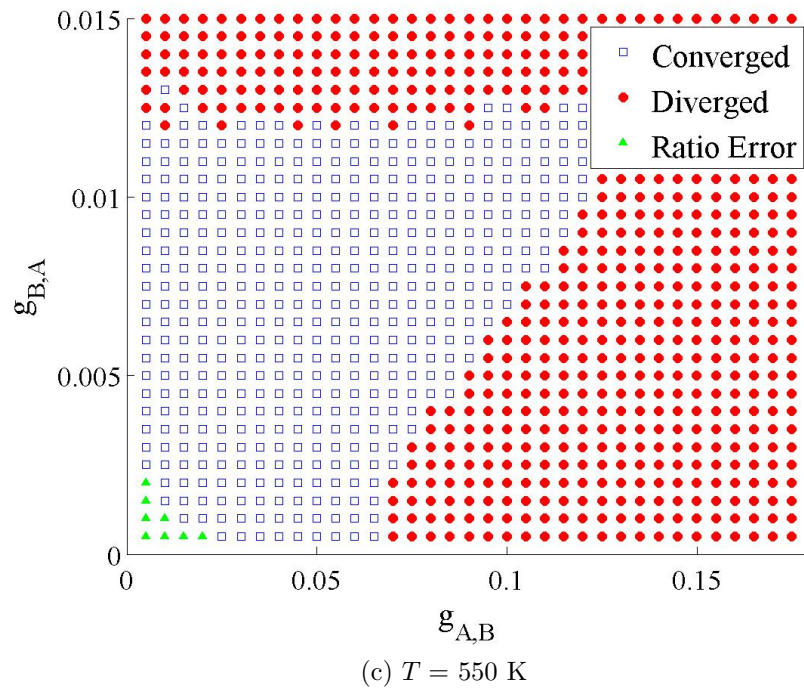


Figure 32: Stability region analysis of intercomponent interaction parameters at the specified temperatures (continued from previous page and continued on next page).

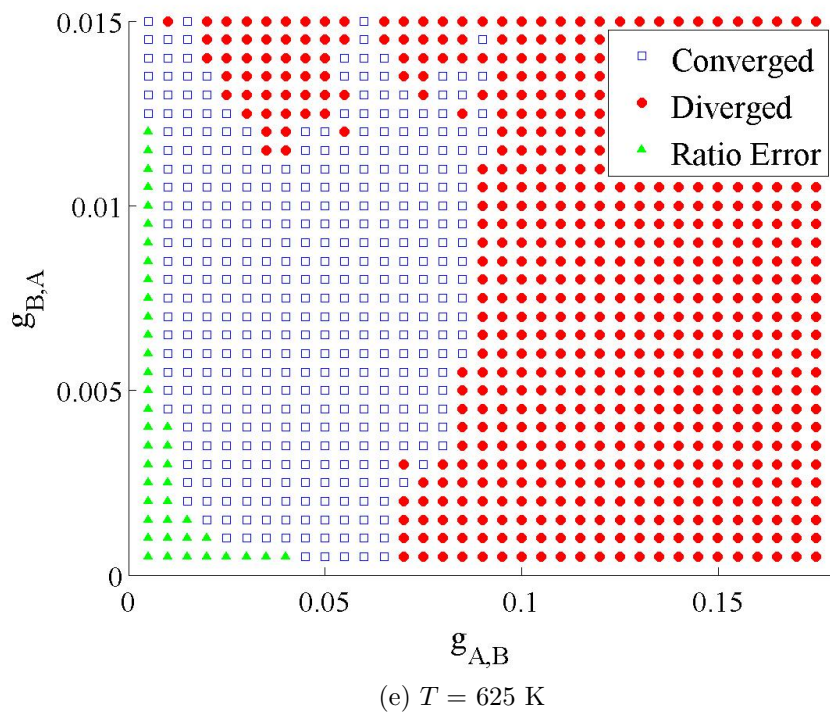


Figure 32: Stability region analysis of intercomponent interaction parameters at the specified temperatures (continued from previous page).

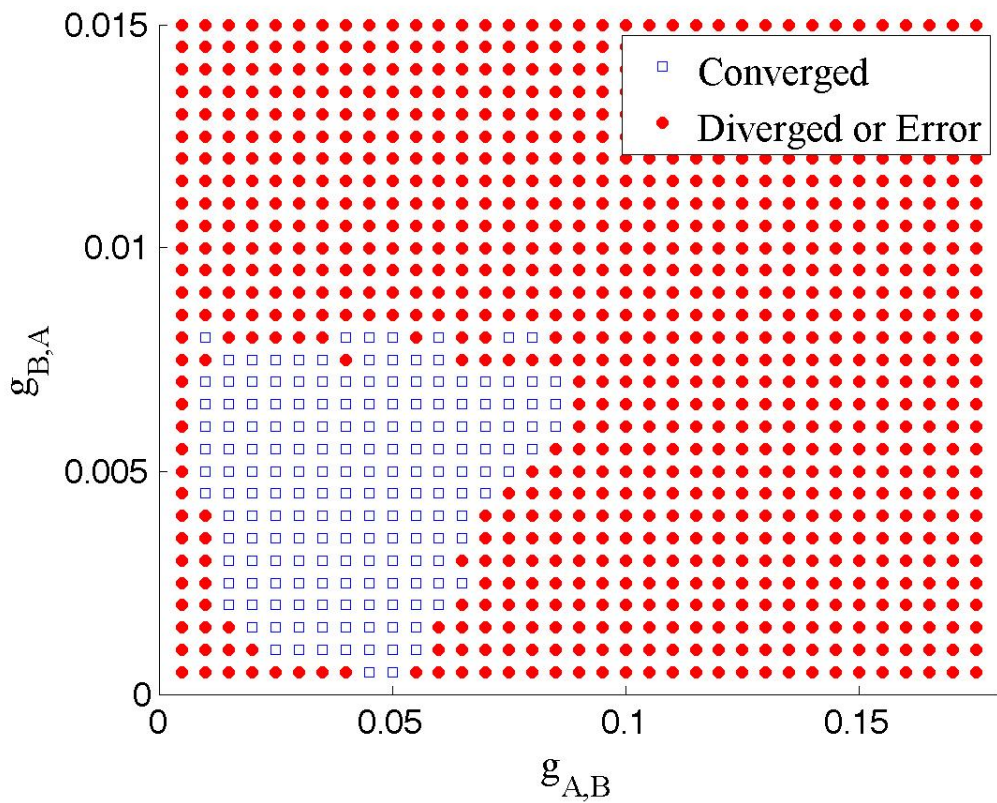


Figure 33: Overlap of the stable regions of the intercomponent interaction parameters from 450 K to 625 K.

having potentially different temperature values. Clearly, this is not physically consistent as the same point in space must have only a single velocity vector and a single temperature. Therefore, the primary difficulty lies in the reconstruction of the macroscopic velocity and temperature information from multiple equations.

First, independent thermal PDFs are solved, one for each chemical component. The coupling of the temperatures is carried out post-streaming using a density-weighted combination of the physical temperatures, such that $T_{coupled,p}$ is defined as:

$$T_{coupled,p} = \frac{\sum_{i=1}^N \rho_{i,p} T_{i,p}}{\sum_{i=1}^N \rho_{i,p}}, \quad (5.7)$$

where the subscript p denotes the physical domain, i runs from 1 to N components, and the temperatures are found from independently treated PDFs, just as the densities were in the isothermal model described above. In the two component case where $i = 1$ corresponds to Component A , and $i = 2$ corresponds to Component B , Equation (5.7) becomes:

$$T_{coupled,p} = \frac{\rho_{A,p} T_{A,p} + \rho_{B,p} T_{B,p}}{\rho_{A,p} + \rho_{B,p}}, \quad (5.8)$$

where the physical values are found by first calculating the macroscopic variables in the lattice domain using Equations (5.1), (5.2), and:

$$T_{A,LU} = \sum_{\alpha=1}^d g_{\alpha,A}, \quad (5.9)$$

$$T_{B,LU} = \sum_{\alpha=1}^d g_{\alpha,B}, \quad (5.10)$$

which, along with the densities, can be translated to the physical domain using the concept of reduced properties discussed in Section 2.6:

$$\rho_{A,p} = \rho_{A,LU} \frac{\rho_{c,p}}{\rho_{c,LU}}, \quad (5.11)$$

$$\rho_{B,p} = \rho_{B,LU} \frac{\rho_{c,p}}{\rho_{c,LU}}, \quad (5.12)$$

$$T_{A,p} = T_{A,LU} \frac{T_{c,p}}{T_{c,LU}}, \quad (5.13)$$

$$T_{B,p} = T_{B,LU} \frac{T_{c,p}}{T_{c,LU}}. \quad (5.14)$$

It is important in the case of temperatures to use values in the physical domain for the coupling carried out in Equations (5.7) and (5.8), as it is the physical temperatures, not the lattice temperatures, which must be equal for thermodynamic consistency. The reason for this is clear when it is recalled that the critical temperatures in the lattice domain are constant across different chemical components. Thus, two different components, both with the same physical temperature but different physical critical temperatures, will actually have two different lattice temperatures. The temperature can be converted back into lattice units post-coupling to form two different coupled temperatures, one for each component, but representing the same physical value:

$$T_{A,coupled,LU} = T_{coupled,p} \frac{T_{c,LU}}{T_{c,p}}, \quad (5.15)$$

$$T_{B,coupled,LU} = T_{coupled,p} \frac{T_{c,LU}}{T_{c,p}}. \quad (5.16)$$

These values are then used to evaluate the effective masses of each of the components, which can be used for the determination of interparticle and intercomponent potentials.

The velocity information obtained from the two hydrodynamic equations must also be combined. The method used to select the velocities must be done in such a way that consistency is maintained and momentum is conserved globally. The coupled velocity is therefore also calculated via weighting by the densities at each node:

$$\mathbf{u}_{coupled,LU} = \frac{\sum_{i=1}^N \rho_{i,LU} \mathbf{u}_{i,LU}}{\sum_{i=1}^N \rho_{i,LU}}. \quad (5.17)$$

As noted by the subscripts, this coupling can be carried out in the lattice domain. The single velocity vector and the two coupled temperatures (all in lattice units), are then utilized in the calculation of the thermal equilibrium PDFs:

$$g_{\alpha,A}^{(0)} = w_\alpha T_{A,coupled,LU} \left[1 + \boldsymbol{\xi}_\alpha \cdot \mathbf{u}_{coupled,LU} + \frac{1}{2} (\boldsymbol{\xi}_\alpha \cdot \mathbf{u}_{coupled,LU})^2 - \frac{1}{2} u_{coupled,LU}^2 \right], \quad (5.18)$$

$$g_{\alpha,B}^{(0)} = w_\alpha T_{B,coupled,LU} \left[1 + \boldsymbol{\xi}_\alpha \cdot \mathbf{u}_{coupled,LU} + \frac{1}{2} (\boldsymbol{\xi}_\alpha \cdot \mathbf{u}_{coupled,LU})^2 - \frac{1}{2} u_{coupled,LU}^2 \right]. \quad (5.19)$$

These equilibrium PDFs are subsequently used in the collision steps of the separate thermal evolution equations for the corresponding components. This approach is consistent due

to the fact that both components occupying the same spatial area should be equilibrating toward the same thermal equilibrium in the physical domain.

By enforcing the immiscibility of the components through proper interparticle interaction parameters, as discussed in the previous section, this approach should maintain the same conservation properties as the single-component model. An error will exist due to the inability to simulate true zero-density regions in the numerical scheme, but this can be minimized by maintaining a sufficiently large ratio between the phases of interest and the zero-density regions (i.e. ensuring the interaction parameters do not approach regions of density errors, as described in the stability analysis of the previous section). The thermal model is analyzed in the following section by considering the following cases: a static thermal conduction simulation, a static liquid droplet simulation, and a thermocapillary migration study.

5.4 MULTIPHASE, IMMISCIBLE, MULTICOMPONENT THERMAL MODEL (MPIMC-T) RESULTS

5.4.1 Static Thermal Conduction

The numerical scheme must first be tested to ensure that it is capable of reproducing realistic thermal behavior in a simple, static system. In order to evaluate this concept, a thermal conduction simulation is performed. A 2D channel, 50 LU x 50 LU, periodic in the x -direction is considered. The two component thermal model is utilized, but both components are initialized as liquid water at 550 K to avoid any complications from differing chemical properties. As shown in Figure 34, the domain is initialized with two horizontal liquid layers of water. The top and bottom walls are fixed at 545 K and 555 K, respectively, as shown by the initial reduced temperature vertical cross-section (taken at $x = 25$ LU) and the reduced temperature contours in Figure 35. Only one of the grids is shown here despite the fact that both grids are evolved in time. This is because both grids contain water; thus, the physical critical properties are the same. As a result, the reduced temperatures, in addition to the physical temperatures, are equal at all times after the thermal coupling procedure is

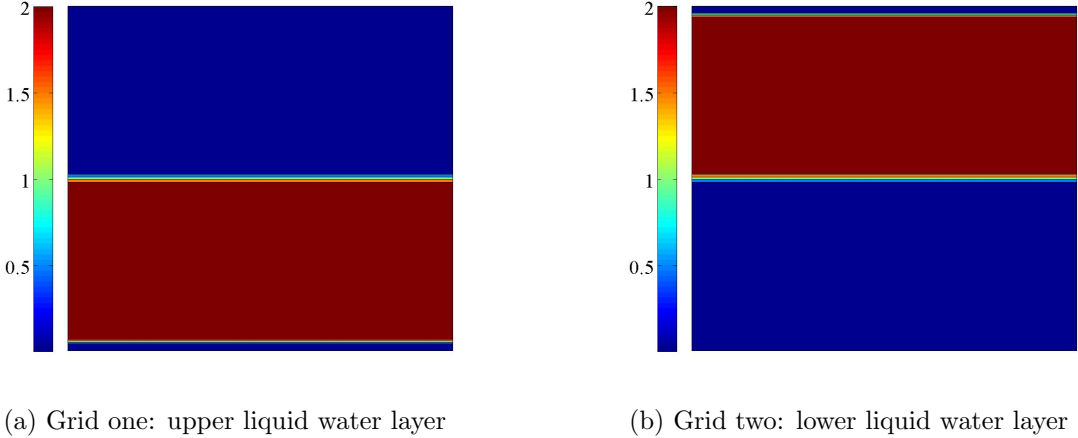


Figure 34: Initial reduced density contours showing the two liquid layers (red) and zero-density regions (blue) on the two grids of the 2D, two component, thermal conduction simulation.

carried out. The physical temperature contours would still be equal had different chemical components been used, but the reduced and lattice temperatures would not be equal in that case.

The simulation is evolved through time, as depicted by the reduced temperature vertical cross-sections of grid one (taken at $x = 25$ LU) in Figure 36, until reaching a steady state. The colorbar in the figure represents the timesteps, with darker lines corresponding to later times. The final reduced density vertical cross-sections of the simulation are shown in Figure 37a. The separate liquid components are shown with the existence of the diffuse interface at the intersection of the two components. Reduced temperature contours are also depicted in 37b. The final state is seen to be the correct linear conduction profile that is expected in a static system, verifying that the thermal model is functioning correctly, despite the presence of two distinct phases. Figure 38 shows the residual temperature error between the simulation results and the theoretical value, calculated as:

$$\text{TError} = \frac{\sum_{i=1}^N |T_{LBM,i} - T_{theor,i}|}{N}, \quad (5.20)$$

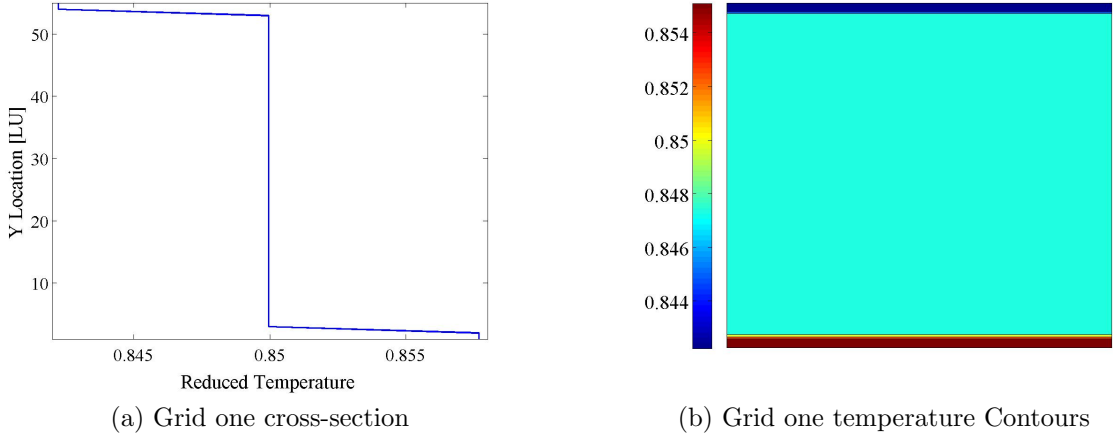


Figure 35: Initial reduced temperature cross-section (taken at $x = 50$ LU) and reduced temperature contours of the 2D, two component, thermal conduction simulation.

where the index represents the nodes along the vertical cross-section. It can be seen that the simulation is rapidly equilibrating to the theoretical linear conduction profile, with the thermal profile reaching a residual of 10^{-4} within 9,000 timesteps. Comparing Figures 36 and 37a, the linearity of the profile is maintained through the diffuse interface where the two components intersect as well.

The importance of the coupling models can now be examined by comparing the error between the temperatures and velocities of the two grids. For any given node, the physical temperature and the velocities must be equivalent. When both the velocities and temperatures are coupled, the errors between the grids will be zero as the values of both grids are set to the coupled values. However, it is possible to relax the coupling constraint on the temperatures, the velocities, or both, and examine the error that arises by comparing, at each time step, the values of the two different grids. The temperature error is calculated in the physical domain as:

$$T_{error,p} = \sum_{\text{all nodes}} \frac{|T_{\text{Grid one},p} - T_{\text{Grid two},p}|}{\# \text{ of nodes}}, \quad (5.21)$$

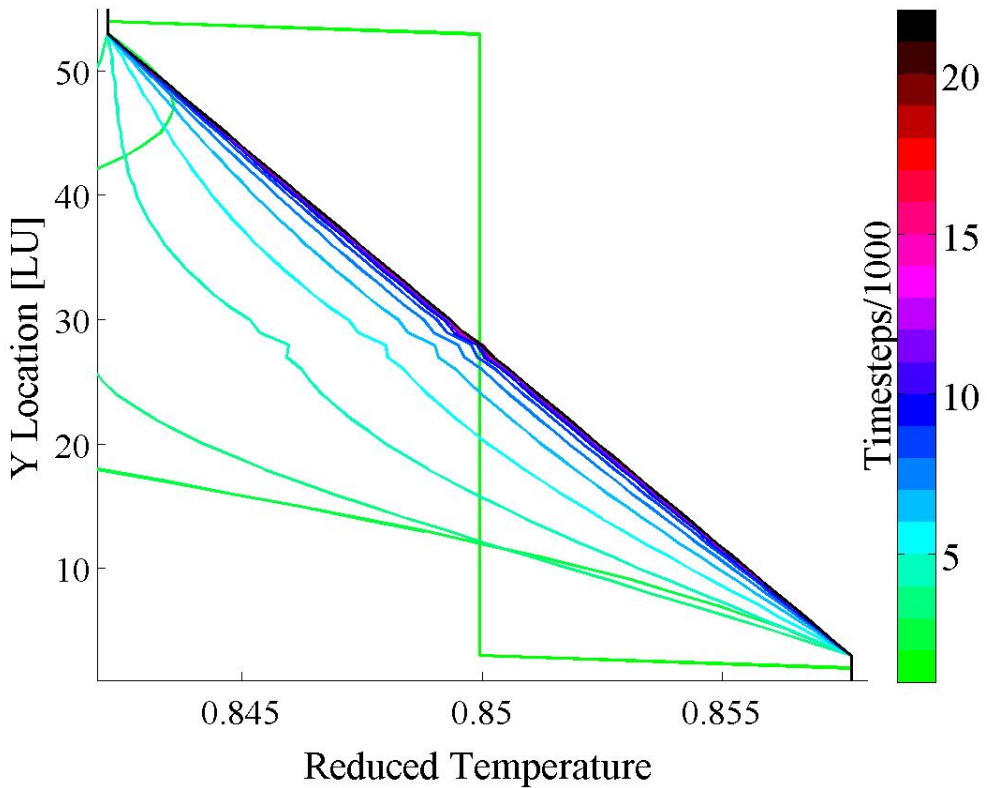


Figure 36: Reduced temperature cross-sections of grid one (taken at $x = 25$ LU) showing the time evolution of the thermal profile of the 2D, two component, thermal conduction simulation. Each line represents a single timestep, with darker colors corresponding to increasing times.

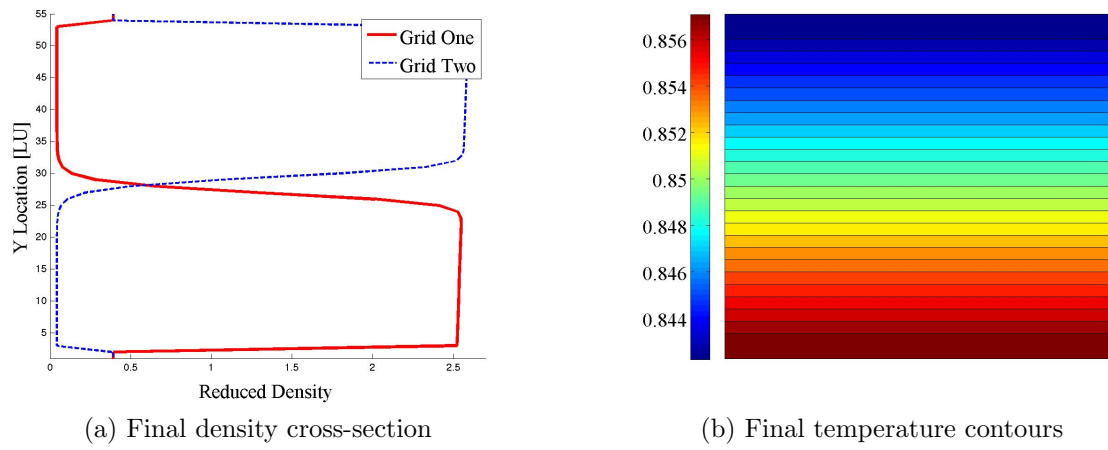


Figure 37: Final reduced density cross-sections and reduced temperature contours of grid one of the 2D, two component, thermal conduction simulation.

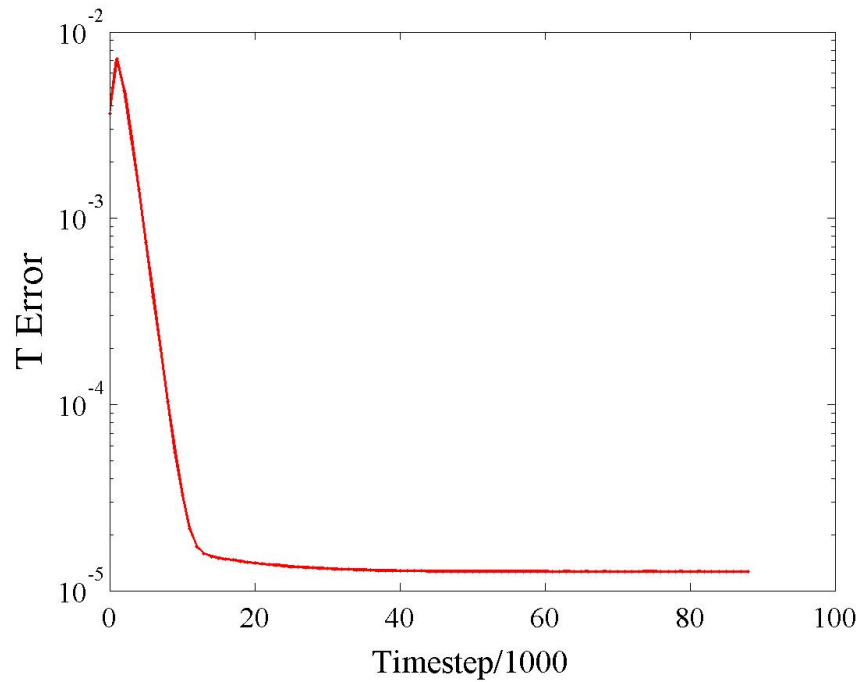


Figure 38: Residual temperature error between the simulation results and the theoretical solution as the 2D, two component thermal conduction simulation evolves through time.

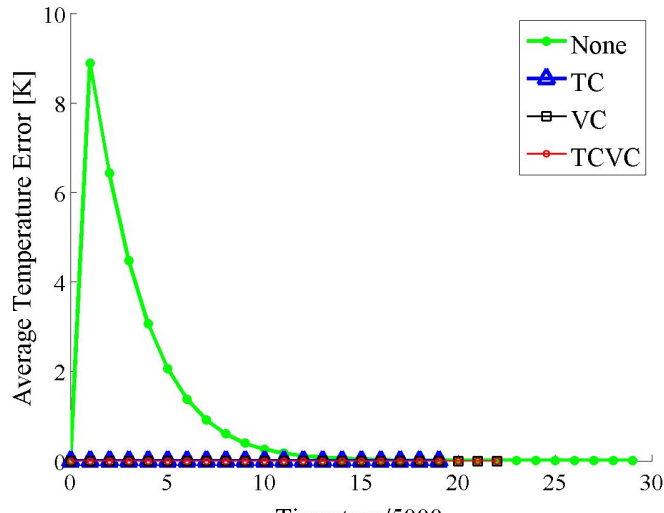
and the errors in the magnitudes of the velocities are calculated for the 2D case in lattice units as:

$$|V|_{error} = \sum_{\text{all nodes}} \frac{\sqrt{(u_{x,\text{Grid one}} - u_{x,\text{Grid two}})^2 + (u_{y,\text{Grid one}} - u_{y,\text{Grid two}})^2}}{\#\text{ of nodes}}. \quad (5.22)$$

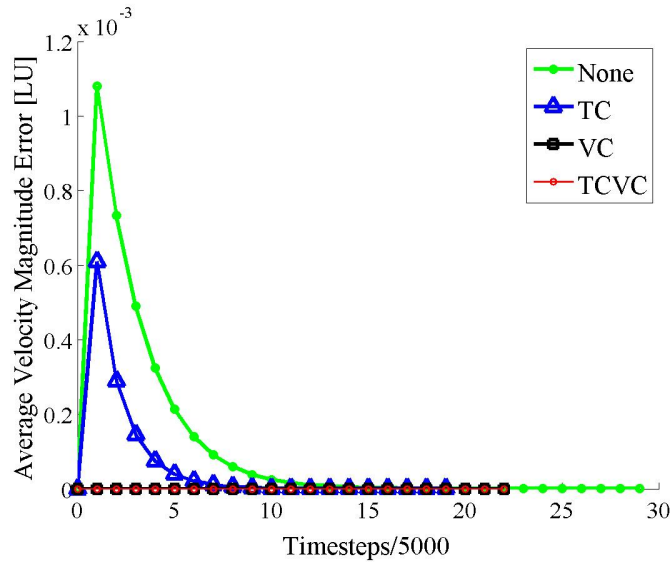
These errors are plotted in Figure 39 for the thermal model for the four cases of no coupling of any kind, only temperature coupling, only velocity coupling, and both velocity and temperature coupling. By definition, the temperature-coupled model will have no temperature error, the velocity-coupled model will have no velocity error, and the combined model will have no error at all. It can be seen that the final solution for this particular example converges for all models. Therefore, no coupling is necessary for a steady state, static model. However, the dynamics of the simulation are affected by the numerical scheme. In this simulation, the total temperature error between the two grids approached 90% of the total initial temperature difference during the early stages of the simulation. It is found that the velocity-coupling alone removes the discrepancy between the two grids throughout the simulation for the temperatures as well as the velocities. This is due to the dominant influence of the velocities on the calculation of the thermal equilibrium distribution. These results verify the thermal model in the static case; however, the steady-state flow case needs to be analyzed as well. For this, the static droplet simulation is again utilized.

5.4.2 Static Droplet

A liquid water droplet surrounded by water vapor is simulated in a fully periodic domain at 500 K with $g_{A,B} = 0.05$ and $g_{B,A} = 0.005$. The simulation is performed using the thermal two-component model so that the phases maintain immiscibility. Mass and momentum conservation are considered first for the model with no coupling, temperature-coupling only, velocity-coupling only, and both temperature and velocity coupling. These are verified in all cases. This is to be expected given the formulation of the coupling models (the velocity coupling is constructed such that conservation is ensured) and the implementation of a full periodic domain (no mass or momentum can enter or leave the system). Next, the internal energy conservation of the models is analyzed, the results of which are given in Figure 40.



(a) Temperature errors



(b) Velocity magnitude errors

Figure 39: Temperature and velocity errors that result from using no coupling of the macroscopic variables (None), only the temperature-coupling model (TC), only the velocity-coupling model (VC), and the temperature and velocity-coupling models used together (TCVC) in the MPiMC-T model as the thermal conduction simulation evolves through time. Note that the results from TC, VC, and TCVC all overlap for the temperature errors, but only the results from VC and TCVC overlap for the velocity errors.

It is found that the temperature-coupling model used alone leads to a large violation of internal energy conservation, whereas the other models behave correctly. In fact, the error in energy conservation is so severe that it leads to the rapid divergence of the simulation. This is a result of the erroneous temperature profile causing density ratios too large to be handled by the LBM. It should be noted that the model with no coupling will always conserve mass, momentum, and energy for a full periodic domain; however, the model is physically incorrect as it allows a discrepancy between the macroscopic properties of nodes between the different numerical grids. This is clear when the model errors are considered again, as in the previous section. The temperature error and velocity magnitude error are shown for the static droplet simulation in Figure 41. These results confirm that the model used without any coupling, as well as the temperature-coupled model used alone, yield physically inconsistent results. Furthermore, the influence of steady-state flow can be seen to lead to a persistent error, unlike the static case in which all of the models eventually converged. As before, the velocity-coupling used alone leads to correct behavior but the temperature-coupling is included for physical consistency.

A closer inspection of the velocities leads to better insight into the performance of the models. Figures 42a and 42b show a comparison of the velocity vectors of the steady-state solution of the static droplet simulation for the model with no coupling and the model with both temperature and velocity coupling, respectively. The left hand sides of the figures show the first grid (a liquid water droplet surrounded by a zero-density region) and the right-hand sides show the second grid (water vapor surrounding a zero-density bubble). The shaded region in the center of the domain shows the location of the liquid droplet. As can be seen, the maximum velocity magnitudes in the coupled model are lower than the magnitudes of the model without coupling. This is due to the fact that the spurious currents that are a consequence of the anisotropies in the discrete gradient operator occur primarily in the zero-density regions (outside the liquid droplet on the first grid and inside the zero-density bubble on the second grid). Thus, weighting via the densities aids in the removal of the effect of these spurious currents. The errors in conservation and the discrepancies between the two grids exist in this case only as a result of the spurious currents. This is why the static case of thermal conduction led to eventual convergence for all models, whereas the steady-state flow

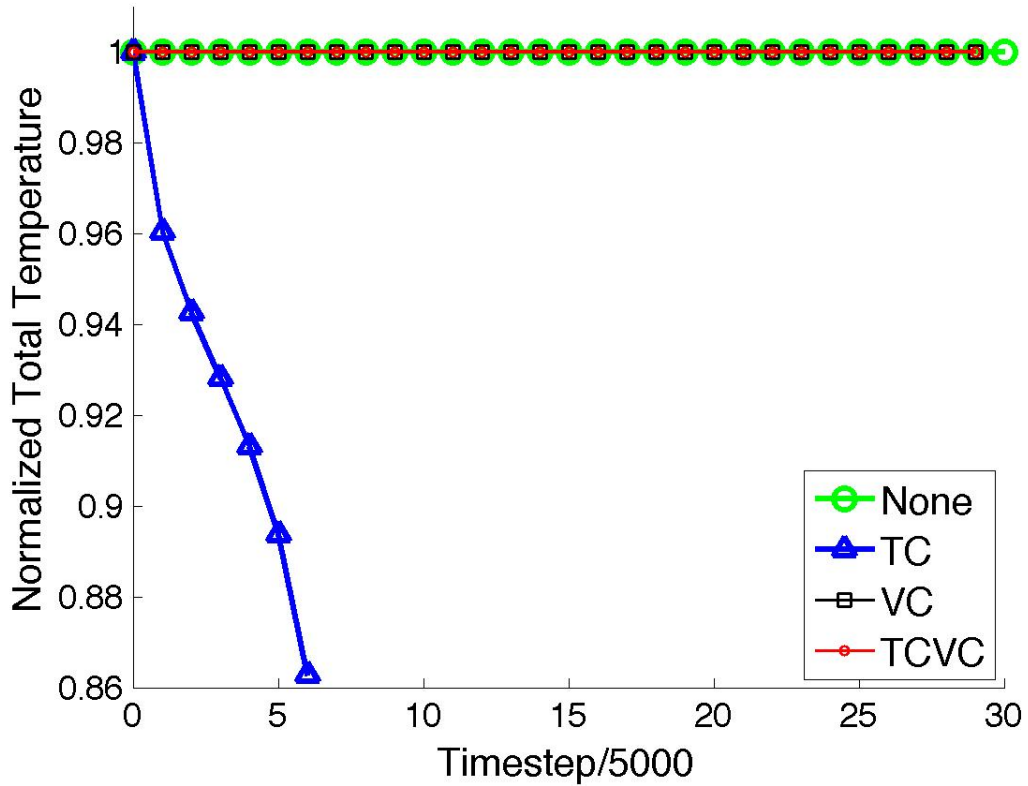


Figure 40: Comparison of the evolution of the total temperature in the domain using no coupling of the macroscopic variables (None), only the temperature-coupling model (TC), only the velocity-coupling model (VC), and the temperature and velocity-coupling models used together (TCVC) in the MPiMC-T LB model for a static droplet simulation. Note that the results from None, VC, and TCVC all overlap.

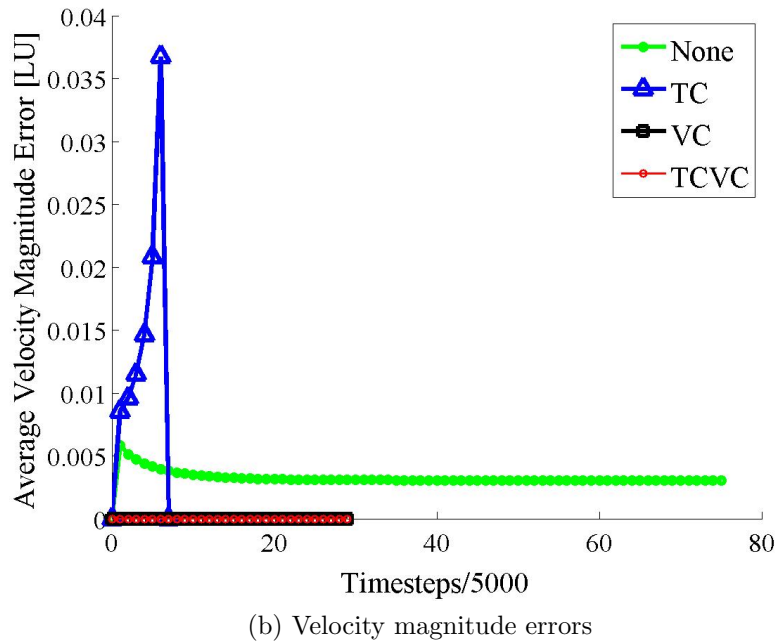
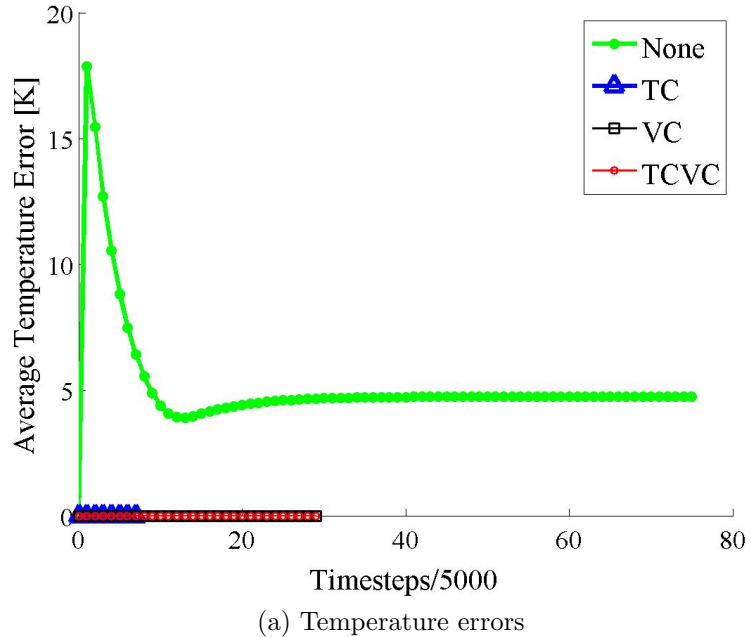


Figure 41: Temperature and velocity errors that result from relaxing the coupling requirements in the MPiMC-T model as the static droplet simulation evolves through time. Note that the results from TC, VC, and TCVC all overlap for the temperature errors, but only the results from VC and TCVC overlap for the velocity errors.

case does not. Therefore, by reducing the influence of the spurious currents, the accuracy of the models is improved. The next step is to verify the dynamic thermal model, with induced flow fields.

5.4.3 Thermocapillary Migration

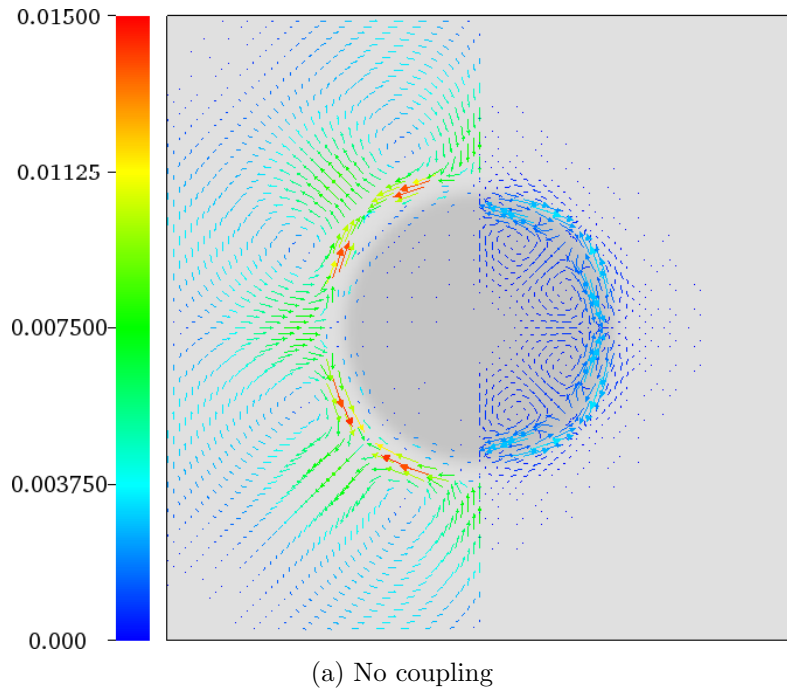
Thermocapillary migration is chosen as a benchmark for the thermal, immiscible, two component, two-phase, dynamic flow model due to the existence of analytic expressions describing the flow dynamics. Thermocapillary motion was first studied by Young, et al. [78], who noted the occurrence of steady migration patterns of non-deformable droplets exposed to linear temperature gradients. In the quasi-steady limit the droplet velocity can be expressed as [78]:

$$V_{droplet} = \frac{2\nu_0}{(2 + 3\alpha)(2 + \beta)}, \quad (5.23)$$

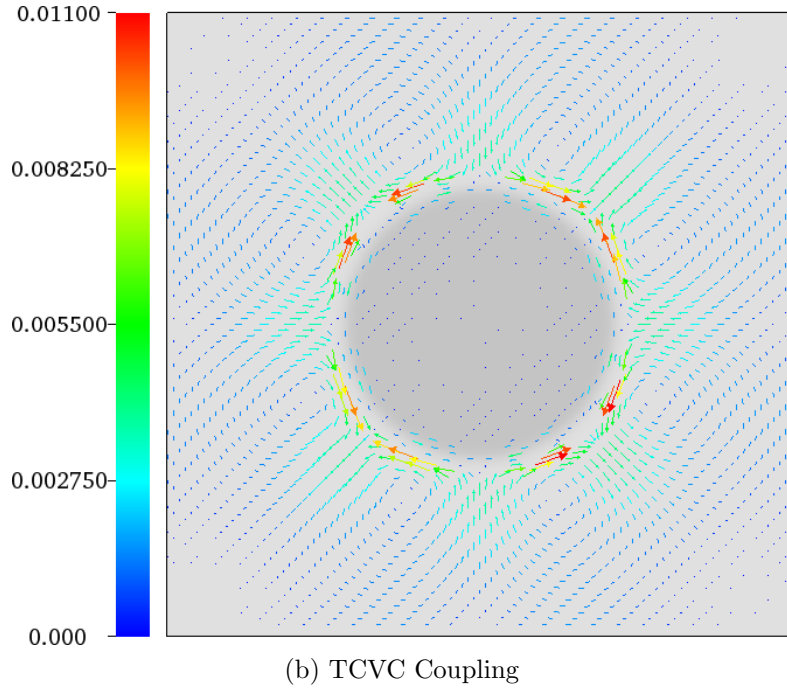
where $\alpha = \mu_2/\mu_1$ is the ratio of the dynamic viscosity of the liquid phase to the vapor phase, $\beta = k_2/k_1$ is the ratio of the thermal conductivities, and:

$$\nu_0 = \frac{|\sigma_T| |\nabla T| R}{\mu}, \quad (5.24)$$

is a reference velocity, in which ∇T is the imposed temperature gradient, R is the drop radius, and σ_T is the gradient of the interfacial tension with temperature. This analytic derivation is based on the existence of an immiscible droplet of a fixed shape, surrounded by a continuous fluid of infinite extent. This droplet and the surrounding fluid are assumed to have physical properties independent of the temperature, with the exception of the surface tension, and the evaluation is considered as the Reynolds and Marangoni numbers go to zero (the case of negligible inertial effects) [79]. Thus, for a given system with constant thermophysical properties, the quasi-steady velocity changes in proportion to the temperature gradient alone. A series of LBM simulations is performed in which a liquid water droplet, surrounded by air, is exposed to temperature gradients of 0 K to 150 K. The domain is initialized with periodicity in the x -direction, a heated lower wall, and a cooled upper wall. The droplet is placed at the center of the domain in a quiescent fluid. The surrounding air quickly equilibrates to a linear conduction profile. During this time, there is a slight unsteady perturbation of the



(a) No coupling



(b) TCVC Coupling

Figure 42: Comparison of the spurious currents in the steady-state static droplet simulation using the model with no coupling and the model with both temperature and velocity-coupling.

droplet, but the droplet quickly reaches a quasi-steady migration in which it moves toward the lower wall without the presence of any external body forces. The droplet progression during various timesteps is shown in Figure 43.

The centers of the droplets through time are plotted for the different temperature gradients in Figure 44. The source of the unsteady behavior seems to indicate a numerical effect due to the droplets all crossing the initial location at the same time, rather than being temperature dependent in some manner. The cause of this behavior is unclear at this point and warrants further investigation. Nevertheless, the existence of the overall flow behavior across all temperature gradients considered, and the variation in the quasi-steady velocities with the variation in temperature gradients indicates that the thermocapillary flow dominates any unsteady behavior.

Linear best fits of the droplet locations in each of the simulations are then performed in the regions of each that best approximate the quasi-steady migration event. The slopes of these fits correspond to the quasi-steady droplet velocities. The individual velocities are then all normalized by the 25 K flow case and are plotted in Figure 45. A one-to-one relationship is predicted by Equations (5.23) and (5.24). For instance,

$$\frac{V_{50}}{V_{25}} = \frac{|\sigma_{T,50}|}{|\sigma_{T,25}|} = 2. \quad (5.25)$$

The velocities follow a proportional relationship to the temperature gradients with reasonable accuracy. A linear fit of the velocity data has a slope of 0.99, an intercept of 0.1075, and an R^2 value of 0.99. The fidelity of this fit is dependent on the selection of the quasi-steady regions. The regions utilized for the fitting processes are indicated in Figure 46 by the filled datapoints. These points are chosen by requiring the fit to begin after the unsteady initial behavior, but before 15,000 timesteps is surpassed. The fit is also performed under the constraint that at least 20 datapoints are included in the analysis to provide an accurate picture of the steady flow behavior.

The Reynolds numbers of the simulations can be calculated as:

$$Re = \nu_0 R / \mu, \quad (5.26)$$

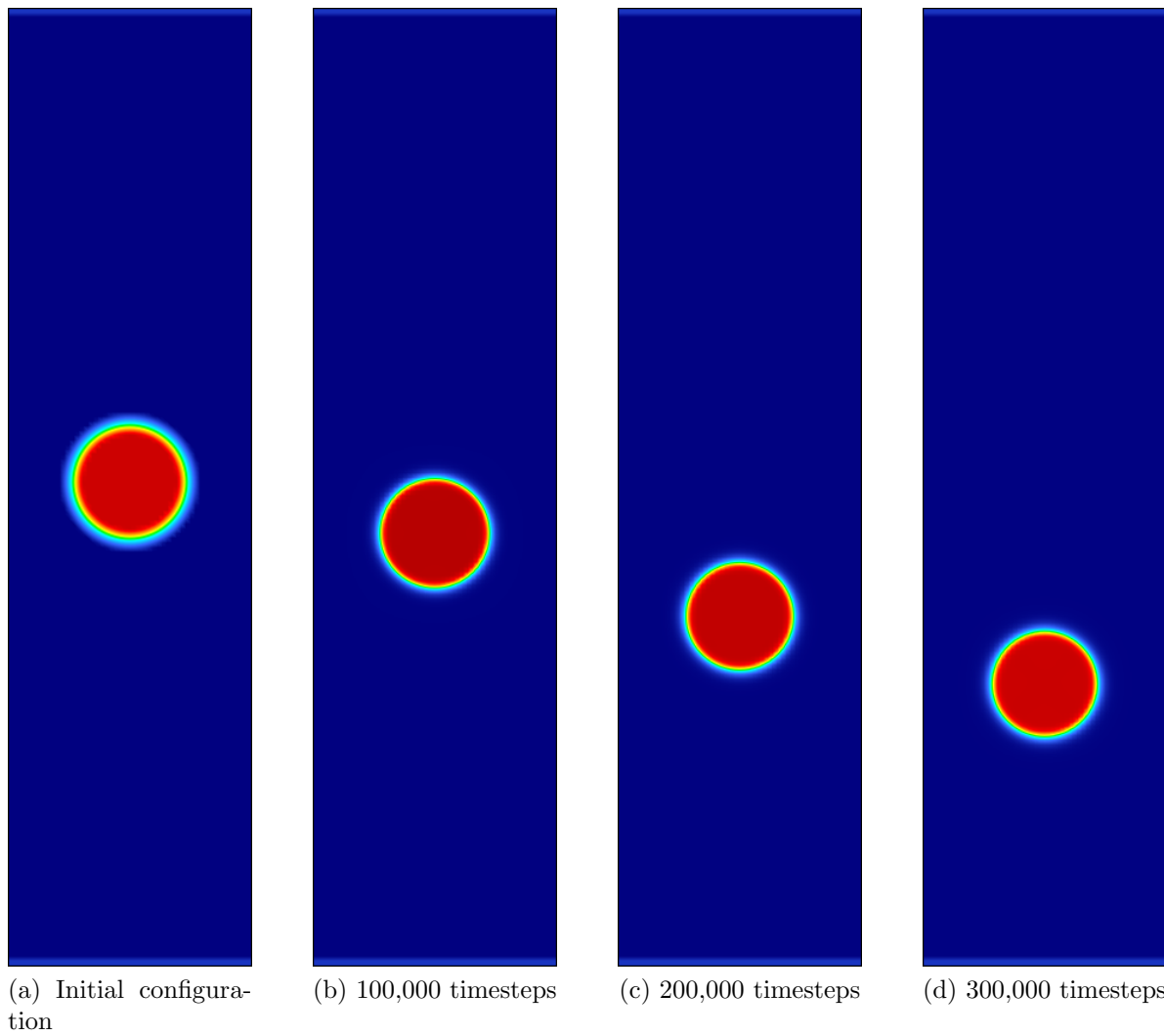


Figure 43: Progression of a liquid droplet surrounded by air due to thermocapillary migration shown at various timesteps during the simulation.

where ν_0 is given by Equation 5.24, R is the radius of the droplet, and μ is the dynamic viscosity of the surrounding fluid. It is found that the Reynolds numbers for all simulations range between 0.02 and 0.15, justifying the low Re assumption that was the basis of the analytic expression for the quasi-steady velocity. The simulations are performed at a Prandtl number of one, leading to Marangoni numbers ($Ma = RePr$), in the same range as the Reynolds numbers. Furthermore, the Weber numbers are shown to remain low, varying from 0.0005 to 0.0175. Thus, it can be stated that the thermal, dynamic, multiphase, multicomponent simulation is behaving properly in relation to the analytic expression.

In conclusion, a multiphase, immiscible, multicomponent thermal (MPiMC-T) lattice Boltzmann model has been developed and described. It has been validated using static, steady-state, and dynamic flows with well-understood physics. The model is shown to conserve mass, momentum, and energy and maintains the physical requirement that the macroscopic properties are equal at overlapping spatial locations.

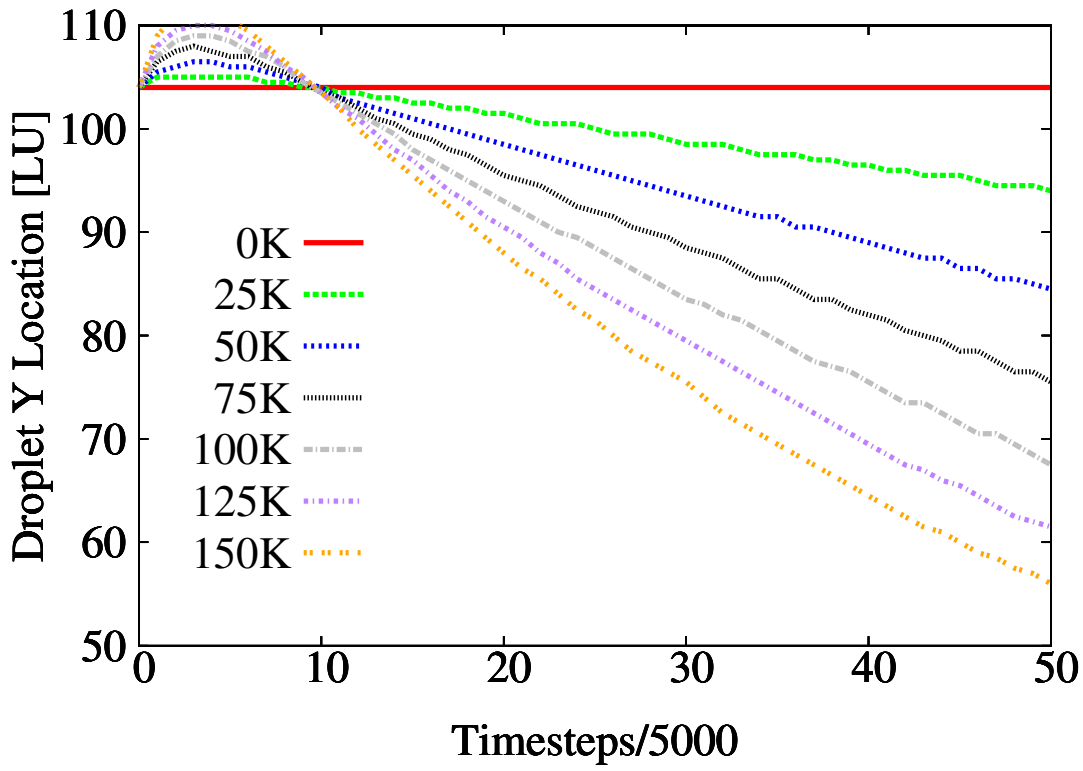


Figure 44: Droplet location during thermocapillary migration studies at various temperatures.

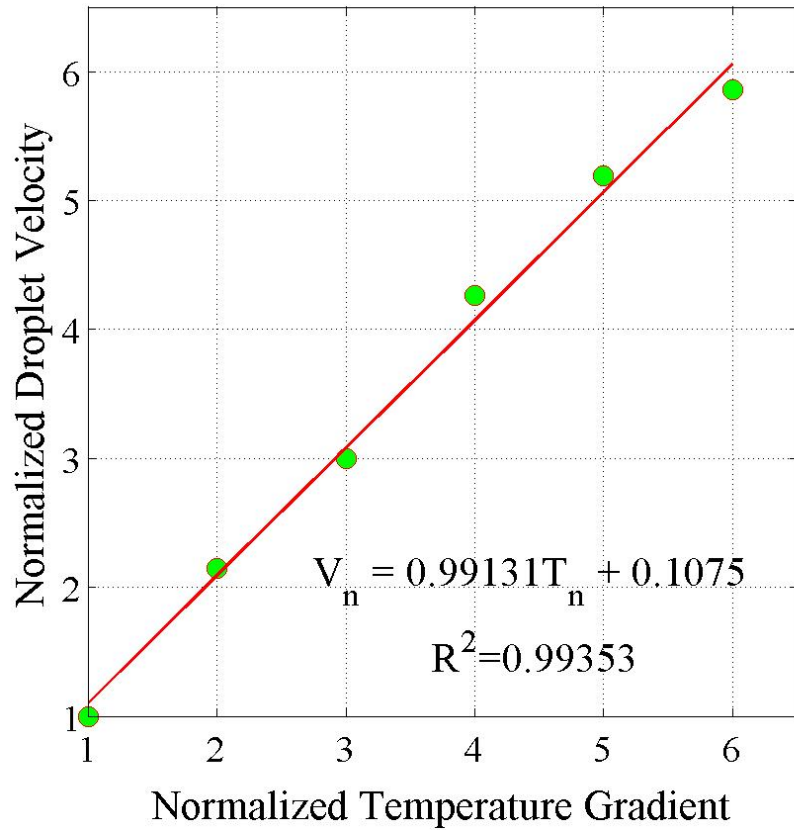


Figure 45: Thermocapillary droplet migration velocities, normalized by the 25 K thermal gradient case.

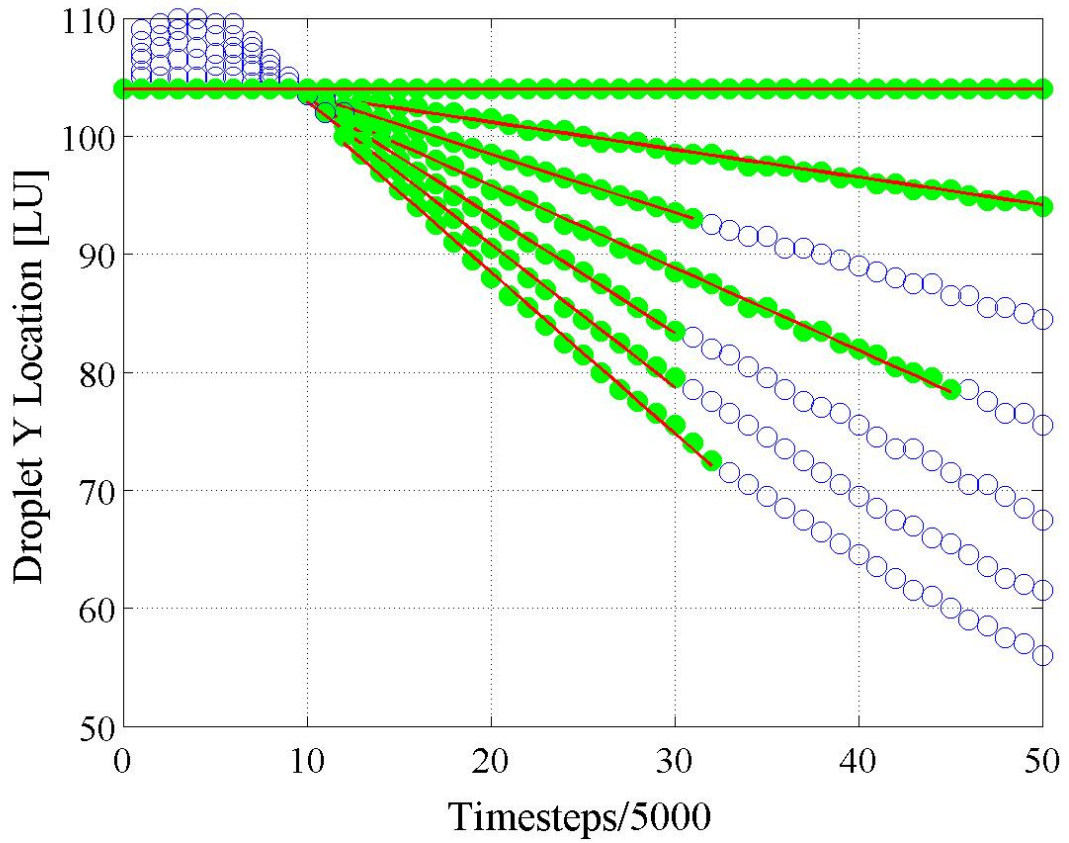


Figure 46: Droplet location during thermocapillary migration studies at various temperatures. Filled datapoints represent those used for the determination of the droplet velocity in the quasi-steady flow regime.

6.0 CONCLUSIONS AND FUTURE WORK

6.1 PRIMARY CONTRIBUTIONS

A number of important developments to the lattice Boltzmann method for fluid flow simulation have been made. The following is a summary of the accomplishments of this work.

6.1.1 Multiphase, single-component, isothermal model gradient operator approximation

A method for estimating the gradient operator used for the interaction between phases, based on the linear combination of local and mean value approximations, was implemented with the Peng-Robinson equation of state (PR-EOS). The weighting of the linear combination was found for a liquid water droplet surrounded by water vapor for this EOS and it was shown to yield more accurate density ratios at lower temperatures. As a result, the stability of the simulation at lower temperatures and higher density ratios was improved for the PR-EOS. This opens the possibility for the simulation of a larger range of flows, extending the applicability of the multiphase lattice Boltzmann method. As shown in Chapter 3, density ratios over 1000:1 can be accurately simulated with this methodology. This corresponds to reduced temperatures below 0.6, or 375 K for liquid-vapor water systems, which brings typical heat exchanger flows within reach of these simulation techniques.

6.1.2 Multiphase, single component, thermal wall interaction model

A novel wall interaction model was developed to account for the thermal dependence of the contact angle. A general function describing the wetting behavior was used for the dynamic

calculation of the wall interparticle interaction strength parameter utilized in the calculation of the wall interaction force. In this manner, wall wetting simulations were performed and shown to correlate well to the prescribed functions. It was discovered that at low temperatures and high contact angles, a simple quadratic correlation can be utilized with an analytic solver for rapid solution of the wall interaction parameter. However, for functions yielding low contact angles or simulations at high temperatures, cubic fitting functions are required, necessitating a Newton-Raphson solver and leading to an increase in computation time. The effects of the dynamic wall wetting functions on overall flow behavior are shown via flow boiling simulations. This development provides a framework which will allow further analysis of wall wetting phenomena, including investigation into flow behavior at the three-phase contact line. Such behavior is important in innumerable applications, from cooling microelectronics using two-phase heat exchangers to diagnosing diseases from blood evaporation pattern analyses [1].

6.1.3 Multiphase, immiscible, multicomponent, isothermal model stability analysis

The parameters which control the intercomponent interaction strength were analyzed over a wide range to determine those which yield stable and valid immiscible results. These parameters were then compared across various temperatures in order to determine overlap in the regions of stability. In this manner, a valid parameter space for a multiphase, immiscible, multicomponent, thermal model is constructed which will remain stable over large thermal variations.

6.1.4 Multiphase, immiscible, multicomponent, thermal model

A lattice Boltzmann model has been developed for the simulation of multiphase, immiscible, multicomponent, thermal systems. A density-weighted coupling of the temperatures and hydrodynamic velocities was implemented in order to preserve global mass, momentum, and energy conservation. Static thermal conduction and static droplet simulations were performed to validate the model. Finally, thermocapillary migration was simulated and the

model successfully reproduced the quasi-steady flow velocities expected for low Reynolds number flows. The development of this model marks a significant improvement of the lattice Boltzmann method. With such a model, along with the improvements described above, the simulation of realistic thermal systems is becoming feasible. For instance, the detailed evaluation of a closed heat pipe system, which operates on the principle of heat exchange through evaporation and condensation of a working fluid, requires modeling a multicomponent, multiphase thermal flow. Such an analysis would present an enormous improvement over the traditional bulk property analyses that currently comprise heat pipe modeling. Additionally, the combustion community is rapidly growing and is in need of more detailed models for the simulation of multicomponent, multiphase, thermal flows. The developments shown here mark significant progress toward such simulations.

6.2 FUTURE WORK

The field of LBM fluid simulation is very large and yet relatively young. As a result, there are a great deal of exciting avenues in need of in-depth analysis and development. A few of the areas specifically related to the work presented here are described below.

6.2.1 Incorporation of the Wall Interaction Model in MPiMC-T model

The wall interaction model developed in this work was implemented into the multiphase, single component model. However, the same argument made concerning the variability of wetting behavior in single component thermal flows will be just as true in multicomponent systems. Implementation of the wall interactions will be far more complicated in the multicomponent model due to the increase in the parameter space. Each component is capable of interacting with the wall, with itself, and with other components.

Additionally, the improvements made here are based on correlations to experimental functions relating contact angles and temperatures. A more fundamental approach would be to model the wall interaction strength using the inherent thermal dependence of the

surface energies. However, this technique requires a better understanding of the underlying thermodynamics at the contact point for both the single and the multicomponent models, as well as the development of a method capable of incorporating these models into the LBM.

6.2.2 Gradient Approximations

The linear approximation for the gradient operator used in multiphase flow simulations is a correlative method. While sufficient for the current work, numerical schemes capable of modeling discontinuities have been developed for the simulation of shock interfaces. Such schemes, if they can be made sufficiently isotropic, would be an interesting and worthwhile development in the LBM for the improvement of high-density ratio flow simulations with reduced spurious currents.

6.2.3 Homogeneous Nucleation

The multiphase, multicomponent, thermal framework developed here has set the groundwork for further studies into interesting phenomena. In particular, the simulation of the homogeneous nucleation process would be very interesting. In order to predict such behavior, the numerical scheme would need to include a process for modeling the random perturbations inherent in any real system, which are thought to be responsible for the homogeneous nucleation process. However, this must be implemented while maintaining conservation principles and thermodynamic consistency.

6.2.4 Higher-Order Thermal Lattice Boltzmann Model

Ultimately, the LBM requires further fundamental development of the underlying thermal models. In this work, the passive-scalar method was utilized for the solution of the energy equation. This model was chosen for its computational simplicity and its clear interpretation. However, as described in Chapter 2, higher order moments can be calculated directly from the PDFs. These moments include additional information about the system dynamics, such as the momentum and energy fluxes. Thus, it is possible to determine information

about the energy evolution of the domain directly from the information stored in the PDFs. While possible, this is greatly complicated by the requirements on the equilibrium distribution function and the Gauss-Hermite quadrature that comprises the underlying lattice. Preserving information in the higher velocity moments requires higher-order expansions in the equilibrium distributions and larger numbers of lattice velocities. The difficulty of this approach is immense from both a theoretical and a practical perspective. Nevertheless, this technique represents the ultimate goal in lattice Boltzmann thermal fluid flow simulation due to its strong fundamental underpinnings.

6.2.5 Comparison to Alternative Multiphase Methods

The lattice Boltzmann method has been improved to incorporate more complex physical phenomena. However, there are still a number of limitations to the LBM. For instance, in the model used in this work, the flows are restricted to the low Reynolds number and low Prandtl number regimes. Additionally, spurious currents are shown to form around interfaces due to anisotropies of the discrete gradient operators. These currents lead to a violation of the low Reynolds number assumption at very high density ratios. Thus, more investigation is needed to improve these models. The previous chapters and the sections above have provided some insight into the sources of these shortcomings and some potential paths forward. It is clear though that the LBM is finally reaching a sufficient level of complexity and accuracy that comparison to alternative multiphase, multicomponent, thermal models is warranted. Alternative simulation techniques, such as the volume-of-fluid (VOF) and the level-set (LS) methods have seen a great deal of development, but are plagued by the immense computational cost of solving the traditional Navier-Stokes equations, coupled with the solution of an interface advection equation. Furthermore, for the simulation of thermal flows with phase changes, the energy and mass transfer equations must also be solved, making the calculations even more expensive. As with the LBM, these methods also have limitations. For instance, the VOF method struggles to recreate a true interface between phases and the LS method often leads to violations of conservation of mass at the interface. Ultimately, the lattice Boltzmann method is based on more fundamental physics, that of the Boltzmann transfer

equation. However, it is not clear, given the current state of all of these methods, which is best for the reliable and efficient calculation of multiphase, multicomponent, thermal flows. A thorough comparison of the computational costs framed in the context of numerical accuracy, has yet to be undertaken. Such an analysis is vital to elucidate both the strengths and the weaknesses of the LBM as a numerical tool for simulating this complex behavior.

BIBLIOGRAPHY

- [1] K. Sefiane, M. Shanahan, M. Antoni, *Wetting and phase change: opportunities and challenges*, Current Opinion in Colloid & Interface Science, **Vol. 16** pp. 317–325 (2011).
- [2] S. G. Kandlikar, *Fundamental issues related to flow boiling in minichannels and microchannels*, Experimental Thermal and Fluid Science, **Vol. 26 (2-4)** pp. 389–407 (2002).
- [3] W. Qu, I. Mudawar, *Flow boiling heat transfer in two-phase micro-channel heat sinks - I. Experimental investigation and assessment of correlation methods*, International Journal of Heat and Mass Transfer, **Vol. 46 (15)** pp. 2755–2771 (2003).
- [4] S. G. Kandlikar, *Heat Transfer Mechanisms During Flow Boiling in Microchannels*, Journal of Heat Transfer, **Vol. 126 (1)** pp. 8–16 (2004).
- [5] S. Kandlikar, *High Flux Heat Removal with Microchannels - A Roadmap of Challenges and Opportunities*, Heat Transfer Engineering, **Vol. 26 (8)** pp. 5–14 (2005).
- [6] S. G. Kandlikar, W. K. Kuan, D. A. Willistein, J. Borrelli, *Stabilization of Flow Boiling in Microchannels Using Pressure Drop Elements and Fabricated Nucleation Sites*, Journal of Heat Transfer, **Vol. 128 (4)** pp. 389–396 (2006).
- [7] S. V. Garimella, V. Singhal, D. Liu, *On-Chip Thermal Management With Microchannel Heat Sinks and Integrated Micropumps*, Proceedings of the IEEE, **Vol. 94 (8)** pp. 1534–1548 (2006).
- [8] L. Cheng, G. Ribatski, J. R. Thome, *Two-Phase Flow Patterns and Flow-Pattern Maps: Fundamentals and Applications*, Applied Mechanics Reviews, **Vol. 61 (5)** p. 050802 (2008).
- [9] H. J. Lee, D. Y. Liu, S.-C. Yao, *Flow instability of evaporative micro-channels*, International Journal of Heat and Mass Transfer, **Vol. 53 (9-10)** pp. 1740 – 1749 (2010).
- [10] H. J. Lee, D. Y. Liu, Y. Alyousef, S.-C. Yao, *Generalized Two-Phase Pressure Drop and Heat Transfer Correlations in Evaporative Micro/Minichannels*, Journal of Heat Transfer, **Vol. 132 (4)** p. 041004 (2010).

- [11] T. Zhang, Y. Peles, J. T. Wen, M. K. Jensen, *Two-phase flow instability analysis for transient electronics cooling*, in *Thermal and Thermomechanical Phenomena in Electronic Systems (ITherm)*, 2010 12th IEEE Intersociety Conference on, pp. 1–9 (2010).
- [12] S. G. Kandlikar, *Scale effects on flow boiling heat transfer in microchannels: A fundamental perspective*, International Journal of Thermal Sciences, **Vol. 49 (7)** pp. 1073 – 1085 (2010).
- [13] S. Kakaç, *Microscale heat transfer: fundamentals and applications*, Springer (2005).
- [14] S. V. Garimella, A. S. Fleischer, J. Y. Murthy, A. Keshavarzi, R. Prasher, C. Patel, S. H. Bhavnani, R. Venkatasubramanian, R. Mahajan, Y. Joshi, B. Sammakia, B. A. Myers, L. Chorosinski, M. Baelmans, P. Sathyamurthy, P. E. Raad, *Thermal Challenges in Next-Generation Electronic Systems*, Components and Packaging Technologies, IEEE Transactions on, **Vol. 31 (4)** pp. 801–815 (2008).
- [15] D. B. Tuckerman, R. F. W. Pease, *High-performance heat sinking for VLSI*, Electron Device Letters, IEEE, **Vol. 2 (5)** pp. 126–129 (1981).
- [16] W. F. Hughes, J. A. Brighton, *Schaum's outline of theory and problems of fluid dynamics*, Schaum's outline series, McGraw Hill (1999).
- [17] A. Mukherjee, S. G. Kandlikar, *Numerical simulation of growth of a vapor bubble during flow boiling of water in a microchannel*, Microfluidics and Nanofluidics, **Vol. 1 (2)** pp. 137–145 (2005).
- [18] Z. Yu, *A Novel Lattice Boltzmann Method for Direct Numerical Simulation of Multiphase Flows*, Ph.D. Thesis, Ohio State University (2009).
- [19] T. L. Hill, *An Introduction to Statistical Thermodynamics*, McGraw-Hill series in advanced chemistry, Dover Publications (1987).
- [20] Exa Corporation, URL www.prweb.com/releases/Exa/Porsche/prweb4110304.htm.
- [21] S. Chen, G. D. Doolen, *Lattice Boltzmann method for fluid flows*, Annual Review of Fluid Mechanics, **Vol. 30 (1)** pp. 329–364 (1998).
- [22] C. K. Aidun, J. R. Clausen, *Lattice-Boltzmann method for complex flows*, Annual Review of Fluid Mechanics, **Vol. 42 (1)** pp. 439–472 (2010).
- [23] R. Zhang, X. Shan, H. Chen, *Efficient kinetic method for fluid simulation beyond the Navier-Stokes equation*, Phys. Rev. E, **Vol. 74** p. 046703 (2006).
- [24] L. Zhu, D. Tretheway, L. Petzold, C. Meinhart, *Simulation of fluid slip at 3D hydrophobic microchannel walls by the lattice Boltzmann method*, Journal of Computational Physics, **Vol. 202 (1)** pp. 181 – 195 (2005).

- [25] X. Nie, G. D. Doolen, S. Chen, *Lattice-Boltzmann simulations of fluid flows in MEMS*, Journal of Statistical Physics, **Vol. 107 (1-2)** pp. 279–289 (2002).
- [26] URL www.scopus.com/home.url.
- [27] X. Shan, H. Chen, *Simulation of nonideal gases and liquid-gas phase transitions by the lattice Boltzmann equation*, Phys. Rev. E, **Vol. 49 (4)** pp. 2941–2948 (1994).
- [28] R. Zhang, H. Chen, *Lattice Boltzmann method for simulations of liquid-vapor thermal flows*, Phys. Rev. E, **Vol. 67** p. 066711 (2003).
- [29] M. C. Sukop, D. Or, *Lattice Boltzmann method for homogeneous and heterogeneous cavitation*, Phys. Rev. E, **Vol. 71** p. 046703 (2005).
- [30] P. Yuan, *Thermal lattice Boltzmann two-phase flow model for fluid dynamics*, Ph.D. Thesis, University of Pittsburgh (2005).
- [31] P. Yuan, L. Schaefer, *Equations of state in a lattice Boltzmann model*, Physics of Fluids, **Vol. 18 (4)** p. 042101 (2006).
- [32] H. Huang, Z. Li, S. Liu, X.-y. Lu, *Shan-and-Chen-type multiphase lattice Boltzmann study of viscous coupling effects for two-phase flow in porous media*, International Journal for Numerical Methods in Fluids, **Vol. 61 (3)** pp. 341–354 (2009).
- [33] P. K. Jain, A. Tentner, Rizwan-uddin, *A lattice Boltzmann framework to simulate boiling water reactor core hydrodynamics*, Computers & Mathematics with Applications, **Vol. 58 (5)** pp. 975 – 986 (2009).
- [34] S. Gong, P. Cheng, *Numerical investigation of droplet motion and coalescence by an improved lattice Boltzmann model for phase transitions and multiphase flows*, Computers & Fluids, **Vol. 53** pp. 93 – 104 (2012).
- [35] X.-P. Chen, C.-W. Zhong, X.-L. Yuan, *Lattice Boltzmann simulation of cavitating bubble growth with large density ratio*, Computers & Mathematics with Applications, **Vol. 61 (12)** pp. 3577 – 3584 (2011).
- [36] J. Bao, *High density ratio multi-component lattice Boltzmann flow model for fluid dynamics and CUDA parallel computation*, Ph.D. Thesis, University of Pittsburgh (2010).
- [37] X. Nie, X. Shan, H. Chen, *Lattice-Boltzmann/Finite-Difference Hybrid Simulation of Transonic Flow*, in *Proceedings of the 47th AIAA Aerospace Sciences Meeting*, pp. 139.1–139.8 (2009).
- [38] X. Shan, *Analysis and reduction of the spurious current in a class of multiphase lattice Boltzmann models*, Phys. Rev. E, **Vol. 73** p. 047701 (2006).

- [39] P. L. Bhatnagar, E. P. Gross, M. Krook, *A Model for Collision Processes in Gases. I. Small Amplitude Processes in Charged and Neutral One-Component Systems*, Phys. Rev., **Vol. 94** pp. 511–525 (1954).
- [40] X. He, L.-S. Luo, *Theory of the lattice Boltzmann method: From the Boltzmann equation to the lattice Boltzmann equation*, Phys. Rev. E, **Vol. 56** pp. 6811–6817 (1997).
- [41] S. Wolfram, *Cellular automaton fluids 1: Basic theory*, Journal of Statistical Physics, **Vol. 45** pp. 471–526 (1986).
- [42] D. A. Wolf-Gladrow, *Lattice Boltzmann models*, Vol. 1725 of *Lecture notes in mathematics*, chap. 5, Springer Berlin, pp. 159–246 (2004).
- [43] X. Shan, X. He, *Discretization of the velocity space in the solution of the Boltzmann equation*, Phys. Rev. Lett., **Vol. 80** pp. 65–68 (1998).
- [44] S. Succi, *The lattice Boltzmann equation for fluid dynamics and beyond*, Numerical mathematics and scientific computation, Clarendon Press (2001).
- [45] T. Inamuro, M. Yoshino, F. Ogino, *A non-slip boundary condition for lattice Boltzmann simulations*, Physics of Fluids, **Vol. 7 (12)** pp. 2928–2930 (1995).
- [46] Q. Zou, X. He, *On pressure and velocity boundary conditions for the lattice Boltzmann BGK model*, Physics of Fluids, **Vol. 9 (6)** pp. 1591–1598 (1997).
- [47] J. Latt, B. Chopard, *Straight velocity boundaries in the lattice Boltzmann method*, Physical Review E, **Vol. 77 (5)** pp. 1–16 (2008).
- [48] J. Latt, O. Malaspinas, *Palabos Project Documentation: Boundary conditions*, URL <http://www.palabos.org/wiki/> (2008).
- [49] L.-S. Luo, *Unified Theory of Lattice Boltzmann Models for Nonideal Gases*, Phys. Rev. Lett., **Vol. 81** pp. 1618–1621 (1998).
- [50] L.-S. Luo, *Theory of the lattice Boltzmann method: Lattice Boltzmann models for non-ideal gases*, Phys. Rev. E, **Vol. 62** pp. 4982–4996 (2000).
- [51] X. He, X. Shan, G. D. Doolen, *Discrete Boltzmann equation model for nonideal gases*, Phys. Rev. E, **Vol. 57** pp. R13–R16 (1998).
- [52] Z. Guo, C. Zheng, B. Shi, *Discrete lattice effects on the forcing term in the lattice Boltzmann method*, Phys. Rev. E, **Vol. 65 (4)** p. 046308 (2002).
- [53] A. Kupershtokh, D. Medvedev, D. Karpov, *On equations of state in a lattice Boltzmann method*, Computers & Mathematics with Applications, **Vol. 58 (5)** pp. 965 – 974 (2009).
- [54] A. L. Kupershtokh, *New method of incorporating a body force term into the lattice Boltzmann equation*, in *5th International EHD Workshop* (2004).

- [55] F. White, *Viscous fluid flow*, McGraw-Hill series in mechanical engineering, McGraw-Hill Higher Education (2006).
- [56] J. Latt, *Palabos Project Documentation: Choice of units in lattice Boltzmann simulations*, URL <http://www.palabos.org/wiki/> (2008).
- [57] T. Harirchian, S. V. Garimella, *A comprehensive flow regime map for microchannel flow boiling with quantitative transition criteria*, International Journal of Heat and Mass Transfer, **Vol. 53 (13-14)** pp. 2694–2702 (2010).
- [58] X. Shan, H. Chen, *Lattice Boltzmann model for simulating flows with multiple phases and components*, Phys. Rev. E, **Vol. 47 (3)** pp. 1815–1819 (1993).
- [59] X. Shan, G. Doolen, *Multicomponent lattice-Boltzmann model with interparticle interaction*, Journal of Statistical Physics, **Vol. 81** pp. 379–393 (1995).
- [60] M. Sukop, D. Thorne, *Lattice Boltzmann modeling: an introduction for geoscientists and engineers*, Springer (2006).
- [61] M. Sbragaglia, R. Benzi, L. Biferale, S. Succi, K. Sugiyama, F. Toschi, *Generalized lattice Boltzmann method with multirange pseudopotential*, Physical Review E, **Vol. 75 (2)** pp. 1–13 (2007).
- [62] S. Walas, *Phase Equilibria in Chemical Engineering*, Butterworth Publishers (1985).
- [63] M. S. Plesset, S. A. Zwick, *The Growth of Vapor Bubbles in Superheated Liquids*, Journal of Applied Physics, **Vol. 25 (4)** pp. 493 –500 (1954).
- [64] B. Shi, V. K. Dhir, *Molecular dynamics simulation of the contact angle of liquids on solid surfaces*, The Journal of Chemical Physics, **Vol. 130 (3)** 034705 (2009).
- [65] M. Brugnara, <http://rsbweb.nih.gov/ij/plugins/contact-angle.html> (2006).
- [66] C. A. Ward, J. Wu, *Effect of Adsorption on the Surface Tensions of SolidFluid Interfaces*, The Journal of Physical Chemistry B, **Vol. 111 (14)** pp. 3685–3694 (2007).
- [67] C. Ward, K. Sefiane, *Adsorption at the solid-liquid interface as the source of contact angle dependence on the curvature of the three-phase line*, Advances in Colloid and Interface Science, **Vol. 161 (1-2)** pp. 171 – 180 (2010).
- [68] A. Bahramian, A. Danesh, *Prediction of solid-fluid interfacial tension and contact angle*, Journal of Colloid and Interface Science, **Vol. 279 (1)** pp. 206 – 212 (2004).
- [69] D. Kwok, A. Neumann, *Contact angle interpretation in terms of solid surface tension*, Colloids and Surfaces A: Physicochemical and Engineering Aspects, **Vol. 161 (1)** pp. 31 – 48 (2000).

- [70] D. Kwok, A. Neumann, *Contact angle interpretation: re-evaluation of existing contact angle data*, Colloids and Surfaces A: Physicochemical and Engineering Aspects, **Vol. 161 (1)** pp. 49 – 62 (2000).
- [71] Z. L. Yang, T. N. Dinh, R. R. Nourgaliev, B. R. Sehgal, *Numerical investigation of bubble growth and detachment by the lattice-Boltzmann method*, International Journal of Heat and Mass Transfer, **Vol. 44 (1)** pp. 195–206 (2001).
- [72] J. Zhang, D. Y. Kwok, *Lattice Boltzmann Simulations of Bubble Dynamics in Microchannels*, in *Proceedings of the 2004 International Conference on MEMS, NANO and Smart Systems, ICMENS '04*, IEEE Computer Society, Washington, DC, USA, pp. 78–83 (2004).
- [73] T. Inamuro, T. Ogata, F. Ogino, *Numerical simulation of bubble flows by the lattice Boltzmann method*, Future Generation Computer Systems, **Vol. 20 (6)** pp. 959 – 964 (2004).
- [74] K. Fei, W. Chen, C. Hong, *Microfluidic analysis of CO₂ bubble dynamics using thermal lattice-Boltzmann method*, Microfluidics and Nanofluidics, **Vol. 5** pp. 119–129 (2008).
- [75] A. Gupta, R. Kumar, *Lattice Boltzmann simulation to study multiple bubble dynamics*, International Journal of Heat and Mass Transfer, **Vol. 51 (21-22)** pp. 5192–5203 (2008).
- [76] M. Cheng, J. Hua, J. Lou, *Simulation of bubble–bubble interaction using a lattice Boltzmann method*, Computers & Fluids, **Vol. 39 (2)** pp. 260–270 (2010).
- [77] J. Bao, L. Schaefer, *Lattice Boltzmann equation model for multi-component multi-phase flow with high density ratios*, Applied Mathematical Modelling, **(0)** (2012).
- [78] N. O. Young, J. S. Goldstein, M. J. Block, *The motion of bubbles in a vertical temperature gradient*, Journal of Fluid Mechanics, **Vol. 6 (03)** pp. 350–356 (1959).
- [79] R. Subramanian, R. Balasubramaniam, *The Motion of Bubbles and Drops in Reduced Gravity*, Cambridge University Press (2001).